LIGHTNING RETURN STROKE CURRENT FROM A NEW DISTRIBUTED CIRCUIT MODEL AND ELECTROMAGNETIC FIELDS GENERATED BY TORTUOUS LIGHTNING CHANNELS

CHIA KOK LIAN DARWIN

B. Eng. (1st class Hons.), NUS

A THESIS SUBMITTED FOR

THE DEGREE OF DOCTOR OF PHILOSOPHY

DEPARTMENT OF ELECTRICAL & COMPUTER ENGINEERING

NATIONAL UNIVERSITY OF SINGAPORE

2007

ACKNOWLEDGEMENTS

I am deeply indebted to Professor Liew Ah Choy, my supervisor, who has guided me with his patience and knowledge. His understanding, encouragement and personal guidance have been inspirational towards the completion of this thesis.

I would like to express my heartfelt gratitude to Professor Walid Tabbara, my co-supervisor, for his care and help. Great appreciation goes to his teachings and constructive criticism, which have been of great value.

My sincere thanks to all the colleagues at the Power Systems Laboratory at NUS and SONDRA at Supélec for their kind friendship and support.

I would also like to express my appreciation to the Singapore Millennium Foundation for the scholarship funding received.

I cannot end without thanking my family and friends for their love and encouragement throughout the extended period of my scholarship.

TABLE OF CONTENTS

SUMMARY

In contribution to the field of lightning research, two lightning return stroke models are developed. The distributed circuit model contrived to produce the lightning return stroke current at ground and the mathematical formulation for the electromagnetic fields generated by tortuous lightning channels are presented.

The distributed circuit model is made up of resistive, capacitive and inductive elements which represent the lightning channel. The inclusion of inductances addresses the limitation of the Pan-Liew model. While simulating the discharge mechanism, the lightning return stroke current at ground was produced to match the 5^{th}-percentile, median and 95^{th}-percentile recorded values of the peak current, charge lowered and front duration reported by Berger *et al.* At the same time, reference to the theoretical waveshape proposed by the Diendorfer-Uman model was kept.

A key function of the distributed circuit model is its applicability in the evaluation of resistive lightning protection terminals in mitigating the lightning return stroke current. Such protection systems can be easily represented by resistive circuit elements and a study was conducted on the Semiconductor Lightning Extender (SLE). From the waveforms of the voltage and current through the SLE, the peak of the return stroke current was shown to be significantly reduced. This demonstrates the efficacy of resistive lightning protection terminals and highlights a major function of the model in such studies, while enforcing the validity of the distributed circuit model.

In the formulation for the electromagnetic fields due to tortuous lightning channels, a flaw identified in Lupò *et al.*'s model was improved upon with a more appropriate current description. The formulation allows for the determination of lightning radiated electromagnetic fields at any distance and height. The resulting waveforms from a randomly generated lightning stroke path demonstrated the sharp initial peak and zero-crossing for fields at far distance, which are key characteristics observed by Lin *et al.* from measured waveforms. Furthermore, while the electromagnetic fields calculated from models adopting the straight vertical lightning channel approximation fail to exhibit the fine structure representing more significant high frequency components in actual measurements, the tortuous channel model clearly displays this attribute. It was also noted that for a lightning channel that does not deviate much from a straight path, which was less than 100 m in both the x- and y-directions for the randomly generated lightning channel, the straight channel approximation adopted by most lightning models is adequate. Potential applications of this model include the reconstruction of the lightning stroke path from remote electromagnetic field measurements and also the study of electromagnetic coupling to systems.

LIST OF PUBLICATIONS

1. K. L. Chia and A. C. Liew, "Modeling of Lightning Return Stroke Current with Inclusion of Distributed Channel Resistance and Inductance," *IEEE Trans. Power Del.*, vol. 19, no. 3, pp. 1342–1347, Jul. 2004.
2. D. K. L. Chia and A. C. Liew, "Analysis of Effect of Resistive Lightning Protection Terminal on Lightning Return Stroke Current," *IEEE Trans. Power Del.*, vol. 20, no. 3, pp. 2307–2314, Jul. 2005.
3. D. K. L. Chia, A. C. Liew and W. Tabbara, "An Improved Model for the Electromagnetic Fields Generated by Tortuous Lightning Channel," *IEEE Trans. Electromagn. Compat.* (under review).

LIST OF TABLES

LIST OF FIGURES

LIST OF SYMBOLS

c	Speed of light
i_{CH}	Return stroke current at base of lightning channel due to breakdown channel discharge
i_{CO}	Return stroke current at base of lightning channel due to corona sheath discharge
i_{CHn}	Current along section n of breakdown channel
i_{COn}	Current along section n of corona sheath
m	Number of sections in distributed circuit model
n_{rods}	Number of semiconductor rods in parallel
$u(t)$	Heaviside step function
v	Return stroke speed
z'	Height along the lightning channel
C_{CHn}	Capacitance value of section n of breakdown channel
C_{COn}	Capacitance value of section n of corona sheath
L_{CHn}	Inductance value of section n of breakdown channel
L_{COn}	Inductance value of section n of corona sheath
R_{CHn}	Resistance value of section n of breakdown channel
R_{COn}	Resistance value of section n of corona sheath
R_r	Distance from the lightning channel segment to the observation point
$R_{CH,weak}$	Breakdown channel weakening resistance
$R_{CO,weak}$	Corona sheath weakening resistance
S_{CHn}	Switch of section n of breakdown channel

S_{COn}	Switch of section *n* of corona sheath
U_{CHn}	Initial voltage across breakdown channel capacitor *n*
U_{COn}	Initial voltage across corona sheath capacitor *n*
$V_{C_{CHn}}$	Voltage across section *n* of breakdown channel capacitance
$V_{C_{COn}}$	Voltage across section *n* of corona sheath capacitance
V_n	Voltage of section *n*
V_{SLE}	Voltage at tip of Semiconductor Lightning Eliminator
$\delta(t)$	Dirac delta function
ε_0	Permittivity of free space
μ_0	Permeability of free space

BG	Bruce-Golde
DU	Diendorfer-Uman
MDU	Modified Diendorfer-Uman
MTL	Modified transmission line
MULS	Master-Uman-Lin-Standler
PL	Pan-Liew
R-L-C	Resistive-inductive-capacitive
SLE	Semiconductor Lightning Extender
TL	Transmission line
TCS	Travelling current source

CHAPTER 1

INTRODUCTION

1.1 BACKGROUND AND OBJECTIVE

1.1.1 Overview on Lightning

Lightning produces one of nature's most powerful forces, causing incalculable damage and quite frequently, death. An understanding of the phenomenon and its effects is therefore of pivotal importance.

The first scientific study of lightning was carried out by Benjamin Franklin in the second half of the eighteen century. When Franklin flew his kite into a thunderstorm in 1752, he was exceptionally lucky not to be killed. He managed to draw charge from a storm cloud down his kite string and as he reached for the key tied to the bottom of the string, he received an electric shock when sparks jumped onto his knuckles. Undoubtedly thrilled with his discovery, he remained unaware that he should be doubly delighted at having lived through the experiment. A Swedish physicist attempting to repeat Franklin's experiment a year later with a lightning rod instead of a kite was killed instantly. Franklin had proven that lightning and static electricity are similar, except in scale. He later showed the world how to protect property from

lightning with the lightning rod. Today, this invention remains virtually unchanged, after more than two hundred years.

Ensuing studies on lightning theorised the discharge mechanism as we know it today. The stepped leader is preceded by a preliminary breakdown within the cloud. With the breakdown of air, the stepped leader is launched. In its path towards ground, it deposits charges on the breakdown channel. The radial electric field created by the deposited charges results in the formation of a corona envelope. As the leader tip approaches ground, the electric field beneath it increases and consequently, initiates an upward streamer. The attachment process follows where the leader and streamer meet. The first return stroke is subsequently initiated and propagates upwards along the ionised leader path. The return stroke discharges the channel, as well as the corona envelope, resulting in what is known as the return stroke current. The process may be terminated when the return stroke reaches the cloud base and the lightning channel is discharged. The other variation is where subsequent dart leaders are released and corresponding return strokes are initiated. A typical cloud-to-ground flash usually comprises of three or four leader-return stroke pairs [1, 2, 7].

Lightning models have been proposed with the aim obtaining a better understanding of the phenomenon and its effects. By reproducing certain aspects of the physical process, prediction of characteristics such as the return stroke current and electromagnetic fields allow for the analysis of the consequence resulting from this act of nature.

1.1.2 Objective and Contribution of Work Undertaken

The Pan-Liew (PL) model presents a simplified circuit model simulating the lightning discharge channel of the return stroke [3]. The equivalent circuit of the PL model comprises of resistive and capacitive (*R*-*C*) elements. Its omission of inductive elements is the impetus for an improved model. The proposed model seeks to include distributed resistance and inductance in the lightning channel.

The distributed model comprises of a network of *R*-*L*-*C* elements to represent the lightning channel. The equivalent circuit of the proposed model was drawn up and its equations were derived and subsequently solved to generate the current waveforms at the base of the lightning channel with the aim of fitting the proposed model to measured lightning values and established lightning waveforms.

An innovative lightning protection system, the Semiconductor Lightning Extender (SLE), is presently used widely in China. It comprises of highly resistive rods arranged in a 3-dimensional fan shape structure, and have shown to be capable of limiting lightning current [4, 5]. A study was conducted by applying the proposed model on the SLE to demonstrate the applicability of the proposed model in predicting the voltage and current levels at lightning protection terminal systems to assess their behaviour and performance.

It is a known fact that a lightning channel is tortuous in nature but models adopting such geometry are limited. In the model by Lupò *et al*. [6], the tortuous channel was broken down into a series of arbitrarily oriented straight segments and these were treated individually. The overall effect of the tortuous channel was then found by

summing up the individual components. But an error was discovered in the formulation. Revised current and charge distribution profiles are presented together with the ensuing mathematical formulation. The resultant electromagnetic fields at near and far distances are computed to illustrate the utility of the model.

1.2 ORGANISATION OF THESIS

There are a total of seven chapters. Following this introduction, Chapter 2 provides a more detailed description of the lightning discharge mechanism. It also lists the various types of lightning flashes.

Chapter 3 reviews some of the lightning return stroke models developed. These models are usually classified into four general categories. The characteristics of each category are also presented.

The distributed circuit model is described in Chapter 4. The basic assumptions made and the conception of the model will be described in detail. The derivation of the equations governed by the circuit model proposed is presented. The results obtained from the model as well as an evaluation of the proposed model follows.

Chapter 5 presents a description of the SLE and its characteristics, together with the nature of its modelling. The findings of the study are then illustrated and discussed.

The development of the model for calculation of electromagnetic fields due to tortuous lightning channels is featured comprehensively in Chapter 6. The resulting waveforms are then shown together with an assessment of the model.

The final chapter concludes the report as well as mentions the scope for future work.

CHAPTER 2

THE LIGHTNING DISCHARGE

Lightning is a transient, high-current electric discharge. It has also been proven that lightning is not an alternating current because the electric charge transferred in a lightning flash mostly moves in only one direction. It is also known that the propagation path is never straight, though it moves in a general direction. On top of that, theoretical advancements over the years have allowed us to establish certain basic understanding of the lightning discharge.

2.1 TYPES OF LIGHTNING DISCHARGES

Lightning discharges are generally classified under cloud-to-ground flashes or cloud flashes depending on whether ground is involved. The majority of lightning discharges fall under the latter group which include intracloud, intercloud and cloud-to-air discharges [7]. But most studies have revolved around cloud-to-ground lightning (sometimes called streaked or forked lightning) because of its practical interest. It is this form of lightning that usually causes injury or death, disturbances in power and communication systems, forest fires and other damages.

Berger has categorised lightning between cloud and ground into four different types in terms of direction of motion, upward or downward, and the polarity of the charge, positive or negative, of the leader that initiates the discharge [8]. The four types, illustrated in Figure 2.1, are as follows:

1. *Negative downward lightning*: A downward-moving negatively charged leader lowers negative charges from the cloud to earth. This is the most common type of cloud-to-ground flash accounting for over 90% of worldwide cloud-to-ground flashes.

2. *Positive upward lightning*: An upward-moving positively charged leader carries positive charges from the earth to cloud.

3. *Positive downward lightning*: A downward-moving positively charged leader lowers positive charges from the cloud to earth. Less than 10% of worldwide cloud-to-ground lightning is of this type.

4. *Negative upward leader*: An upward-moving negatively charged leader carries negative charges from the earth to cloud.

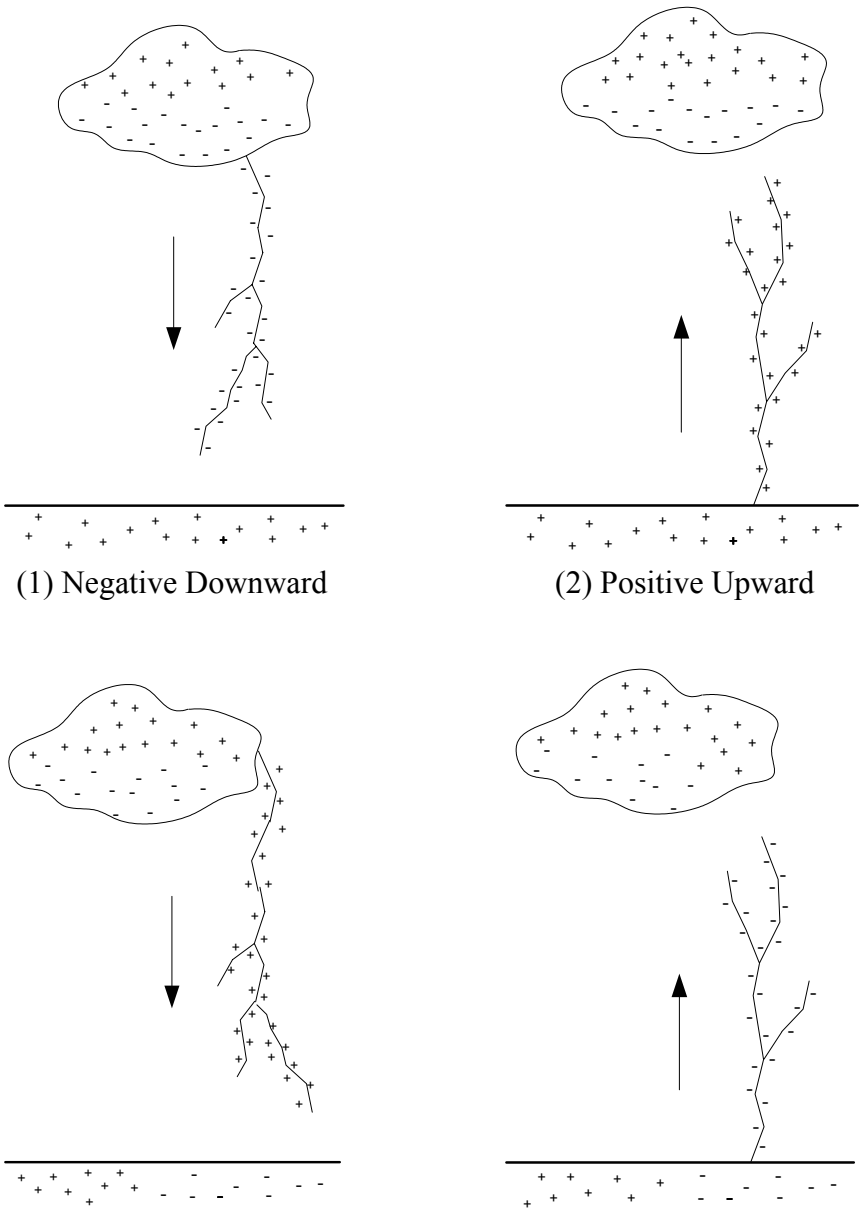

(1) Negative Downward (2) Positive Upward

(3) Positive Downward (4) Negative Upward

Figure 2.1 Categorisation of lightning

Categories 2 and 4 are relatively rare and generally occur from mountain tops and tall man-made buildings. And because the leaders move upward from the earth, they are sometimes called earth-to-cloud discharges.

Since the most frequent type of cloud-to-ground lightning flash is initiated by a negative downward leader, it has been the most studied type and it will be used to

describe the lightning discharge mechanism. Further discussions in this report will also be based on the negative cloud-to-ground discharge.

2.2 LIGHTNING DISCHARGE MECHANISM

2.2.1 Preliminary Breakdown

Far above the earth, there exists a region in the atmosphere, known as the ionosphere, which contains more ions, or charged particles, than uncharged particles or neutral molecules. With the earth having a surplus of electrons, a potential difference is set up between the ionosphere and the earth. This potential difference, which is about 300,000 V, is the driving force behind a small current, about 35 $\mu A/km^2$, flowing in the air [9]. The reason we do not feel this current is because its magnitude is too small. Hence, on a fair-weather day, negative ions migrate upwards and positive ions move downwards, seemingly neutralising the potential difference.

The ion movement is brought about by water particles which bring positive charges down as rain or snow and electrons up as water moisture. Some of these water particles are deposited in a region between the ionosphere and the earth. This region, known as the troposphere, is where cumulonimbus clouds, also referred to as thunderclouds or thunderstorms, are found. While the distribution and motion of electric charges within a thunderstorm is complex and constantly changing, it is generally accepted that a thundercloud has a net positive charge near the top, a net negative charge below it, and an additional positive charge at the bottom of the cloud [10]. The main charges are the top two charges and the lower positive charge may not always be present.

The negative charges in a thundercloud repel the earth's negative charges directly below it, reversing the potential difference. The earth effectively becomes positively charged. The potential below a thundercloud reaches a magnitude of about 10 to 100 MV [9]. This large potential difference sets up an electric field between the thundercloud and earth. As the charges are not stationary, the electric field varies for a duration from a few milliseconds to a few hundred milliseconds prior to the beginning of the stepped leader [11]. And when the strength of the electric field due to a charge centre in the thundercloud becomes greater than the electric breakdown strength of air, the region of air directly below the thundercloud is ionised and the initial leader, carrying negative charges, is released from the thundercloud and begins its propagation towards earth.

2.2.2 Stepped Leader

A significant fraction of what is known about stepped leaders was determined in the 1930s by Schonland and his associates in South Africa using streak-photograph measurements [1, 2, 7]. It revealed that the leader process does not move downward in a smooth continuous motion. Instead, it actually "steps", pausing at regular intervals before continuing further.

In-between steps, air below the stepped leader is broken down to allow further propagation. It is likely that the stepped leader will branch out to "look" for the easiest path downwards. Hence, it does not necessarily move down directly because of minor field fluctuations in the air. It has to be noted that some stepped leaders are discontinued in mid-air because it fails to breakdown the air below it.

Stepped leaders move an average of tens of meters in a time span averaging 1 μs, and the average time interval between steps is about 50 μs. Schonland reported that the minimum three-dimensional speed is estimated to be 1×10^5 m/s and the most often measured two-dimensional speed is between 1 and 2×10^5 m/s [12]. The two-dimensional speed is the speed seen from the two-dimensional photographs taken whereas the three-dimensional speed is the actual speed in space which was estimated. The stepped leader current near ground was recorded by Thomson *et al*. in Florida to have a mean of 1.3 kA, ranging from 100 A to 5 kA [13]. And the total charge on stepped leader ranges from a few coulombs to 10 to 20 C with a resulting average charge lowered per unit length of the order of 10^{-3} C/m.

As the stepped leader propagates downwards, negative charges are deposited on the channel formed. Due to the high potential of the deposited charges, a corona sheath is consequently formed. This explains the luminosity seen in the streak-photographs. And it is the leader tip which is the most luminous part of the stepped leader. The structure of the propagation path is a core surrounded by a corona sheath.

2.2.3 Attachment Process

While it is possible that the stepped leader reaches earth or any object at the end of its path purely through its own "stepping" motion, it is highly improbable. The leader usually propagates towards a sharp or pointed object, such as the tip of a tower, or even a leaf or a blade of grass. At the end of its path, it is met by another electrical phenomenon.

Most people are unaware of an electrical process going on at their very feet. Franklin was one of the first to notice that a charged body with a sharp point loses its charge faster than a flat body. When ions collide in a concentrated area, such as the charged region at the tip of a point, additional ions are produced and a transfer of electrons takes place between the ions and the point. This is known as point discharge. Since the earth is a conductor, natural points, namely tips of blades of grass and leaves, conduct charges away from the earth and discharge them away into the air. This brings about a region of air of lower electric breakdown strength.

When the stepped leader approaches any pointed object, the electric field produced by the charge on the leader greatly intensifies the effect of point discharges. Under this influence, one or more streamers start upwards. And when the leader is within striking distance, it makes the final step to engage "contact" with the streamer and a continuous channel from the cloud to earth is thus formed.

Many photographs of lightning to ground or to structures show a pronounced kink or change in direction of the channel near the ground or structure. Below the kink, the channel is generally straight. Striking distances are generally between about 10 and a few hundred metres [1, 7].

2.2.4 Return Stroke

The continuous channel formed after the attachment process has relatively low resistance. And since the potential difference between the base of the thundercloud and earth is in excess of 10^7 V, current flows in the channel, discharging it [9].

The discharging process begins at the base of the channel and progresses upward towards the top of the channel. Since both the core, known as the breakdown channel, and the envelope around it, known as the corona sheath, have charges deposited along them, both are discharged by the return stroke.

During the discharging process, the negative charges are lowered back to earth. It can also be viewed as the movement of positive charges upward to neutralise both the breakdown channel and the corona sheath. The neutralisation front, which moves in a direction opposite to the stepped leader, is known as the return stroke.

The return stroke is the most researched and, consequently, the best understood of all the processes that make up a flash to earth. The current measured at ground level reaches its peak value, median of 30 kA, in a median time interval of 5.5 μs and the amount of charge lowered is about 4.5 C (as shown in Table 2.1) [14]. The return stroke speed, v, is also an important parameter of the cloud-to-ground flash. The average speed is $1.3\pm0.3\times10^8$ m/s for long-channels exceeding 500 m in length, and $1.9\pm0.7\times10^8$ m/s for channel lengths less than 500 m [15]. The measured values also show that the return-stroke speed decreases with height.

About 75% of the energy in a lightning flash is dissipated as heat into the air. This raises the temperature of the lightning channel to about 30,000 K [1, 7]. The result is a sharp increase of temperature and pressure in the air surrounding the lightning channel. This causes the air to expand radially outwards, and consequently sound waves are formed generating the loud noise we commonly know as thunder.

Some lightning flashes are terminated when the return stroke reaches the base of the thundercloud. Such flashes are known as single stroke flashes. Figure 2.2 illustrates the mechanism of a single stroke lightning flash. But most lightning flashes are made up of more than one stroke. The mean number of strokes per flash was found to be 4.1 by Schonland in South Africa [12] and 4.0 by Thomson *et al.* in Florida [16].

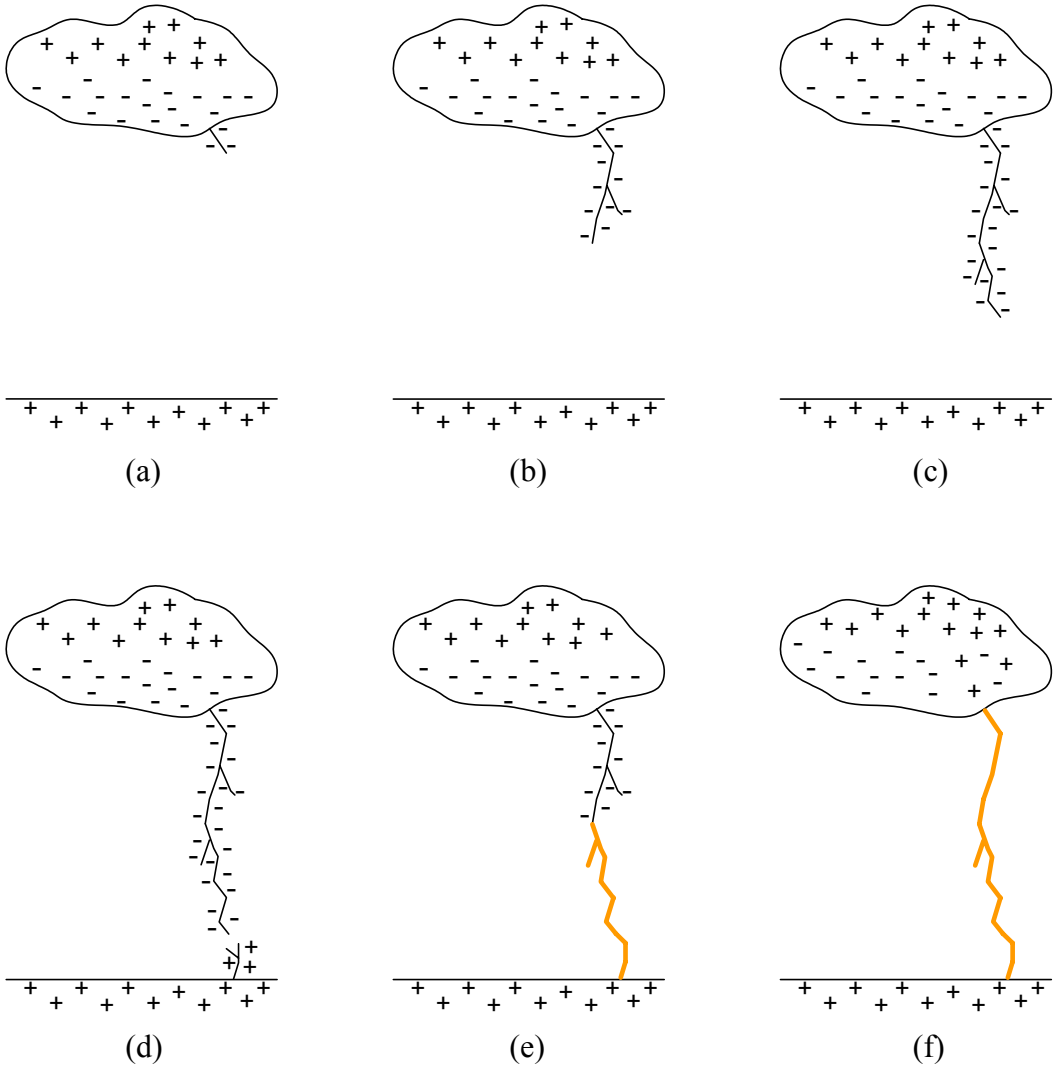

Figure 2.2 Single stroke lightning flash

(a): preliminary breakdown. (b) & (c): stepped leader.

(d): attachment process. (e) & (f): return stroke.

2.2.5 Subsequent and Multiple Strokes

If additional charges are available from another charge centre in the thundercloud, at the top of the lightning channel, a dart leader may propagate down at an average speed of about 1×10^7 m/s without additional branching [1]. Since the channel is still "hot", the stepping process is bypassed and the dart leader propagates downward in a continuous motion. As the dart leader reaches ground, it initiates another return stroke. After the second return stroke reaches the top of the channel, another dart leader might be released. The same process could be repeated leading to multiple strokes.

The dart leader, on average, lowers a charge of the order of 1 C by virtue of a current of about 1 kA [17]. Subsequent return-stroke currents have faster zero-to-peak rise-times than first stroke currents but usually carry lower charge.

Continuing currents may flow in the channel following the return stroke, representing a direct transfer of charge from cloud to ground. Its magnitude is typically of the order of tens to hundreds of amperes and typically lasts for tens to hundreds of milliseconds.

The time between successive strokes in a flash is usually several tens of milliseconds, but can be tenths of a second if a continuing current flows in the channel after a return stroke.

2.3 LIGHTNING CURRENT

In many respects the lightning current is the most important single parameter of the lightning discharge. With knowledge of the waveform and amplitude of the current,

the electrical problems of protection against lightning can be better understood and addressed.

The most complete description of lightning return stroke current at the base of the stroke channel is due to Berger and his co-workers in Switzerland. The currents were derived from measurements induced in resistive shunts located at the tops of two towers each 55 m above the summit of Mt. San Salvatore in Lugano. The resulting cumulative frequency distributions are reproduced in Table 2.1 [14].

Table 2.1 Lightning Current Parameters

Number of events	Parameters	Unit	Percentage of cases exceeding tabulated values		
			95%	50%	5%
	Peak current (minimum 2 kA)				
101	Negative first strokes	kA	14	30	80
135	Negative subsequent strokes	kA	4.6	12	30
20	Positive first strokes	kA	4.6	35	250
	Charge				
93	Negative first strokes	C	1.1	5.2	24
122	Negative subsequent strokes	C	0.2	1.4	11
94	Negative flashes	C	1.3	7.5	40
26	Positive flashes	C	20	80	350
	Impulse charge				
90	Negative first strokes	C	1.1	4.5	20
11	Negative subsequent strokes	C	0.22	0.95	4.0
25	Positive first strokes	C	2.0	16	150

	Front duration (2 kA to peak)				
89	Negative first strokes	μs	1.8	5.5	18
118	Negative subsequent strokes	μs	0.22	1.1	4.5
19	Positive first strokes	μs	3.5	22	200
	Maximum *di/dt*				
92	Negative first strokes	kA/μs	5.5	12	32
122	Negative subsequent strokes	kA/μs	12	40	120
21	Positive first strokes	kA/μs	0.20	2.4	32
	Stroke duration (2 kA to half-value)				
90	Negative first strokes	μs	30	75	200
115	Negative subsequent strokes	μs	6.5	32	140
16	Positive first strokes	μs	25	230	2000
	Integral ($i^2\,dt$)				
91	Negative first strokes	$A^2\,s$	6.0×10^3	5.5×10^4	5.5×10^5
88	Negative subsequent strokes	$A^2\,s$	5.5×10^2	6.0×10^3	5.2×10^4
26	Positive first strokes	$A^2\,s$	2.5×10^4	6.5×10^4	1.5×10^7
	Time interval				
133	Between negative strokes	ms	7	33	150
	Flash duration				
94	Negative (including single-stroke flashes)	ms	0.15	13	1100
39	Negative (excluding single-stroke flashes)	ms	31	180	900
24	Positive (only single flashes)	ms	14	85	500

The peak current in negative first strokes range from a few kilo-amperes to beyond 80 kA while that of negative subsequent strokes are lower. The median peak current of 30 kA for negative first strokes and 35 kA positive first strokes are comparable, but the upper 5 % recorded peak currents of the latter reached up to three times that of the former. The stroke duration is generally longer for positive first strokes compared to

negative first strokes with negative subsequent strokes lasting for the shortest period of time. This provides some explanation to why the charge lowered is greatest for positive strokes and smallest for negative subsequent strokes. The rise time is also longest for positive first strokes and shortest for negative subsequent strokes.

The time derivative of current is also an important parameter. The voltage induced by lightning current is directly proportional to its rate of change and overvoltages induced often cause damage to equipment. Positive first strokes exhibit the lowest maximum *di/dt* while negative subsequent strokes display a large value. This can also be attributed to its shortest rise time.

The charge lowered can be found by integrating the current waveform over time. It can be seen that the majority of the charge lowered in a negative flash is due to the first stroke, which lowers 5.2 C. But while the negative flash typically lowers 7.5 C of charge, the less common positive flash carries a median value of 80 C.

Field measurements of return stroke current parameters have shown that the negative first stroke carries a larger current and charge compared to subsequent strokes. Even though the time derivative of the latter is larger, most models developed are mainly concerned with the first return stroke because of the damaging effects caused by the large magnitude of the discharge current and its consequent electromagnetic fields.

2.4 LIGHTNING ELECTROMAGNETIC FIELDS

Radiated electromagnetic fields are another cause of damage due to lightning flashes. Coupling to systems can bring about current and voltage surges which subsequently lead to impairment of normal operations. Hence, measurements of lightning

electromagnetic fields are taken to allow better understanding of the phenomenon. Furthermore, such measurements also allow for the inference of the lightning discharge current.

Lin *et al*. presented results from electric and magnetic field measurements recorded at distances between 1 and 200 km [18]. Drawings of these waveforms, based on the measurements, illustrate typical vertical electric and azimuthal magnetic fields for first and subsequent strokes and are reproduced in Figure 2.3.

From these waveforms, the following key features have been identified:

1) a distinct initial peak in both electric and magnetic fields measured beyond about 10 kilometres;
2) a slow ramp following the initial peak for electric fields measured within a few tens of kilometres;
3) a hump following the initial peak in magnetic fields measured within several tens of kilometres;
4) zero crossing within tens of microseconds of the initial peak in both electric and magnetic fields beyond about 50 km;

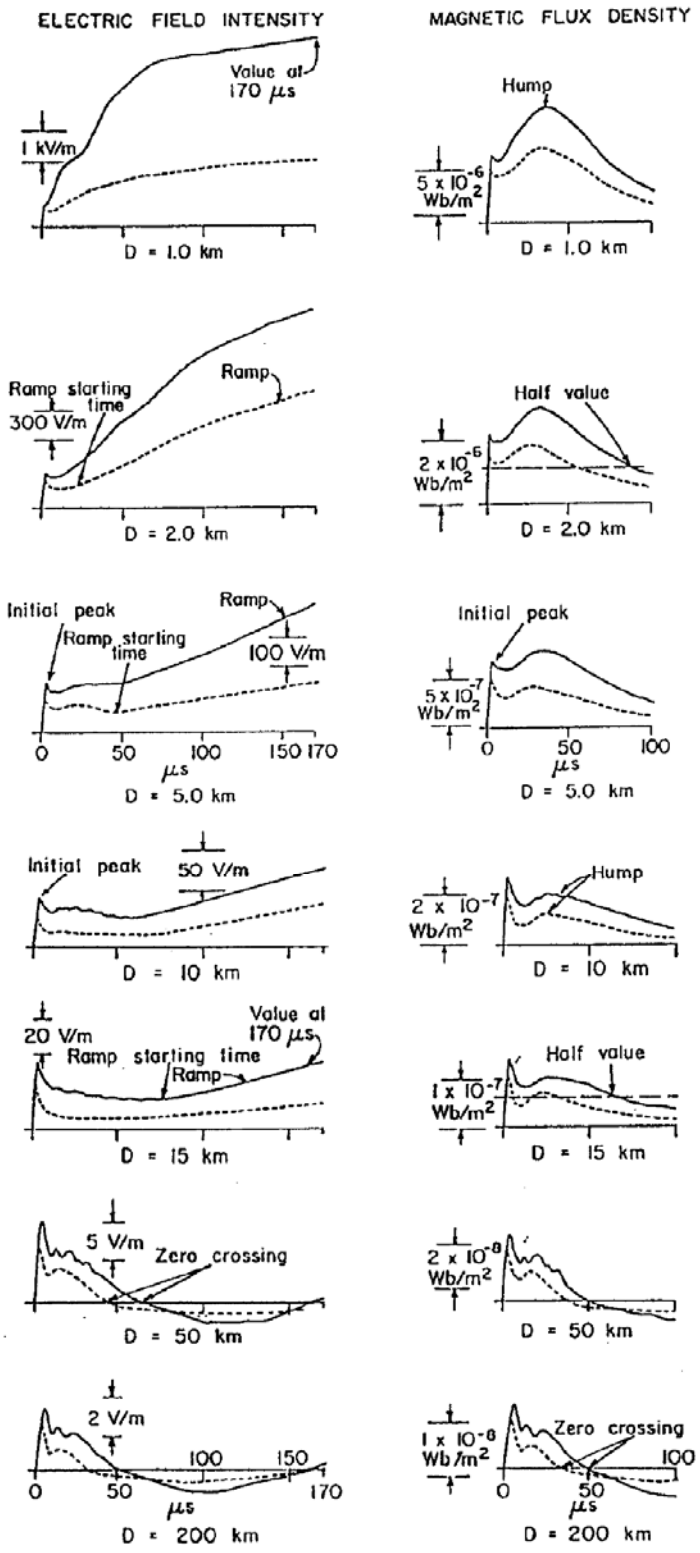

Figure 2.3 Typical vertical electric field intensity (left column) and azimuthal magnetic flux density (right column) waveforms for the first (solid line) and subsequent (dashed line) return strokes at distances of 1, 2, 5, 10, 15, 50 and 200 km. The time scales are in μs.

CHAPTER 3

LIGHTNING RETURN STROKE MODELS

Lightning models can be used for the description of the characteristics of the lightning return stroke. Most models relate the remote electric and magnetic fields to the channel current [19, 20] and some allow us to study the effects of lightning on lightning conductors and thus, the behaviour of lightning protection systems.

3.1 MODELLING

Rakov and Uman [7] defined four classes of lightning return-stroke models which differ primarily by the type of governing equations:

(1) Gas dynamic or "physical" models are primarily concerned with the radial evolution of a short segment of the lightning channel and its associated shock wave. The three dynamic gas equations representing the conservation of mass, momentum and energy are typically involved to find the temperature, pressure, and mass density as a function of the radial coordinate and time. Such a model

could even allow the determination of the properties of the shock waves generated by expansion of the hot channel. An example of work on this type of model was performed by Paxton *et al.* whose results include the temperature, mass density, pressure and electrical conductivity variations versus radial coordinate at different instants of time [21].

(2) Electromagnetic models are usually based on a lossy, thin-wire antenna approximation to the lightning channel. Numerical analysis of Maxwell's equations is employed to compute the current distribution along the channel from which remote electromagnetic fields can be determined. Podgorski and Landt [22], Moini et al. [23], and Baba and Ishii [24] proposed such models which involve the numerical solution of Maxwell's equations using the method of moments to find the complete solution for the channel current.

(3) Distributed-circuit models can be regarded as an approximation to electromagnetic models and represent the lightning discharge as a transient process on a vertical transmission line characterised by resistive (R), inductive (L) and capacitive (C) elements which are functions of time and space. Also called *RLC* transmission line models, the channel current as a function of time and height is determined and used to calculate remote electromagnetic fields. Little [25] set up such a model to calculate current pulses at various heights, including ground, with a non-uniform transmission line represented by a lumped-parameter ladder network shown in Figure 3.1. The inductance and capacitance values were deduced from the electrostatic field distribution around a simplified model of a cloud charge and a vertical unbranched leader. The resistance of the

channel was assumed to be constant with height, and all the network parameters are assumed independent of time. The switch is closed to simulate connection of the channel to ground and the resulting current pulse parameters deduced at ground level are in rough agreement with observations.

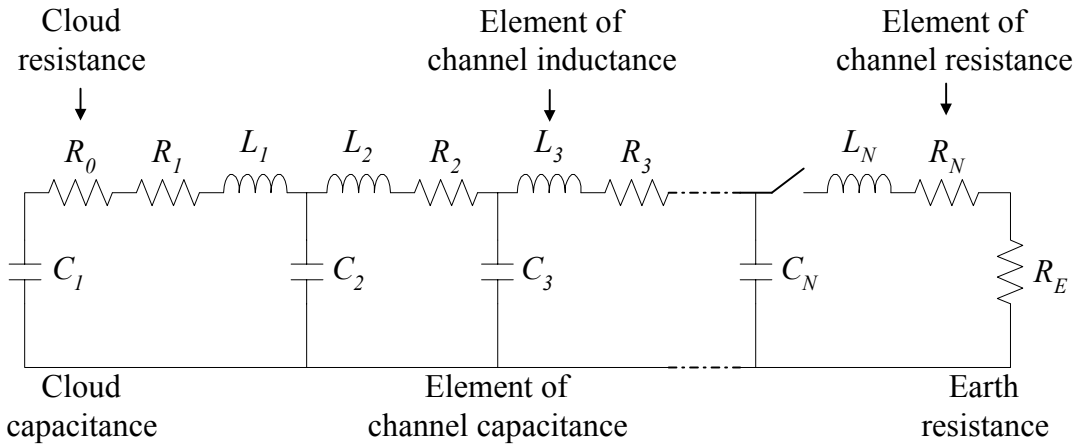

Figure 3.1 Lumped parameter transmission line representation of lightning return stroke

(4) In engineering models, the spatial and temporal distribution of the channel current or channel line charge density is specified based on observed lightning return stroke characteristic such as the channel base current and the return stroke wavefront speed. The physics of the lightning return stroke is deliberately downplayed while placing emphasis on achieving coherence between model-predicted electromagnetic fields and those observed. Notable examples include the Bruce-Golde (BG) model [26], the transmission line (TL) model [27], the Master-Uman-Lin-Standler (MULS) model [28], the travelling current source (TCS) model [29] and the Diendorfer-Uman (DU) model [30] which will be discussed later.

While models can fall under more than one of these classes, the most common and least sophisticated type fall under engineering models. Uman *et al.* [31] and Master and Uman [32] have demonstrated how remote electromagnetic fields can be computed from Maxwell's equations given the current in a vertical channel above a perfectly conducting ground. For the cylindrical coordinate system given in Figure 3.2, the electric and magnetic fields at a location (*r, ϕ, z*) from a short vertical section of the channel *dz′* at height *z′* carrying a time-varying current *i(z′, t)* are:

$$\begin{aligned} d\mathbf{E}(r,\phi,z,t) = \frac{dz'}{4\pi\varepsilon_0}\Bigg\{\Bigg[\frac{3r(z-z')}{R^5}\int_0^t i(z',\tau-R/c)d\tau + \\ + \frac{3r(z-z')}{cR^4}i(z',t-R/c) + \frac{r(z-z')}{c^2R^3}\frac{\partial i(z',t-R/c)}{\partial t}\Bigg]\mathbf{a}_r \\ + \Bigg[\frac{2(z-z')^2-r^2}{R^5}\int_0^t i(z',\tau-R/c)d\tau \\ + \frac{2(z-z')^2-r^2}{c^2R^4}i(z',t-R/c) \\ - \frac{r^2}{c^2R^3}\frac{\partial i(z',t-R/c)}{\partial t}\Bigg]\mathbf{a}_z\Bigg\} \end{aligned} \tag{3.1}$$

$$d\mathbf{B}(r,\phi,z,t) = \frac{\mu_0 dz'}{4\pi}\left[\frac{r}{R^3}i(z',t-R/c) + \frac{r}{cR^2}\frac{\partial i(z',t-R/c)}{\partial t}\right]\mathbf{a}_\phi \tag{3.2}$$

where c is the speed of light, and ε_0 and μ_0 are the free-space permittivity and permeability respectively.

In equation (3.1), the terms containing the current integral are called electrostatic fields, the terms containing the current derivative are called the radiation fields and the terms containing current are called intermediate or induction fields. In equation (3.2), the first term is called induction or magnetostatic term and the second term is the radiation field. The effects of the perfectly conducting ground plane are included by

postulating an image current beneath the plane as shown in Figure 3.2. The electric and magnetic fields of the image are obtained by substituting R_I for R and $-z'$ for z' in equations (3.1) and (3.2). Once the expression for the fields of a short channel section is formulated, the fields for the total channel are found by integrating over the channel.

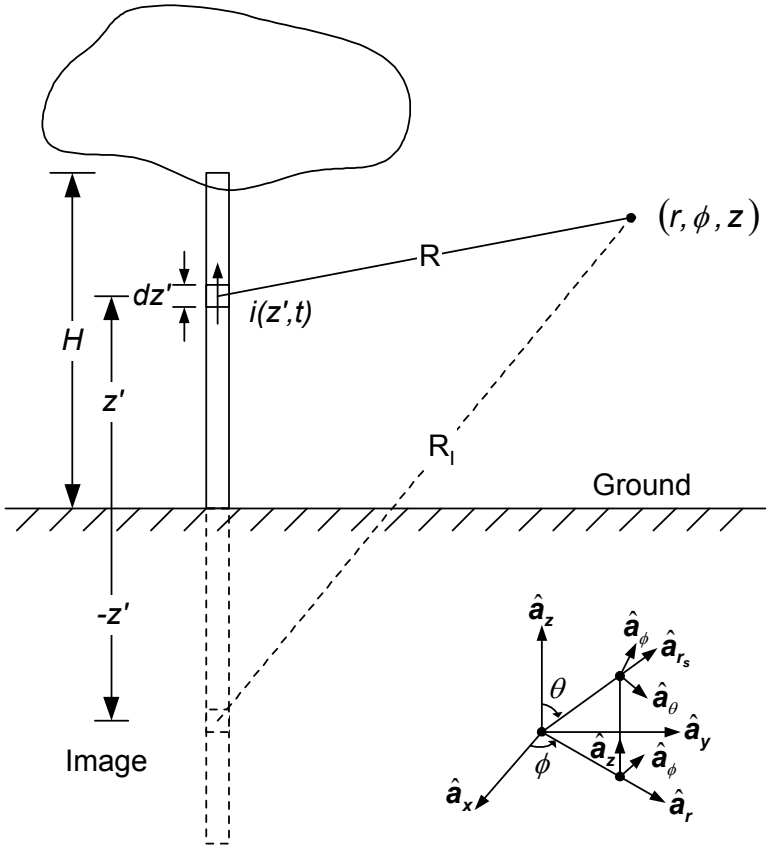

Figure 3.2 Geometrical parameters used in the models

3.2 BRUCE-GOLDE (BG) MODEL

This is perhaps the simplest return stroke current model. The current at any time is assumed to be uniform for heights below the return stroke wave front; above the wave front, the current is zero [26].

$$\begin{aligned} i(z',t) &= i(0,t) \qquad z' \le vt \\ i(z',t) &= 0 \qquad\quad z' > vt \end{aligned} \tag{3.3}$$

where v is the speed of the return stroke.

The current distribution along the BG return stroke channel exhibits a discontinuity at the return stroke wave front. This implies that the charge at each height is removed from the channel instantaneously by the return stroke wave front.

3.3 TRANSMISSION LINE (TL) MODEL

The current specified at the base of the channel is assumed to propagate upward with the speed of the return stroke, as if the channel were a lossless transmission line [27]. The current at a given height is equal to the current at ground at a time z'/v earlier.

$$\begin{aligned} i(z',t) &= i\left(0, t - \frac{z'}{v}\right) \qquad z' \le vt \\ i(z',t) &= 0 \qquad\qquad\qquad\quad z' > vt \end{aligned} \tag{3.4}$$

This model only allows the transfer of charge from the bottom of the leader channel to the top. No charge is removed from the channel by the return stroke since the channel simply acts as an ideal transmission line for the upward propagating current wave. This is one reason why the fields calculated from the model are unrealistic at longer times and closer ranges when compared with measurements.

The modified transmission line (MTL) model was formulated to correct the limitation of the TL model. It takes into account the contribution of the corona charges during the return stroke phase. The waveform of current remains fixed with height while the

amplitudes decrease. In the MTL model proposed by Nucci [33], the current is assumed to decrease exponentially and the return stroke speed is assumed to be constant.

$$\begin{aligned} i(z',t) &= e^{-z'/\lambda} i\left(0, t-\frac{z'}{v}\right) \qquad z' \le vt \\ i(z',t) &= 0 \qquad\qquad\qquad\qquad\qquad\quad z' > vt \end{aligned} \tag{3.5}$$

where λ is the decay constant.

The decay accounts for the effect of the vertical distribution of charge stored in the corona sheath of the leader which is subsequently discharged during the return stroke phase. Removal of charge from the leader channel at height z' starts when the return stroke front passes the height z' and is continued to the end of current flow at ground level.

3.4 MASTER-UMAN-LIN-STANDLER (MULS) MODEL

In the MULS model, the return stroke current is decomposed into three components [28, 34]:

(1) A uniform current, I_u that can be viewed as a continuation of the preceding steady leader current. This component can be drawn from the electric field change near the lightning channel as seen in electric field measurements.

(2) A breakdown pulse current, i_p, that propagates up the channel with a constant speed. This current can be treated using the TL model

$$i_p(z',t) = i_p\left(0, t - \frac{z'}{v}\right) \tag{3.6}$$

or more accurately, using the MTL model

$$i_p(z',t) = e^{-\frac{z'}{\lambda_p}} i_p\left(0, t - \frac{z'}{v}\right) \tag{3.7}$$

where $i_p(0,t)$ is the breakdown pulse current at ground level and λ_p is the height decay constant.

This is the component responsible for the initial peak electric and magnetic fields.

(3) A corona current, i_c, due to the discharge of the charge stored in the corona envelope around the leader channel. This component has been modelled by assuming distributed current sources along the channel whose functional form is that of a double exponential and whose amplitude decreases with height along the channel. Each source is switched on when the peak of the upward propagating breakdown pulse reached its height and the corona charges are assumed to flow to ground at the speed of light, c.

$$i_c(z',t) = e^{-\frac{z'}{\lambda_c}} i_c\left(0, t - \frac{z'}{v} - t_{on}\right) \tag{3.8}$$

where

$$\begin{aligned} i_c(0,t) = \frac{I_0}{p_1}\left\{\exp\left[\frac{-t}{\lambda_c}\left(\frac{1}{v}+\frac{1}{c}\right)\right] - \exp(-\alpha t)\right\} \\ + \frac{I_0}{p_2}\left\{\exp(-\beta t) - \exp\left[\frac{-t}{\lambda_c}\left(\frac{1}{v}+\frac{1}{c}\right)\right]\right\} \end{aligned} \tag{3.9}$$

and

$$p_1 = \alpha\left(\frac{1}{v}+\frac{1}{c}\right)-\frac{1}{\lambda_c} \tag{3.10}$$

$$p_2 = \beta\left(\frac{1}{v}+\frac{1}{c}\right)-\frac{1}{\lambda_c} \tag{3.11}$$

and I_o, α and β are the parameters which determine the assumed double exponential waveform of the single corona source, λ_c is the decay constant which forces the corona sources to decrease with height and t_{on} is the zero-to-peak time of the breakdown pulse current.

Therefore, the overall current at any height can be related to the current at the channel base

$$\begin{aligned} i(z',t) &= I_u + i_p(z',t) + i_c(z',t) \\ &= I_u + e^{-\frac{z'}{\lambda_p}} i_p\left(0, t-\frac{z'}{v}\right) + e^{-\frac{z'}{\lambda_c}} i_c\left(0, t-\frac{z'}{v}-t_{on}\right) \end{aligned} \tag{3.12}$$

3.5 TRAVELLING CURRENT SOURCE (TCS) MODEL

The charge on the channel is assumed to be instantaneously released from the leader channel by the return stroke wave front, propagating upward with a constant speed, with which is associated a travelling current source. The resulting current is assumed to propagate to ground at the speed of light [29]. The current injected by the travelling current source at each height z' reaches the channel base at time z'/c later.

$$\begin{aligned} i(z',t) &= i\left(0, t+\frac{z'}{c}\right) && z' \le vt \\ i(z',t) &= 0 && z' > vt \end{aligned} \tag{3.13}$$

It is interesting to note that for the case where current flows to ground at infinite speed, the TCS model reduces to the BG model, even though both models were conceived independently. But similarly, the TCS model shows a discontinuity in the return stroke wave front.

3.6 DIENDORFER-UMAN (DU) MODEL

The DU model combines the general features of the TCS model with the idea of exponential discharge of the leader in the MTL and MULS models. In the DU model, the return stroke wave front initiates an exponential release of the leader charge deposited on the channel, and the resulting current wave propagates to ground at the speed of light [30]. When the return stroke wave front travelling at a speed of v passes height z', the channel segment dz' is discharged with a discharge time constant τ_D into the channel to ground. For a specified current at ground strike point $i(0, t)$, the current $i(z',t)$ at height z' is given by

$$i(z',t) = i\left(0, t + \frac{z'}{c}\right) - i\left(0, \frac{z'}{v} + \frac{z'}{c}\right) e^{-\left(t - \frac{z'}{v}\right)/\tau_D} \qquad z' \le vt \tag{3.14}$$

The channel current is considered to be the sum of two components, one due to a fast discharge of the channel core (i_{BD}) with a smaller time constant and the other due to a slower discharge of the outer corona sheath of stored charges (i_C) with a longer discharge time constant. Each of the two components at the base of the lightning channel is calculated analytically from the Heidler function [29]:

$$i(0,t) = \frac{I_0}{\mu} \frac{(t/\tau_1)^2}{\left[(t/\tau_1)^2 + 1\right]} e^{-t/\tau_2} \tag{3.15}$$

where the various constants are amplitude I_0, amplitude correction factor μ, current rise time constant τ_1, and current decay time constant τ_2.

The current at the base of the lightning channel using equation (3.15) is reproduced from [30] using constants given in Table 3.1 and is shown in Figure 3.3

Table 3.1 Constants Used to Calculate Return Stroke Current in the DU Model

	i_{BD}	i_C
I_0 (kA)	28	16
μ	0.73	0.53
τ_1 (μs)	0.3	10
τ_2 (μs)	6.0	50

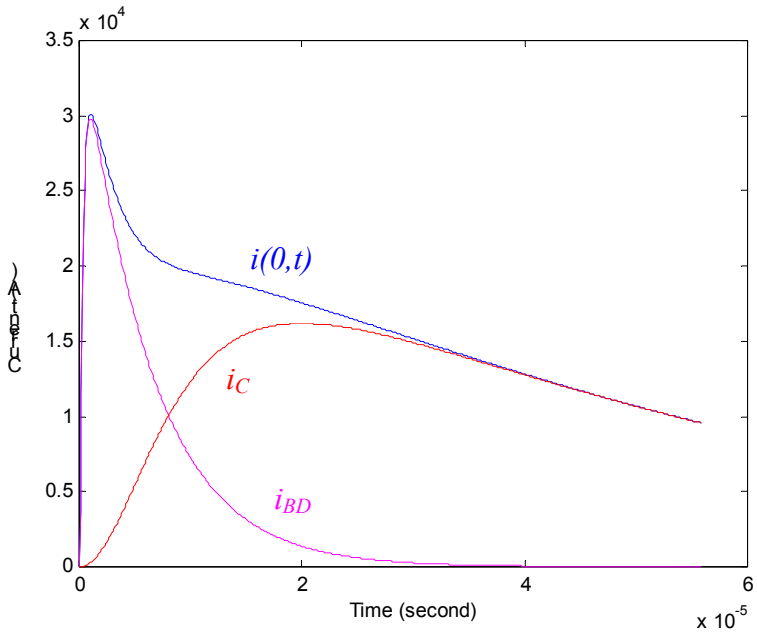

Figure 3.3 Channel-base return stroke current in the DU model

The current waveform is similar to a measured lightning return stroke current. The peak current is 30 kA and the maximum current derivative is 80 kA/μs.

Thottppillil *et al.* generalised the DU model to include a variable upward return stroke speed and a variable downward discharge current speed [35]. The modified Diendorfer-Uman (MDU) model considers the influence of a decrease in speed with height, as occurring in nature, on the channel current and the charge distributions, as well as on the remote electric and magnetic fields.

The current is defined in terms of the average return stroke speed $V_{av}(z')$ and the average downward speed of the discharge current $U_{av}(z')$. For a return-stroke speed $v(z')$ and a downward speed of the discharge current $u(z')$, both functions of z',

$$V_{av}(z') = \frac{z'}{t_u(z')} = \frac{z''}{\int_{z''=0}^{z'} \frac{dz''}{v(z'')}} \tag{3.16}$$

$$U_{av}(z') = \frac{z'}{t_d(z')} = \frac{z''}{\int_{z''=0}^{z'} \frac{dz''}{u(z'')}} \tag{3.17}$$

where $t_u(z')$ is the time required for the return stroke to reach a height z' and $t_d(z')$ is the time required for the discharge currents at height z' to reach ground. Then the current is given by

$$i(z',t) = i\left(0, t + \frac{z'}{c}\right) - i\left(0, \frac{z'}{V_{av}(z')} + \frac{z'}{U_{av}(z')}\right) e^{-\left(t - \frac{z'}{V_{av}(z')}\right)/\tau_D} \quad t \geq \frac{z'}{V_{av}(z')} \tag{3.18}$$

3.7 PAN-LIEW (PL) MODEL

The Pan-Liew (PL) circuit model comprises of two separate current components: (1) the fast breakdown discharge current i_B, and (2) the slow corona discharge current i_C [3]. As shown in Figure 3.4, the leader channel is divided into several sections, and each one is equivalent to a capacitance-resistance circuit. The return stroke is assumed to propagate upwards with a constant speed, closing the switches in progression to signify the discharging of the section it passes. Similar to the DU model, the charge stored along the channel is assumed to decrease exponentially with height and the discharge current is assumed to propagate at the speed of light, c. The return stroke current at the channel base is obtained by integrating all the discharge currents along the channel.

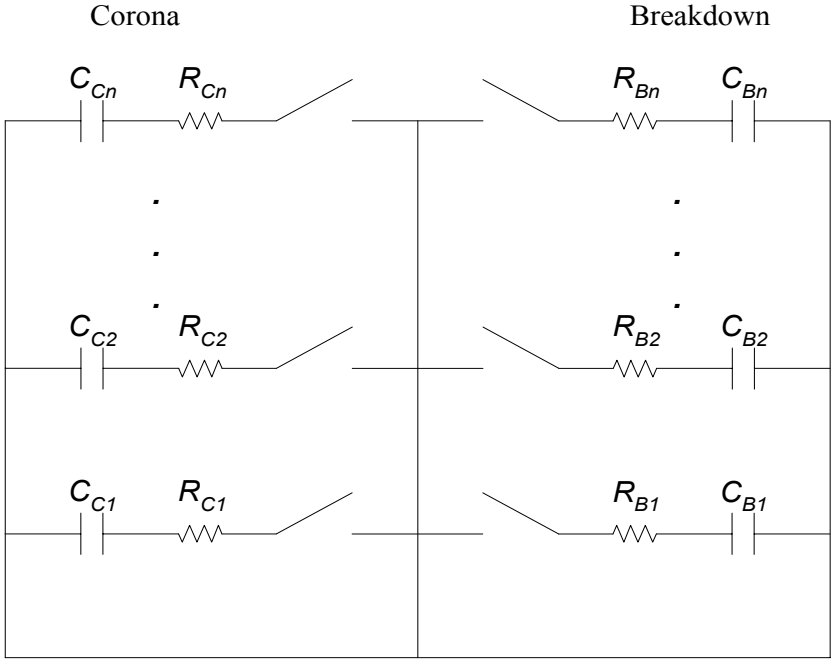

Figure 3.4 Equivalent circuit of leader channel in the PL model

According to the circuit in Figure 3.4, the discharge current in each section is given by

$$\begin{aligned} i_n &= i_{Cn} + i_{Bn} \\ &= \frac{U_0}{R_{Cn}} e^{-t/R_{Cn}C_{Cn}} + \frac{U_0}{R_{Bn}} e^{-t/R_{Bn}C_{Bn}} \end{aligned} \tag{3.19}$$

where U_0 is the initial voltage of the capacitors.

The height of each section was set to l, and the return stroke speed set to v. Subsequently, the delay constant w was defined as the time interval between which the return stroke leaves the base of a section and the discharging current of that section reaches its base.

$$w = \left(\frac{l}{v} + \frac{l}{c} \right) \tag{3.20}$$

Therefore, for the circuit model of n sections, the total return stroke current at height z' is given by:

$$\begin{aligned} i(z',t) &= \sum_{n=1+z'/l}^{H/l} i_n(t - nw + z'/c)\ \ u(t - nw + z'/c) \qquad t \geq w + z'/v \\ i(z',t) &= 0 \qquad\qquad\qquad\qquad\qquad\qquad\qquad\qquad\qquad\qquad t < w + z'/v \end{aligned} \tag{3.21}$$

where H is the height of the lightning channel and $u(t)$ is the Heaviside step function:

$$u(t) = \begin{cases} 1 & t \geq 0 \\ 0 & t < 0 \end{cases} \tag{3.22}$$

The circuit parameter values were set as shown in Table 3.2 and the channel-base current waveform, reproduced in Figure 3.4, was very similar to that given by the DU model in Figure 3.3. The peak current value obtained was 30 kA and the maximum current-time derivative was about 93 kA/μs.

Table 3.2 Circuit Parameter Values Used in the PL Model

H (m)	5000
l (m)	5
n	1000
U_0 (MV)	1.97
R_{Cn} (kΩ)	$6.4e^{n/1100}$
R_{Bn} (kΩ)	$0.4e^{n/52}$
C_{Cn} (nF)	$0.63e^{-n/1100}$
C_{Bn} (nF)	$0.9e^{-n/52}$

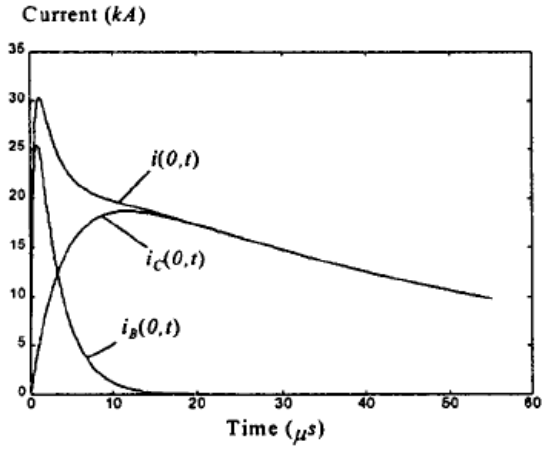

Figure 3.5 Channel-base current waveform for the PL model

This is the only model mentioned that allows the analysis of the effect of an added resistance at the base of the lightning channel. The added resistance could represent the current limiting lightning rod in lightning protection systems. And the results obtained showed that with an added resistance of 35 kΩ, the channel current was effectively reduced to 56.2 A [3].

3.8 LUPO *ET AL.*'S MODEL

Lupò *et al.*'s model [6] considered a tortuous lightning stroke path as opposed to the straight channel approximation adopted by most models to determine the electromagnetic fields due to the lightning return stroke current. The effect of channel tortuosity was studied using a piecewise representation of the lightning channel by means of arbitrarily oriented radiators.

For a unit step-wave representation of the current and charge distributions along the discharge channel,

$$i(z',t) = u\left(t - \frac{z'}{v}\right) \times \left[u(z') - u(z'-h)\right] \tag{3.23}$$

$$\begin{aligned} \lambda(z',t) = -\Bigg\{ & tu(t)\delta(z') - \left(t - \frac{h}{v}\right)u\left(t - \frac{h}{v}\right)\delta(z'-h) \\ & - \frac{1}{v}u\left(t - \frac{z'}{v}\right)\left[u(z') - u(z'-h)\right]\Bigg\} \end{aligned} \tag{3.24}$$

the closed-form solution for the fields were found to be

$$\begin{aligned} H_r &= 0 \\ H_z &= 0 \\ H_\phi &= \int_0^h \frac{1}{4\pi}\left[\frac{r}{R_r^{\,3}}u\left(t - \frac{z'}{v} - \frac{R_r}{c}\right) + \frac{r}{cR_r^{\,2}}\delta\left(t - \frac{z'}{v} - \frac{R_r}{c}\right)\right]dz' \end{aligned} \tag{3.25}$$

$$E_r = \frac{r\left[-tu\left(t-\frac{\sqrt{r^2+z^2}}{c}\right)\right]}{4\pi\varepsilon_0\left(\sqrt{r^2+z^2}\right)^3} + \frac{r\left[\left(t-\frac{h}{v}\right)u\left(t-\frac{h}{v}-\frac{\sqrt{r^2+(z-h)^2}}{c}\right)\right]}{4\pi\varepsilon_0\left(\sqrt{r^2+(z-h)^2}\right)^3}$$
$$+\int_0^h \frac{1}{4\pi v\varepsilon_0}\left[\frac{r}{R_r^{\,3}}u\left(t-\frac{z'}{v}-\frac{R_r}{c}\right)+\frac{1}{cR_r^{\,2}}\delta\left(t-\frac{z'}{v}-\frac{R_r}{c}\right)\right]dz'$$

$$E_z = \frac{z\left[-tu\left(t-\frac{\sqrt{r^2+z^2}}{c}\right)\right]}{4\pi\varepsilon_0\left(\sqrt{r^2+z^2}\right)^3} + \frac{(z-h)\left[\left(t-\frac{h}{v}\right)u\left(t-\frac{h}{v}-\frac{\sqrt{r^2+(z-h)^2}}{c}\right)\right]}{4\pi\varepsilon_0\left(\sqrt{r^2+(z-h)^2}\right)^3}$$
$$+\int_0^h \frac{1}{4\pi v\varepsilon_0}\left[\frac{z-z'}{R_r^{\,3}}u\left(t-\frac{z'}{v}-\frac{R_r}{c}\right)+\frac{z-z'}{cR_r^{\,2}}\delta\left(t-\frac{z'}{v}-\frac{R_r}{c}\right)\right]$$
$$-\frac{\mu_0}{4\pi}\frac{1}{R_r}\delta\left(t-\frac{z'}{v}-\frac{R_r}{c}\right)dz'$$

$$E_\phi = 0 \tag{3.26}$$

where u is the Heaviside step function, δ is the Dirac delta function and R_r is the distance between the radiator and the observation point [6].

The vertical electric field and azimuthal magnetic fields at ground were computed at various distances by superimposing the fields due to each individual radiator forming the lighting channel [36].

CHAPTER 4

DEVELOPMENT OF DISTRIBUTED CIRCUIT MODEL

Previous lightning return stroke models are successful in reproducing the return stroke current, and the remote electric and magnetic fields from experimental observations. They have also been employed to establish the effectiveness of lightning protection systems. But the majority of these models assume infinite ground conductivity which limits their application to cases where the propagation path or channel base does not include an element of finite conductivity. The PL model caters for such cases and allows the analysis of the effect of resistance at the base of the lightning channel on the return stroke current. However, the PL model has failed to account for the effect of inductance along the lightning channel.

4.1 ASSUMPTIONS

4.1.1 Discharge Current Components

The stepped leader process is viewed to lower charges from a charge centre in the cloud. As the stepped leader propagates downwards, it deposits charges along the

channel. Due the large potential of the charges, a radial electric field is created and charges are pushed away from the channel core, leading to the formation of a corona sheath.

As the return stroke travels upwards along the channel, it discharges the deposited charges on both the channel core and the corona envelope. Therefore, in the proposed model, the discharge current is assumed to consist of two separate components: (1) a fast breakdown channel current, i_{CH}, and (2) a slower corona sheath discharge current, i_{CO}.

4.1.2 Charge Distribution along the Leader Channel

Various charge distributions have been proposed and studied. *Thum et al.* (1982) [37, 38] studied the growth of corona streamers from a lightning rod. They considered the stepped leader as a continuously descending conical structure with the apex at the cloud. Charge on the leader increases linearly from within the cloud to the lower end of the leader. In *Rizk's* model (1994) [39], the distribution of charges is also linearly increasing from the base of the cloud to the base of the leader. But the charge distributions proposed in the MTL, MULS, DU and PL models was taken to increase exponentially from the cloud base to the base of the leader.

So, it is chosen in the proposed model for the charge profile to be exponentially decreasing with height. This allows for a legitimate comparison with previous models. This profile applies to charges on both the breakdown channel core and corona sheath.

4.1.3 Height of Lightning Channel

The height of the lightning channel varies with geographical location. One of the most common values assumed is 5 km. Hence, as in the PL model, it is chosen as the channel height in the proposed model.

4.1.4 Return Stroke and Discharge Current Speeds

The average return stroke speed is $1.3\pm0.3\times10^8$ m/s for long-channels exceeding 500 m in length, and $1.9\pm0.7\times10^8$ m/s for channel lengths less than 500 m [15]. These values were obtained by *Mach et al.* who also showed that the return stroke speed decreases with height. But other than in the MDU model, most models neglect the variation of return stroke speed with height

The return stroke speed v is chosen to be constant with height with a value of 1.3×10^8 m/s since the channel length was set to 5 km. And as with most models, the discharge current speed is assumed to be the speed of light, c (3×10^8 m/s).

4.2 PROPOSED MODEL

The intention of new model is to consider the effect of inductance and resistance on the lightning return stroke current. It bears resemblance to the PL model, which is why the basic assumptions proposed are similar to those taken by the PL model. Additional distributed inductance components are included in both the breakdown channel core and the corona sheath.

4.2.1 Equivalent Circuit

The equivalent circuit of the proposed lightning channel model is shown in Figure 4.1. The circuit is made up of two different halves: (1) one representing the breakdown channel, with subscript *CH*, and (2) the other representing the corona sheath, with subscript *CO*. The entire lightning channel consists of a total of *m* sections (seen horizontally), where each section, comprises of a breakdown channel element and a corona sheath element.

The corona sheath was formed when the charges deposited by the stepped leader set up a radial electric field. Hence, when the corona sheath is discharged by the return stroke, the charges flow radially inwards towards the core before propagating towards ground. This explains the positioning of the breakdown channel at the centre of the circuit. On top of that, it also reflects that the channel core is dynamic. As the return stroke discharges each section, the discharge current flows into the channel core. It is modelled that the core "reacts" to the current flow, influencing the discharge of subsequent sections.

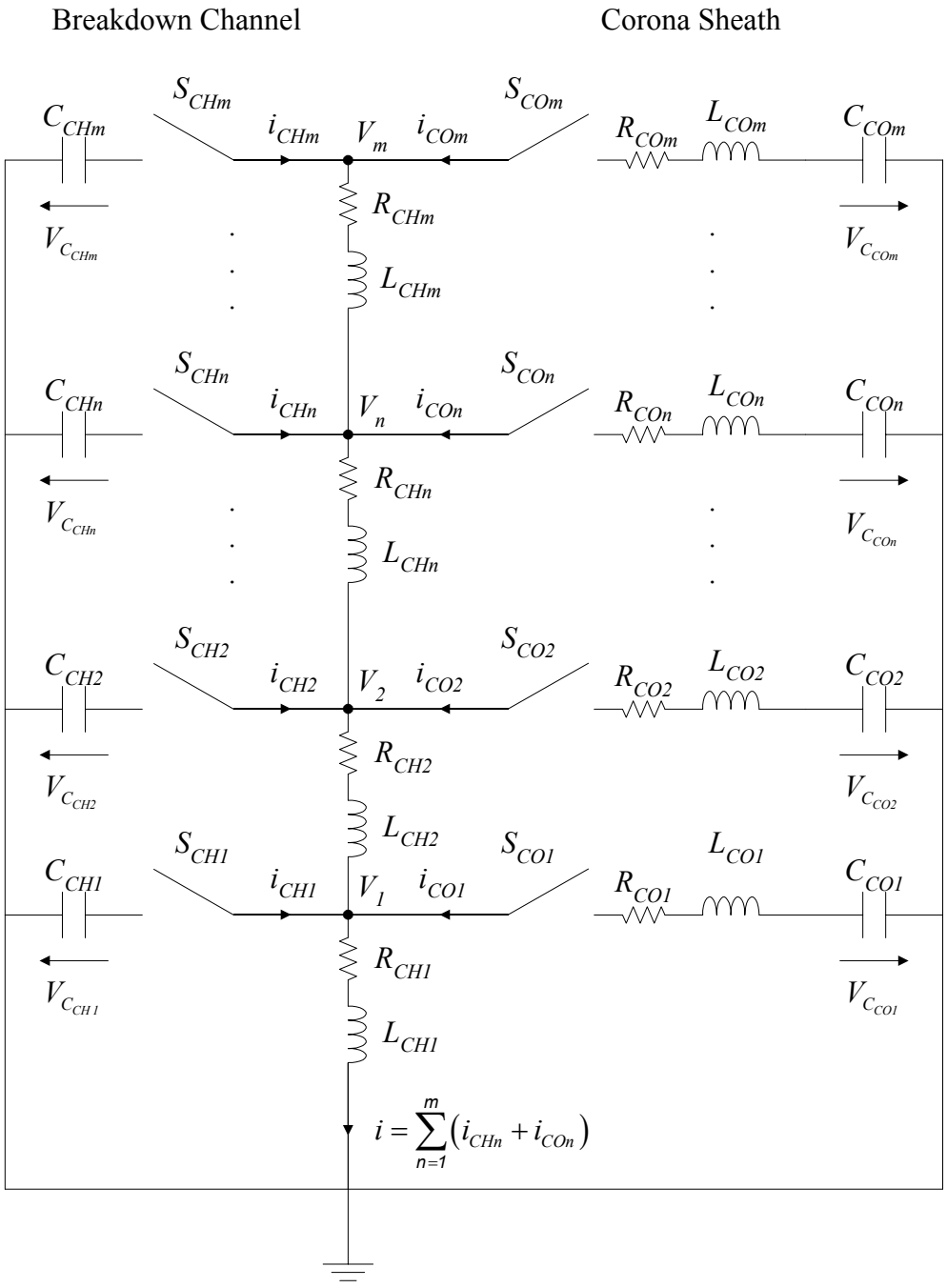

Figure 4.1 Equivalent circuit of lightning channel

As the stepped leader travels downward, forming the channel, each capacitor stores charges at its respective height. When the leader arrives at the ground, the return stroke is initiated and propagates upward with a constant speed *v*. For a constant step length of *h*, the return stroke wave front reached the first section after a time interval of *h/v*. Therefore the switches of section 1, S_{CH1} and S_{CO1}, are closed at $t = h/v$, initiating the

discharge of the charges deposited in that section by the stepped leader. The discharge currents, i_{CH1} and i_{CO1}, flow into the return stroke channel and propagate downward at the speed of light c. The current reaches ground only after a time of h/c, even though the discharging process has already begun. Therefore, there a delay of $(h/v+h/c)$ from the time the return stroke wave front leaves ground to the time the discharge current reaches ground.

At a time interval of h/v after the section 1 begins discharging, the return stroke wave front reaches section 2 closing the second set of switches S_{CH2} and S_{CO2}. Similarly, the discharge currents of section 2, i_{CH2} and i_{CO2}, reach ground after a time interval of $2(h/v+h/c)$.

Eventually, the return stroke wave front reaches the base of the cloud, closing the final set of switches, S_{CHm} and S_{COm}. And the discharge currents of the last section reach ground after a time interval of $(H/h)(h/v+h/c)$, where H is the height of the lightning channel. Hence, we can define the number of sections m as

$$m = H/h \tag{4.1}$$

An important parameter of the proposed model is the time period from which the return stroke leaves the bottom of a section to the time when the discharge currents of that section reaches the bottom of the section. Hence the time delay constant w is defined as

$$w = h\left(1/v + 1/c\right) \tag{4.2}$$

For a general section n, the return stroke wave front leaves the previous section at $t = (n\text{-}1)h/v$ and reaches the n-th section at $t = nh/v$. The n-th section begins to discharge. The discharging process is dependent on the current and voltage states of the (n-1) sections below it. At $t = nh/v+h/c$, the discharge currents of section n reaches section (n-1) and affects the discharge of the capacitors of section (n-1). Consequently, the discharge currents of section n are also affected. At $t = nh/v+2h/c$, the discharge currents of section n and section (n-1), with their new current profiles, reach section (n-2) and affects the discharge of the capacitors of section (n-2). Similarly, the discharge currents of sections 1 to (n-3) are affected at regular intervals of h/c and take on their respective new profiles.

Ultimately, the effect due to the discharge of section n is reflected at ground only from $t = nw$ to $t = (n+1)w$. To simplify analysis, the effects of all the intermediate changes are ignored. To maintain the dynamic property of the channel core, all of the changes are reflected only at the time the discharge current reaches the base of the lightning channel. Equivalently, the switches of section n in the equivalent circuit can be viewed to be closed at $t = nw$ when analysing the lightning return stroke current at the base of the lightning channel.

4.2.2 Derivation of Equations Defining Return Stroke Current

For the time interval between nw to $(n+1)w$, the functions defining the discharge currents for sections 1 to (n-1) change due to the introduction of section n. Hence, the equations governing the discharge currents have to be defined separately for each time interval. The time limits for each section is defined as

$$t_n = nw \tag{4.3}$$

A. Section 1 ($t_1 \le t \le t_2$):

For the breakdown channel,

$$V_{C_{CH1}} + R_{CH1}\left(i_{CH1} + i_{CO1}\right) + L_{CH1}\left(\frac{di_{CH1}}{dt} + \frac{di_{CO1}}{dt}\right) = 0 \tag{4.4}$$

since the voltage across a resistor is given by

$$V_R = Ri_R \tag{4.5}$$

and the voltage across an inductor is given by

$$V_L = L\frac{di_L}{dt} \tag{4.6}$$

Multiplying equation (4.4) with C_{CH1}, followed by differentiating with respect to time, t

$$i_{CH1} + C_{CH1}R_{CH1}\left(\frac{di_{CH1}}{dt} + \frac{di_{CO1}}{dt}\right) + C_{CH1}L_{CH1}\left(\frac{d^2i_{CH1}}{dt} + \frac{d^2i_{CO1}}{dt}\right) = 0 \tag{4.7}$$

since the current through a capacitor is given by

$$i_C = C\frac{dV_C}{dt} \tag{4.8}$$

For the corona sheath,

$$\begin{aligned} V_{C_{CO1}} + R_{CH1}i_{CH1} + \left(R_{CH1} + R_{CO1}\right)i_{CO1} + \\ L_{CH1}\frac{di_{CH1}}{dt} + \left(L_{CH1} + L_{CO1}\right)\frac{di_{CO1}}{dt} = 0 \end{aligned} \tag{4.9}$$

Multiplying equation (4.9) with C_{CO1}, followed by differentiating with respect to time, t

$$\begin{aligned} i_{CO1} + C_{CO1}R_{CH1}\frac{di_{CH1}}{dt} + C_{CO1}\left(R_{CH1} + R_{CO1}\right)\frac{di_{CO1}}{dt} + \\ C_{CO1}L_{CH1}\frac{d^2i_{CH1}}{dt} + C_{CO1}\left(L_{CH1} + L_{CO1}\right)\frac{d^2i_{CO1}}{dt} = 0 \end{aligned} \tag{4.10}$$

Rewriting equation (4.4) and (4.9) in matrix form,

$$\begin{bmatrix} V_{C_{CH1}} \\ V_{C_{CO1}} \end{bmatrix} + \begin{bmatrix} R_{CH1} & R_{CH1} \\ R_{CH1} & R_{CH1} + R_{CO1} \end{bmatrix} \begin{bmatrix} i_{CH1} \\ i_{CO1} \end{bmatrix} + \begin{bmatrix} L_{CH1} & L_{CH1} \\ L_{CH1} & L_{CH1} + L_{CO1} \end{bmatrix} \begin{bmatrix} \frac{di_{CH1}}{dt} \\ \frac{di_{CO1}}{dt} \end{bmatrix} = 0 \tag{4.11}$$

And rewriting equations (4.7) and (4.10) in matrix form,

$$\begin{bmatrix} \frac{1}{C_{CH1}} & 0 \\ 0 & \frac{1}{C_{CO1}} \end{bmatrix} \begin{bmatrix} i_{CH1} \\ i_{CO1} \end{bmatrix} + \begin{bmatrix} R_{CH1} & R_{CH1} \\ R_{CH1} & R_{CH1} + R_{CO1} \end{bmatrix} \begin{bmatrix} \frac{di_{CH1}}{dt} \\ \frac{di_{CO1}}{dt} \end{bmatrix} + \begin{bmatrix} L_{CH1} & L_{CH1} \\ L_{CH1} & L_{CH1} + L_{CO1} \end{bmatrix} \begin{bmatrix} \frac{d^2 i_{CH1}}{dt^2} \\ \frac{d^2 i_{CO1}}{dt^2} \end{bmatrix} = 0 \tag{4.12}$$

The initial conditions at $t = t_1$ are

$$\begin{bmatrix} i_{CH1} \\ i_{CO1} \\ V_{C_{CH1}} \\ V_{C_{CO1}} \end{bmatrix} = \begin{bmatrix} 0 \\ 0 \\ U_{CH1} \\ U_{CO1} \end{bmatrix} \tag{4.13}$$

where U_{chn} and U_{con} are the initial voltages of the capacitors in section n. Equation (4.13) is based on the current continuity property of an inductor and the voltage continuity property of a capacitor.

Substituting the initial conditions for the voltages into equation (4.11),

$$\begin{bmatrix} U_{CH1} \\ U_{CO1} \end{bmatrix} + \begin{bmatrix} R_{CH1} & R_{CH1} \\ R_{CH1} & R_{CH1} + R_{CO1} \end{bmatrix} \begin{bmatrix} i_{CH1}(t_1) \\ i_{CO1}(t_1) \end{bmatrix} + \begin{bmatrix} L_{CH1} & L_{CH1} \\ L_{CH1} & L_{CH1} + L_{CO1} \end{bmatrix} \begin{bmatrix} \dfrac{di_{CH1}(t_1)}{dt} \\ \dfrac{di_{CO1}(t_1)}{dt} \end{bmatrix} = 0 \tag{4.14}$$

Therefore, the initial conditions to the second order differential equation (4.12) are

$$\begin{bmatrix} \dfrac{di_{CH1}(t_1)}{dt} \\ \dfrac{di_{CO1}(t_1)}{dt} \end{bmatrix} = -\begin{bmatrix} L_{CH1} & L_{CH1} \\ L_{CH1} & L_{CH1} + L_{CO1} \end{bmatrix}^{-1} \begin{bmatrix} U_{CH1} \\ U_{CO1} \end{bmatrix} - \begin{bmatrix} L_{CH1} & L_{CH1} \\ L_{CH1} & L_{CH1} + L_{CO1} \end{bmatrix}^{-1} \begin{bmatrix} R_{CH1} & R_{CH1} \\ R_{CH1} & R_{CH1} + R_{CO1} \end{bmatrix} \begin{bmatrix} i_{CH1}(t_1) \\ i_{CO1}(t_1) \end{bmatrix} \tag{4.15}$$

and

$$\begin{bmatrix} i_{CH1} \\ i_{CO1} \end{bmatrix} = \begin{bmatrix} 0 \\ 0 \end{bmatrix} \tag{4.16}$$

B. Section 2 ($t_2 \le t \le t_3$):

For the breakdown channel of section 2,

$$\begin{aligned} &V_{C_{CH2}} + R_{CH1}(i_{CH1} + i_{CO1}) + L_{CH1}\frac{d}{dt}(i_{CH1} + i_{CO1}) + \\ &(R_{CH1} + R_{CH2})(i_{CH2} + i_{CO2}) + (L_{CH1} + L_{CH2})\frac{d}{dt}(i_{CH2} + i_{CO2}) = 0 \end{aligned} \tag{4.17}$$

Multiplying with C_{CH2}, followed by differentiating with respect to time, t

$$\begin{aligned} &i_{CH2} + C_{CH2}R_{CH1}\left(\frac{di_{CH1}}{dt} + \frac{di_{CO1}}{dt}\right) + C_{CH2}L_{CH1}\left(\frac{d^2i_{CH1}}{dt^2} + \frac{d^2i_{CO1}}{dt^2}\right) + \\ &C_{CH2}(R_{CH1} + R_{CH2})\left(\frac{di_{CH2}}{dt} + \frac{di_{CO2}}{dt}\right) + C_{CH2}(L_{CH1} + L_{CH2})\left(\frac{d^2i_{CH2}}{dt^2} + \frac{d^2i_{CO2}}{dt^2}\right) = 0 \end{aligned} \tag{4.18}$$

For the corona sheath of section 2,

$$\begin{aligned} &V_{C_{CO2}} + R_{CH1}\left(i_{CH1} + i_{CO1}\right) + L_{CH1}\frac{d}{dt}\left(i_{CH1} + i_{CO1}\right) + \\ &\left(R_{CH1}+R_{CH2}\right)i_{CH2} + \left(R_{CH1}+R_{CH2}+R_{CO2}\right)i_{CO2} + \\ &\left(L_{CH1} + L_{CH2}\right)\frac{di_{CH2}}{dt} + \left(L_{CH1} + L_{CH2} + L_{CO2}\right)\frac{di_{CO2}}{dt} = 0 \end{aligned} \tag{4.19}$$

Multiplying with C_{CO2}, followed by differentiating with respect to time, t

$$\begin{aligned} &i_{CO2} + C_{CO2}R_{CH1}\left(\frac{di_{CH1}}{dt} + \frac{di_{CO1}}{dt}\right) + C_{CO2}L_{CH1}\left(\frac{d^2i_{CH1}}{dt^2} + \frac{d^2i_{CO1}}{dt^2}\right) + \\ &C_{CO2}\left(R_{CH1}+R_{CH2}\right)\frac{di_{CH2}}{dt} + C_{CO2}\left(R_{CH1}+R_{CH2}+R_{CO2}\right)\frac{di_{CO2}}{dt} + \\ &C_{CO2}\left(L_{CH1} + L_{CH2}\right)\frac{d^2i_{CH2}}{dt^2} + C_{CO2}\left(L_{CH1} + L_{CH2} + L_{CO2}\right)\frac{d^2i_{CO2}}{dt^2} = 0 \end{aligned} \tag{4.20}$$

For the breakdown channel of section 1,

$$\begin{aligned} &V_{C_{CH1}} + R_{CH1}\left(i_{CH1} + i_{CO1} + i_{CH2} + i_{CO2}\right) + \\ &L_{CH1}\frac{d}{dt}\left(i_{CH1} + i_{CO1} + i_{CH2} + i_{CO2}\right) = 0 \end{aligned} \tag{4.21}$$

Multiplying with C_{CH1}, followed by differentiating with respect to time, t

$$\begin{aligned} &i_{CH1} + C_{CH1}R_{CH1}\left(\frac{di_{CH1}}{dt} + \frac{di_{CO1}}{dt} + \frac{di_{CH2}}{dt} + \frac{di_{CO2}}{dt}\right) + \\ &C_{CH1}L_{CH1}\left(\frac{d^2i_{CH1}}{dt} + \frac{d^2i_{CO1}}{dt} + \frac{d^2i_{CH2}}{dt} + \frac{d^2i_{CO2}}{dt}\right) = 0 \end{aligned} \tag{4.22}$$

For the corona sheath of section 1,

$$\begin{aligned} &V_{C_{CO1}} + R_{CH1}\left(i_{CH1} + i_{CH2} + i_{CO2}\right) + \left(R_{CH1}+R_{CO1}\right)i_{CO1} + \\ &L_{CH1}\frac{d}{dt}\left(i_{CH1} + i_{CH2} + i_{CO2}\right) + \left(L_{CH1} + L_{CO1}\right)\frac{di_{CO1}}{dt} = 0 \end{aligned} \tag{4.23}$$

Multiplying with C_{CO1}, followed by differentiating with respect to time, t

$$\begin{aligned} &i_{CO1} + C_{CO1}R_{CH1}\left(\frac{di_{CH1}}{dt} + \frac{di_{CH2}}{dt} + \frac{di_{CO2}}{dt}\right) + C_{CO1}\left(R_{CH1} + R_{CO1}\right)\frac{di_{CO1}}{dt} + \\ &C_{CO1}L_{CH1}\left(\frac{d^2i_{CH1}}{dt} + \frac{d^2i_{CH2}}{dt} + \frac{d^2i_{CO2}}{dt}\right) + C_{CO1}\left(L_{CH1} + L_{CO1}\right)\frac{d^2i_{CO1}}{dt} = 0 \end{aligned} \tag{4.24}$$

Rewriting the voltage equations (4.17), (4.19), (4.21) and(4.23) in matrix form,

$$\begin{bmatrix} V_{C_{CH1}} \\ V_{C_{CO1}} \\ V_{C_{CH2}} \\ V_{C_{CO2}} \end{bmatrix} + \begin{bmatrix} R_{CH1} & R_{CH1} & R_{CH1} & R_{CH1} \\ R_{CH1} & R_{CH1} + R_{CO1} & R_{CH1} & R_{CH1} \\ R_{CH1} & R_{CH1} & R_{CH1} + R_{CH2} & R_{CH1} + R_{CH2} \\ R_{CH1} & R_{CH1} & R_{CH1} + R_{CH2} & R_{CH1} + R_{CH2} + R_{CO2} \end{bmatrix} \begin{bmatrix} i_{CH1} \\ i_{CO1} \\ i_{CH2} \\ i_{CO2} \end{bmatrix} + \begin{bmatrix} L_{CH1} & L_{CH1} & L_{CH1} & L_{CH1} \\ L_{CH1} & L_{CH1} + L_{CO1} & L_{CH1} & L_{CH1} \\ L_{CH1} & L_{CH1} & L_{CH1} + L_{CH2} & L_{CH1} + L_{CH2} \\ L_{CH1} & L_{CH1} & L_{CH1} + L_{CH2} & L_{CH1} + L_{CH2} + L_{CO2} \end{bmatrix} \begin{bmatrix} \frac{di_{CH1}}{dt} \\ \frac{di_{CO1}}{dt} \\ \frac{di_{CH2}}{dt} \\ \frac{di_{CO2}}{dt} \end{bmatrix} = 0 \tag{4.25}$$

And rewriting equations (4.18), (4.20), (4.22) and (4.24) in matrix form,

$$\begin{bmatrix} \frac{1}{C_{CH1}} & 0 & 0 & 0 \\ 0 & \frac{1}{C_{CO1}} & 0 & 0 \\ 0 & 0 & \frac{1}{C_{CH2}} & 0 \\ 0 & 0 & 0 & \frac{1}{C_{CO2}} \end{bmatrix} \begin{bmatrix} i_{CH1} \\ i_{CO1} \\ i_{CH2} \\ i_{CO2} \end{bmatrix} +$$

$$\begin{bmatrix} R_{CH1} & R_{CH1} & R_{CH1} & R_{CH1} \\ R_{CH1} & R_{CH1}+R_{CO1} & R_{CH1} & R_{CH1} \\ R_{CH1} & R_{CH1} & R_{CH1}+R_{CH2} & R_{CH1}+R_{CH2} \\ R_{CH1} & R_{CH1} & R_{CH1}+R_{CH2} & R_{CH1}+R_{CH2}+R_{CO2} \end{bmatrix} \begin{bmatrix} \frac{di_{CH1}}{dt} \\ \frac{di_{CO1}}{dt} \\ \frac{di_{CH2}}{dt} \\ \frac{di_{CO2}}{dt} \end{bmatrix} +$$

$$\begin{bmatrix} L_{CH1} & L_{CH1} & L_{CH1} & L_{CH1} \\ L_{CH1} & L_{CH1}+L_{CO1} & L_{CH1} & L_{CH1} \\ L_{CH1} & L_{CH1} & L_{CH1}+L_{CH2} & L_{CH1}+L_{CH2} \\ L_{CH1} & L_{CH1} & L_{CH1}+L_{CH2} & L_{CH1}+L_{CH2}+L_{CO2} \end{bmatrix} \begin{bmatrix} \frac{d^2 i_{CH1}}{dt^2} \\ \frac{d^2 i_{CO1}}{dt^2} \\ \frac{d^2 i_{CH2}}{dt^2} \\ \frac{d^2 i_{CO2}}{dt^2} \end{bmatrix} = 0 \tag{4.26}$$

The initial conditions $t = t_2$ are

$$\begin{bmatrix} i_{CH2} \\ i_{CO2} \\ V_{C_{CH2}} \\ V_{C_{CO2}} \end{bmatrix} = \begin{bmatrix} 0 \\ 0 \\ U_{CH2} \\ U_{CO2} \end{bmatrix} \tag{4.27}$$

and

$$\begin{bmatrix} i_{CH1} \\ i_{CO1} \\ V_{C_{CH1}} \\ V_{C_{CO1}} \end{bmatrix} = \begin{bmatrix} i_{CH1}(t_2) \\ i_{CO1}(t_2) \\ V_{CH1}(t_2) \\ V_{CO1}(t_2) \end{bmatrix} \tag{4.28}$$

where the voltages are obtained from the voltage matrix equation of the previous section, i.e. equation (4.11).

Substituting the initial conditions for the voltages into equation (4.25),

$$\begin{bmatrix} V_{C_{CH1}}(t_2) \\ V_{C_{CO1}}(t_2) \\ U_{CH2} \\ U_{CO2} \end{bmatrix} + \begin{bmatrix} R_{CH1} & R_{CH1} & R_{CH1} & R_{CH1} \\ R_{CH1} & R_{CH1}+R_{CO1} & R_{CH1} & R_{CH1} \\ R_{CH1} & R_{CH1} & R_{CH1}+R_{CH2} & R_{CH1}+R_{CH2} \\ R_{CH1} & R_{CH1} & R_{CH1}+R_{CH2} & R_{CH1}+R_{CH2}+R_{CO2} \end{bmatrix} \begin{bmatrix} i_{CH1}(t_2) \\ i_{CO1}(t_2) \\ i_{CH2}(t_2) \\ i_{CO2}(t_2) \end{bmatrix} +$$

$$\begin{bmatrix} L_{CH1} & L_{CH1} & L_{CH1} & L_{CH1} \\ L_{CH1} & L_{CH1}+L_{CO1} & L_{CH1} & L_{CH1} \\ L_{CH1} & L_{CH1} & L_{CH1}+L_{CH2} & L_{CH1}+L_{CH2} \\ L_{CH1} & L_{CH1} & L_{CH1}+L_{CH2} & L_{CH1}+L_{CH2}+L_{CO2} \end{bmatrix} \begin{bmatrix} \frac{di_{CH1}(t_2)}{dt} \\ \frac{di_{CO1}(t_2)}{dt} \\ \frac{di_{CH2}(t_2)}{dt} \\ \frac{di_{CO2}(t_2)}{dt} \end{bmatrix} = 0 \tag{4.29}$$

Therefore, the initial conditions of equation (4.26) are

$$\begin{bmatrix} \frac{di_{CH1}(t_2)}{dt} \\ \frac{di_{CO1}(t_2)}{dt} \\ \frac{di_{CH2}(t_2)}{dt} \\ \frac{di_{CO2}(t_2)}{dt} \end{bmatrix} = -\begin{bmatrix} L_{CH1} & L_{CH1} & L_{CH1} & L_{CH1} \\ L_{CH1} & L_{CH1}+L_{CO1} & L_{CH1} & L_{CH1} \\ L_{CH1} & L_{CH1} & L_{CH1}+L_{CH2} & L_{CH1}+L_{CH2} \\ L_{CH1} & L_{CH1} & L_{CH1}+L_{CH2} & L_{CH1}+L_{CH2}+L_{CO2} \end{bmatrix}^{-1} \begin{bmatrix} V_{C_{CH1}}(t_2) \\ V_{C_{CO1}}(t_2) \\ U_{CH2} \\ U_{CO2} \end{bmatrix} -$$

$$\begin{bmatrix} L_{CH1} & L_{CH1} & L_{CH1} & L_{CH1} \\ L_{CH1} & L_{CH1}+L_{CO1} & L_{CH1} & L_{CH1} \\ L_{CH1} & L_{CH1} & L_{CH1}+L_{CH2} & L_{CH1}+L_{CH2} \\ L_{CH1} & L_{CH1} & L_{CH1}+L_{CH2} & L_{CH1}+L_{CH2}+L_{CO2} \end{bmatrix}^{-1}$$

$$\begin{bmatrix} R_{CH1} & R_{CH1} & R_{CH1} & R_{CH1} \\ R_{CH1} & R_{CH1}+R_{CO1} & R_{CH1} & R_{CH1} \\ R_{CH1} & R_{CH1} & R_{CH1}+R_{CH2} & R_{CH1}+R_{CH2} \\ R_{CH1} & R_{CH1} & R_{CH1}+R_{CH2} & R_{CH1}+R_{CH2}+R_{CO2} \end{bmatrix} \begin{bmatrix} i_{CH1}(t_2) \\ i_{CO1}(t_2) \\ i_{CH2}(t_2) \\ i_{CO2}(t_2) \end{bmatrix} \tag{4.30}$$

and

$$\begin{bmatrix} i_{CH1} \\ i_{CO1} \\ i_{CH2} \\ i_{CO2} \end{bmatrix} = \begin{bmatrix} i_{CH1}(t_2) \\ i_{CO1}(t_2) \\ 0 \\ 0 \end{bmatrix} \tag{4.31}$$

C. Section n ($t_n \le t \le t_{n+1}$):

For the breakdown channel of section n,

$$V_{C_{CHn}} + \sum_{j=1}^{n} \left[\left(\sum_{k=1}^{j} R_{CHk} \right) \left(i_{CHj} + i_{COj} \right) + \left(\sum_{k=1}^{j} L_{CHj} \right) \frac{d}{dt} \left(i_{CHj} + i_{COj} \right) \right] = 0 \tag{4.32}$$

Multiplying with C_{CHn}, followed by differentiating with respect to time, t

$$i_{CHn} + C_{CHn} \sum_{j=1}^{n} \left[\left(\sum_{k=1}^{j} R_{CHk} \right) \left(\frac{di_{CHj}}{dt} + \frac{di_{COj}}{dt} \right) + \left(\sum_{k=1}^{j} L_{CHj} \right) \left(\frac{d^2 i_{CHj}}{dt^2} + \frac{d^2 i_{COj}}{dt^2} \right) \right] = 0 \tag{4.33}$$

For the corona sheath of section n,

$$V_{C_{COn}} + \sum_{j=1}^{n} \left[\left(\sum_{k=1}^{j} R_{CHk} \right) \left(i_{CHj} + i_{COj} \right) + \left(\sum_{k=1}^{j} L_{CHj} \right) \frac{d}{dt} \left(i_{CHj} + i_{COj} \right) \right] + R_{COn} i_{COn} + L_{COn} \frac{di_{COn}}{dt} = 0 \tag{4.34}$$

Multiplying with C_{COn}, followed by differentiating with respect to time, t

$$i_{COn} + C_{COn} \sum_{j=1}^{n} \left[\begin{array}{l} \left(\sum_{k=1}^{j} R_{CHk} \right) \left(\frac{di_{CHj}}{dt} + \frac{di_{COj}}{dt} \right) + \\ \left(\sum_{k=1}^{j} L_{CHj} \right) \left(\frac{d^2 i_{CHj}}{dt^2} + \frac{d^2 i_{COj}}{dt^2} \right) + R_{COn} \frac{di_{COn}}{dt} + L_{COn} \frac{d^2 i_{COn}}{dt^2} \end{array} \right] = 0 \tag{4.35}$$

For the breakdown channel of sections 1 to *n-1*,

$$V_{C_{CH\lambda}} + \left\{ \begin{array}{l} \sum_{j=1}^{\lambda} \left[\left(\sum_{k=1}^{j} R_{CHk} \right) \left(i_{CHj} + i_{COj} \right) + \left(\sum_{k=1}^{j} L_{CHj} \right) \frac{d}{dt} \left(i_{CHj} + i_{COj} \right) \right] + \\ \sum_{j=\lambda+1}^{n} \left[\left(\sum_{k=1}^{\lambda} R_{CHk} \right) \left(i_{CHj} + i_{COj} \right) + \left(\sum_{k=1}^{\lambda} L_{CHj} \right) \frac{d}{dt} \left(i_{CHj} + i_{COj} \right) \right] \end{array} \right\} = 0 \qquad (4.36)$$

where $\lambda = 1, 2, \ldots, n\text{-}1$.

Multiplying with $C_{CH\lambda}$, followed by differentiating with respect to time, t

$$i_{CH\lambda} + C_{CH\lambda} \left\{ \begin{array}{l} \sum_{j=1}^{\lambda} \left[\left(\sum_{k=1}^{j} R_{CHk} \right) \left(\frac{di_{CHj}}{dt} + \frac{di_{COj}}{dt} \right) + \left(\sum_{k=1}^{j} L_{CHj} \right) \left(\frac{d^2 i_{CHj}}{dt^2} + \frac{d^2 i_{COj}}{dt^2} \right) \right] + \\ \sum_{j=\lambda+1}^{n} \left[\left(\sum_{k=1}^{\lambda} R_{CHk} \right) \left(\frac{di_{CHj}}{dt} + \frac{di_{COj}}{dt} \right) + \left(\sum_{k=1}^{\lambda} L_{CHj} \right) \left(\frac{d^2 i_{CHj}}{dt^2} + \frac{d^2 i_{COj}}{dt^2} \right) \right] \end{array} \right\} = 0$$

(4.37)

For the corona sheath of sections 1 to *n-1*,

$$V_{C_{CH\lambda}} + \left\{ \begin{array}{l} \sum_{j=1}^{\lambda} \left[\left(\sum_{k=1}^{j} R_{CHk} \right) \left(i_{CHj} + i_{COj} \right) + \left(\sum_{k=1}^{j} L_{CHj} \right) \frac{d}{dt} \left(i_{CHj} + i_{COj} \right) \right] + \\ \sum_{j=\lambda+1}^{n} \left[\left(\sum_{k=1}^{\lambda} R_{CHk} \right) \left(i_{CHj} + i_{COj} \right) + \left(\sum_{k=1}^{\lambda} L_{CHj} \right) \frac{d}{dt} \left(i_{CHj} + i_{COj} \right) \right] \end{array} \right\} = 0 \qquad (4.38)$$

where $\lambda = 1, 2, \ldots, n\text{-}1$.

Multiplying with $C_{CO\lambda}$, followed by differentiating with respect to time, t

$$i_{CO\lambda} + C_{CO\lambda} \left\{ \begin{array}{l} \sum_{j=1}^{\lambda} \left[\left(\sum_{k=1}^{j} R_{CHk} \right) \left(\frac{di_{CHj}}{dt} + \frac{di_{COj}}{dt} \right) + \left(\sum_{k=1}^{j} L_{CHj} \right) \left(\frac{d^2 i_{CHj}}{dt^2} + \frac{d^2 i_{COj}}{dt^2} \right) \right] + \\ \sum_{j=\lambda+1}^{n} \left[\left(\sum_{k=1}^{\lambda} R_{CHk} \right) \left(\frac{di_{CHj}}{dt} + \frac{di_{COj}}{dt} \right) + \left(\sum_{k=1}^{\lambda} L_{CHj} \right) \left(\frac{d^2 i_{CHj}}{dt^2} + \frac{d^2 i_{COj}}{dt^2} \right) \right] + \\ R_{CO\lambda} \frac{di_{CO\lambda}}{dt} + L_{CO\lambda} \frac{d^2 i_{CO\lambda}}{dt^2} \end{array} \right\} = 0$$

(4.39)

As before, the voltage equations (4.32), (4.34), (4.36) and (4.38)can be rewritten in matrix form,

$$[\mathbf{V_n}]+[\mathbf{R_n}][\mathbf{i_n}]+[\mathbf{L_n}]\left[\frac{\mathbf{di_n}}{\mathbf{dt}}\right]=0 \tag{4.40}$$

And equations (4.33), (4.35), (4.37) and (4.39) can be expressed in matrix form as

$$[\mathbf{C_n}][\mathbf{i_n}]+[\mathbf{R_n}]\left[\frac{\mathbf{di_n}}{\mathbf{dt}}\right]+[\mathbf{L_n}]\left[\frac{\mathbf{d^2i_n}}{\mathbf{dt^2}}\right]=0 \tag{4.41}$$

The initial conditions at $t = t_n$ are

$$\begin{bmatrix} i_{CHn} \\ i_{COn} \\ V_{C_{CHn}} \\ V_{C_{COn}} \end{bmatrix} = \begin{bmatrix} 0 \\ 0 \\ U_{CHn} \\ U_{COn} \end{bmatrix} \tag{4.42}$$

and

$$\begin{bmatrix} i_{CH\lambda} \\ i_{CO\lambda} \\ V_{C_{CH\lambda}} \\ V_{C_{CH\lambda}} \end{bmatrix} = \begin{bmatrix} i_{CH\lambda}(t_n) \\ i_{CO\lambda}(t_n) \\ V_{CH\lambda}(t_n) \\ V_{CO\lambda}(t_n) \end{bmatrix} \tag{4.43}$$

for $\lambda = 1, 2, \ldots, n\text{-}1$.

The voltages at $t = t_n$ are obtained from the voltage matrix equation of the previous section,

$$[\mathbf{V_{n-1}}(t_n)]=-[\mathbf{R_{n-1}}][\mathbf{i_{n-1}}(t_n)]-[\mathbf{L_{n-1}}]\left[\frac{\mathbf{di_{n-1}}(t_n)}{\mathbf{dt}}\right] \tag{4.44}$$

Substituting the initial conditions for the voltages into equation (4.40),

$$\begin{bmatrix} \mathbf{V_{n-1}}(t_n) \\ \hline U_{CHn} \\ U_{COn} \end{bmatrix} + [\mathbf{R_n}][\mathbf{i_n}(t_n)] + [\mathbf{L_n}]\left[\frac{\mathbf{di_n}(t_n)}{\mathbf{dt}}\right] = 0 \tag{4.45}$$

Therefore, the initial conditions are

$$\left[\frac{\mathbf{di_n}(t_n)}{\mathbf{dt}}\right] = -[\mathbf{L_n}]^{-1}\begin{bmatrix} \mathbf{V_{n-1}}(t_n) \\ \hline U_{CHn} \\ U_{COn} \end{bmatrix} - [\mathbf{L_n}]^{-1}[\mathbf{R_n}][\mathbf{i_n}(t_n)] + \tag{4.46}$$

and

$$[\mathbf{i_n}(t_n)] = \begin{bmatrix} \mathbf{i_{n-1}}(t_n) \\ \hline 0 \\ 0 \end{bmatrix} \tag{4.47}$$

A computer program code was written in MATLAB, which employs the Runge-Kutta formulae, to solve the above differential equations. The validity of the program code was verified against analytical solutions.

The total return stroke current at ground is given by

$$i(0,t) = \begin{cases} \sum_{k=1}^{m}\left[\sum_{n=1}^{k}\left(i_{CHn} + i_{COn}\right)\right]\left[u(t-kw) - u(t-(k+1)w)\right] & t \geq w \\ 0 & t < w \end{cases} \tag{4.48}$$

where $u(t)$ is the Heaviside step function defined as

$$u(t) = \begin{cases} 1 & t \geq 0 \\ 0 & t < 0 \end{cases} \tag{4.49}$$

4.2.3 Profile of Circuit Elements

The potential of the base of a thundercloud reaches a magnitude of 10 to 100 MV [9]. Selecting the value of 100 MV, the potential distribution of the lightning channel was set to be linear. Assuming the potential of the breakdown channel and corona sheath capacitances to be the same prior to the attachment process, the initial voltages of the capacitances are given by

$$U_{CHn} = U_{COn} = \frac{n}{m} \times 100 \ MV \tag{4.50}$$

While the total charge lowered can be set to the recorded values as presented by Berger *et al*., the actual ratio of charges lowered by the breakdown channel current and the corona sheath current is not known. Thus, the current distribution found by the DU model was adopted. The current equations were integrated and it was found that the breakdown channel current lowers 15.5% of the total charge and the corona sheath current lowers 84.5%.

As with the charge distribution, the capacitance values were set to be exponentially decreasing with height.

$$C_n = k_C \exp\left(-\alpha n\right) \tag{4.51}$$

And by equating the total charges in the capacitors with the median charge lowered, the capacitance values can be determined.

$$\sum C_n V_n = Q \tag{4.52}$$

For convenience, the constant k_C was set to m/n so that the exponent for the capacitors can be found easily.

C. A. Jordan [40] had defined the external inductance of a current-carrying vertical cylinder with consideration given to its image below the true ground plane. The elementary inductance of an element *dy* of a tower equivalent cylinder, at an elevation *y* above the true ground plane was given as

$$dL = \left[\ln \frac{\sqrt{(h+a-y)^2 + r^2} + (h+a-y)}{\sqrt{(h+a+y)^2 + r^2} + (h+a+y)} + \ln \frac{\sqrt{(a+y)^2 + r^2} + (a+y)}{\sqrt{(a-y)^2 + r^2} + (a-y)} \right] dy \quad (4.53)$$

where *h* is the height of cylinder above ground plane, *r* is the radius of cylinder, and *a* is the depth of true ground plane below earth's surface.

Equation (4.53) was adopted to describe the inductance of the proposed circuit with *h* as the height of the lightning channel, *r* set to 5 cm [1] and *a* assumed to be zero. The individual breakdown channel inductances were found by integrating equation (4.53) between the height limits of each section while the corona sheath inductances were simply set to be a multiple of the breakdown channel inductances. While it can be considered reasonable to assume the radius of the lightning channel to be uniform, the main discrepancy in applying equation (4.53) lies in that it was defined for the current in the cylinder being uniform throughout its length. Hence, the inductance distribution was taken as a multiple of the integral of equation (4.53) rather than strictly adhering to it. This also allows additional freedom in tuning the parameters when fitting the return stroke current waveform.

It can be clearly seen from the circuit that most of the current flowing through each section decreases with height. And since the resistance of an arc is inversely related to its current, the resistances in the circuit were set to be exponentially proportional to height.

$$R_n = k_R \exp(\beta n) \tag{4.54}$$

4.3 EVALUATION OF PROPOSED MODEL

The intention was to produce a set of lightning return stroke current waveforms at ground that matched the lightning parameters measured by *Berger et al.* (Table 2.1). The model was fitted to match the 5th percentile, median and 95th percentile values, henceforth also termed as the 14 kA, 30 kA and 80 kA strokes (after their peak current values) respectively. While it was noted that the median (or the other two percentiles) values put together do not necessarily represent a median lightning return stroke current, all the values of each percentile were lumped together for the description of each characteristic stroke. This postulation was required for the legitimate comparison of the results obtained.

Numerous lightning return stroke current waveshapes have been presented based on current oscillograms readings. But such actual recordings are incapable of showing the composition of the current as a result of its two components. The widely recognised DU model was the first to enumerate the two components to simulate the channel current. But it was noted that its waveshape (Figure 3.3) and current parameters were for an arbitrary lightning stroke rather than the desired lightning current. Therefore its waveshape was chosen only as a guide for the proposed model, while simultaneously matching Berger *et al*.'s measured values.

The simulation was conducted for the proposed model with 10 sections. The resulting waveforms [1] for the 3 currents are presented together in Figure 4.2 and the corresponding lightning current parameters are shown in Table 4.2. The values found by *Berger et al.* are listed together for easy comparison. Figures 4.3 – 4.5 show the individual currents with their respective breakdown channel and corona sheath components. The corresponding circuit element values are shown in Tables 4.3 – 4.5 respectively.

The current waveforms are similar to the double exponential waveshape described by the DU model. The main difference lies in the breakdown channel currents. But the fact that it fails to decay to zero rapidly, as opposed to the DU model, is clearly a consequence of the inductive presence in the channel. Moreover, it also maintains that the channel is still 'hot' and conducive for current sustenance.

[1] The polarity of the currents are reversed with respect to that as indicated in the circuit (Figure 4.1) for easy viewing and comparison.

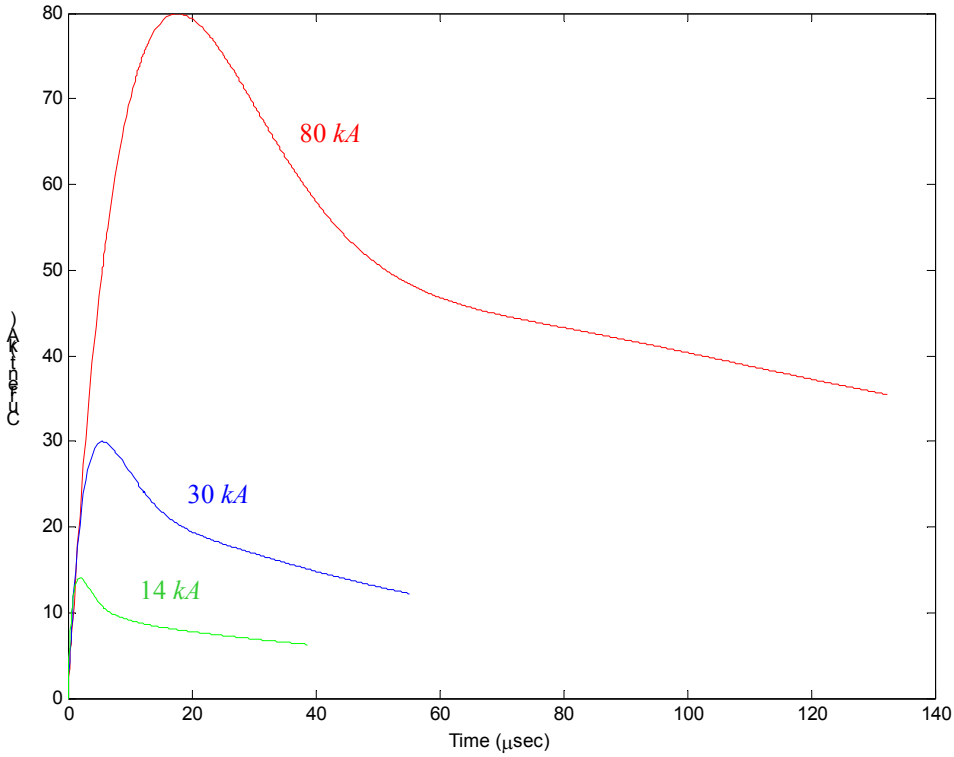

Figure 4.2 Lightning return stroke currents in proposed model

The proposed model was shown to be capable of matching the median peak current, charge lowered and front duration accurately. The maximum *di/dt* could not be matched except for the 30 kA stroke where a slight difference was observed. This was attributed to coincidence as the general trend of the maximum *di/dt* recorded was inverse to that measured by Berger *et al*. This discrepancy is due to the way the circuit elements were defined, leading to the nature of the waveforms. Measured lightning return stroke waveforms exhibit a slow initial rate of rise followed by an increased *di/dt* on its wavefront similar to that displayed by the corona sheath current. Whereas in the waveforms produced by the proposed model, the maximum *di/dt* always occurs at $t = 0$. Hence even if the values of the maximum *di/dt* could be matched, it would have been inconsequential.

Another discrepancy observed was in the stroke duration, though the value was comparable for the 14 kA stroke. The inability to fit the stroke duration is also due to the nature of the circuit. Basically, the stroke duration could be lengthened by increasing the inductance. But since the circuit is essentially second-order in nature, oscillations were observed when higher values of inductances were applied. Furthermore, additional effects of increasing the inductance are the delay of the front duration and the lowering of the peak current. Hence it was elected to maintain the front duration and peak current as it is usually the wavefront that the damaging effects of lightning are attributed to.

The total charge lowered was matched exactly because of the way the capacitances were defined. Basically the capacitances were set based on the values measured by Berger *et al*. While this choice of action reduced the degree of freedom available in tuning the circuit, the additional degree of freedom would have made the tuning process increasingly tedious.

In addition, the radius of the lightning channel was fixed at a constant value while omitting the effects of channel expansion, which is usually observed during the initial 10 μs or so. Such a change has an immediate effect on the resistance and inductance of the lightning channel. But since the initial radius as well as its rate of change is not known, the effects of varying inductance and resistance were ignored in the proposed model.

Table 4.2 Lightning Current Parameters of Proposed Model vs. Berger *et al.*'s Measured Values

Parameters	Unit	95 %		50 %		5 %	
		Proposed model	Berger *et al.*'s value	Proposed model	Berger *et al.*'s value	Proposed model	Berger *et al.*'s value
Peak current (minimum 2 kA)	kA	14.09	14	29.97	30	79.92	80
Charge	C	1.1	1.1	5.2	5.2	24	24
Front duration (2 kA to peak)	μs	1.79	1.8	5.46	5.5	17.57	18
Maximum *di*/*dt*	kA/μs	25.55	5.5	15.06	12	12.25	32
Stroke duration (2 kA to half-value)	μs	28.43	30	39.19	75	102.57	200

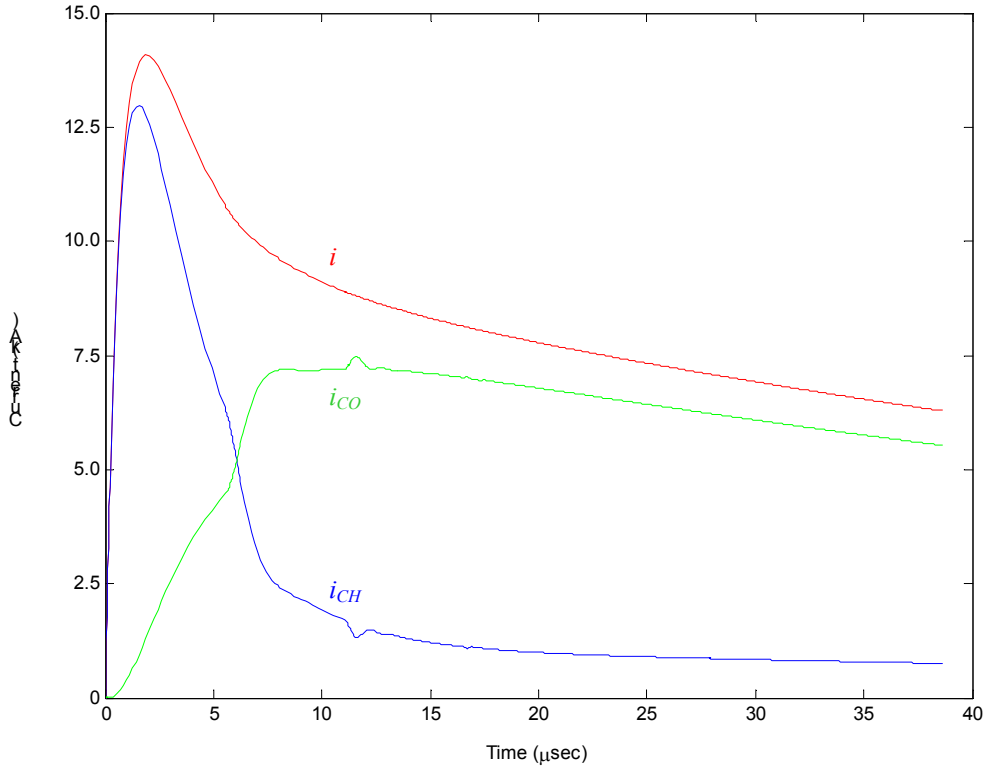

Figure 4.3 14 kA return stroke current

Table 4.1 Circuit Element Values for 14 kA Return Stroke Current

	Breakdown Channel	Corona Sheath
Charge (total: 1.1C)	0.1706 C	0.9294 C
Capacitance	$\frac{m}{n}\times\exp\left(\frac{-n}{0.5192}\right)\times10^{-8}$ F	$\frac{m}{n}\times\exp\left(\frac{-n}{1.3697}\right)\times10^{-8}$ F
Resistance	$0.7\times\exp\left(\frac{n}{0.46}\right)\times10^{2}$ Ω	$6.8\times\exp\left(\frac{n}{13.0}\right)\times10^{2}$ Ω
Inductance	$0.41\times\int dL$ H	$0.31\times\int dL$ H

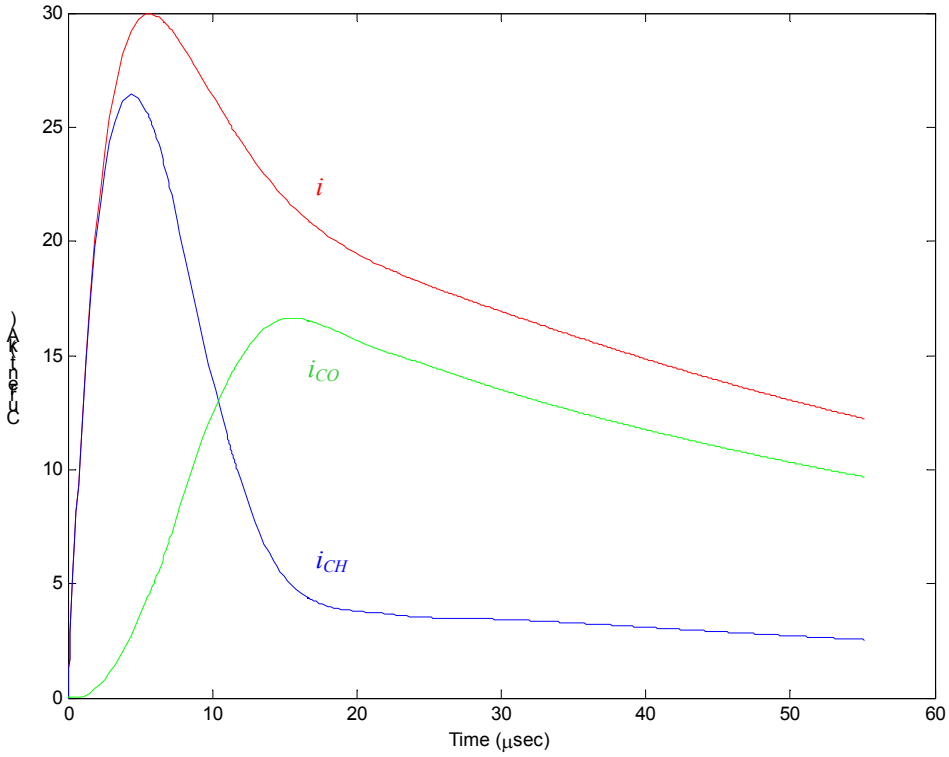

Figure 4.4 30 kA return stroke current

Table 4.2 Circuit Element Values for 30 kA Return Stroke Current

	Breakdown Channel	Corona Sheath
Charge (total: 5.2 C)	0.8064 C	4.3936 C
Capacitance	$\frac{m}{n}\times\exp\left(\frac{-n}{1.24}\right)\times10^{-8}$ F	$\frac{m}{n}\times\exp\left(\frac{-n}{5.85}\right)\times10^{-8}$ F
Resistance	$0.27\times\exp\left(\frac{n}{0.45}\right)\times10^{2}$ Ω	$3.0\times\exp\left(\frac{n}{11.0}\right)\times10^{2}$ Ω
Inductance	$0.75\times\int dL$ H	$\int dL$ H

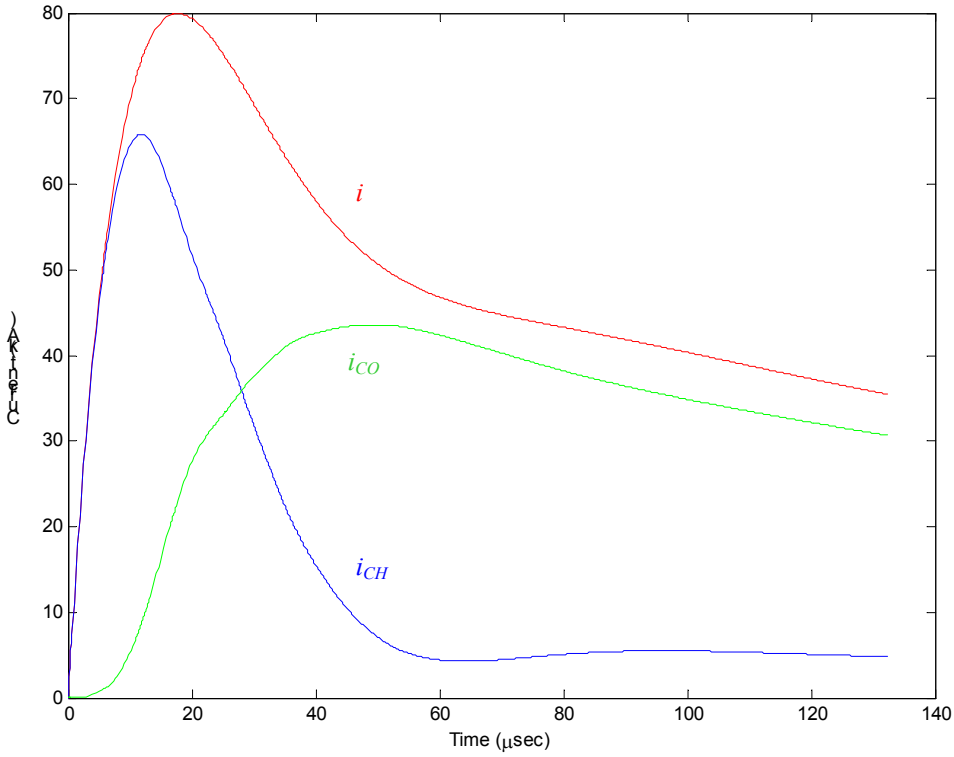

Figure 4.5 80 kA return stroke current

Table 4.3 Circuit Element Values for 80 kA Return Stroke Current

	Breakdown Channel	Corona Sheath
Charge (total: 24 C)	3.7219 C	20.2781 C
Capacitance	$\frac{m}{n}\times\exp\left(\frac{-n}{0.7664}\right)\times10^{-7}$ F	$\frac{m}{n}\times\exp\left(\frac{-n}{2.5351}\right)\times10^{-7}$ F
Resistance	$0.12\times\exp\left(\frac{n}{0.50}\right)\times10^{2}$ Ω	$1.6\times\exp\left(\frac{n}{15.0}\right)\times10^{2}$ Ω
Inductance	$\int dL$ H	$1.2\times\int dL$ H

CHAPTER 5

APPLICATION OF DISTRIBUTED CIRCUIT MODEL ON SEMICONDUCTOR LIGHTNING EXTENDER

The traditional Franklin rod remains widely used today for protection against lightning. Its function is mainly to prevent direct strikes on man and property by drawing the lightning stroke and directing it to ground via a low resistance path. But it is incapable of alleviating the direct and induced effects of the large lightning current. On the other hand, the revolutionary Semiconductor Lightning Extender (SLE) uses high resistance rods which can effectively reduce the magnitude of the lightning current. This novel lightning protection system has grown in popularity and is presently used in many countries including China, Singapore, Malaysia, Japan, Iran and USA.

5.1 SEMICONDUCTOR LIGHTNING EXTENDER (SLE)

5.1.1 Physical Structure

The SLE comprises of 3 to 25 semiconductor rods distributed radially from a centre base plate to form 2 to 3 fan-shaped surfaces. Figure 5.1 shows a 3-rod SLE on a base plate which can hold up to 13 rods. Each rod is 5 m in length with 4 metal needles protruding from the tip of each rod as shown in Figure 5.2. The angle between two adjacent rods on each fan-shaped surface is between 20 to 25 degrees [4].

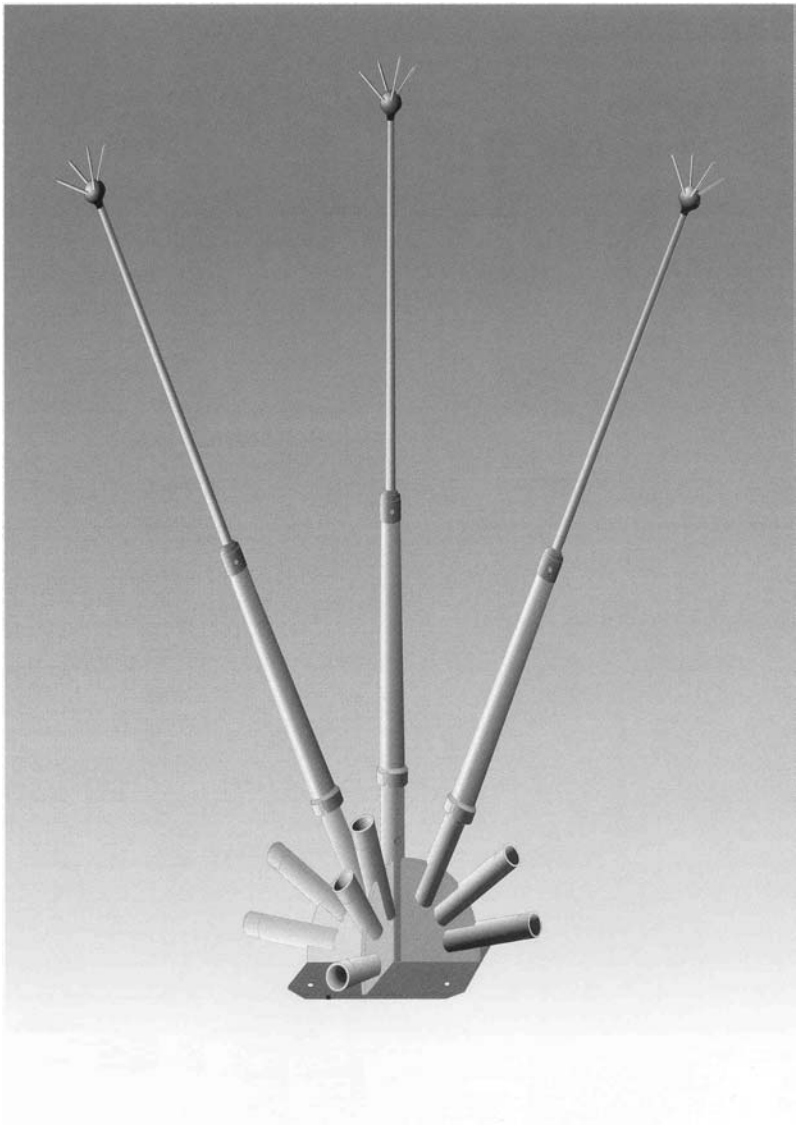

Figure 5.1 3-rod SLE

Figure 5.2 Single SLE rod with 4 needles

5.1.2 Characteristics

Each rod is made of silicon rubber, epoxy resins and semiconductor materials and has a resistance of 35 kΩ [5]. With such a large resistance, the lightning discharge current can naturally be reduced as understood from Ohm's Law. But simultaneously, this large resistance causes the voltage across the semiconductor rod to increase significantly. This poses a risk of flashover along the rod, thereby removing the current-limiting effect of the high resistance rod. This is precisely why the SLE is composed of a number of rods rather than just one. The angle between adjacent rods has been calculated to favour the occurrence of flashover to another rod rather than along the rod itself. Each flashover event is equivalent to the addition of another semiconductor rod in parallel. The unique structure of the SLE enables current sharing between rods, thereby allowing the handling of larger current strokes. The current limiting effect is hence maintained, effectively reducing the lightning discharge current from 100 % to 0.4 % [4]. Simultaneously, the SLE can prolong the lightning discharge

current duration and decrease the rate of rise of current, *di*/*dt*, thereby reducing its potentially damaging effects.

The sharp needles of the SLE can produce 3 – 14.5 mA neutralising currents under the thundercloud. When the thundercloud is heavily charged, 1 – 2 m long spark discharge can occur at the top of the semiconductor rods with neutralising currents reaching magnitudes of 1 kA and above. With this function, the SLE can reduce the probability of lightning occurrence by 25 % [4].

The SLE can also completely eliminate the occurrence of upward lightning strokes which constitute more than 50 % of all lightning strokes on high buildings or towers. The high resistance rods limit the current in the upward leader, thus restricting the formation of the lightning channel.

The protective angle of the SLE can reach up to 80 degrees due to its fan-shaped arrangement, protecting a larger zone compared to the 45 degrees or less for conventional lightning rods.

5.1.3 Field Measurement Results on SLE

Measured lightning current data for direct lightning strikes on the SLE presented by Xie *et al*. are reproduced in Table 5.1 [4, 5]. Three types of equipment were employed in the measurement of the direct lightning current: 1) the automatic lightning current measurement device YL0-1 in the range of 10 – 100 kA, 2) the ferromagnetic bar, and 3) the thermal crack on the protective lacquer membrane which can indicate the passing of a current of 10 – 35 A through the semiconductor rod in the millisecond

range. Of the 38 measurements, 6 were dual strokes and 2 were triple strokes. The last 5 measurements (No. 34 – 38) were measured using the thermal crack, hence the polarity was unclear. Table 5.2 shows the cumulative probability distribution of the measurements for currents (absolute value) larger than *I*.

The results clearly reflect the SLE's ability to reduce the lightning discharge current.

Table 5.1 Lightning Current Measured by Xie *et al.*

No.	1	2	3	4	5	6	7
I (A)	-485	-26	-296	-362	-43	-346	-233
No.	8	9	10	11	12	13	14
I (A)	-335	-79	-485	-391	-28	-368	-346
No.	15	16	17	18	19	20	21
I (A)	-356	-204	-391	-348	-143	-403	+67
No.	22	23	24	25	26	27	28
I (A)	-303	+47	+278	-327	-628	-290	-991
No.	29	30	31	32	33	34	35
I (A)	-100	-100	-200	-100	+200	300	30
No.	36	37	38				
I (A)	210	240	200				

Note: No. 4 – 5, No. 6 – 7, No. 8 – 9, No. 11 – 12, No. 18 – 19 and No. 20 – 21 are dual strokes, and No. 14 – 16 and No. 22 – 24 are triple strokes

Table 5.2 Cumulative Probability Distribution of Currents Larger Than I

I (A)	30	50	100	200	300
P (%)	92.1	86.8	73.7	63.2	42.1
I (A)	400	500	700	1000	
P (%)	13.2	5.3	2.6	0	

5.2 MODELLING OF THE SLE

5.2.1 Circuit Representation

A circuit representation of the SLE was required for the application of the proposed model. In view of the behaviour of the SLE on incident lightning strikes, it was simply modelled as a variable resistor and its resistance R_{SLE} is given as

$$R_{SLE} = \frac{35\text{k}\Omega}{n_{rods}} \tag{5.55}$$

where n_{rods} is the number of semiconductor rods in parallel.

As such, the initial value of n_{rods} is 1 when lightning strikes directly on the SLE. As the current and voltage V_{SLE} at the tip of the semiconductor rod rises, flashover occurs when the voltage reaches the flashover value V_{flash}. On such an event and subsequent flashovers, the value of n_{rods} is incremented by 1.

With a reduction in the lightning discharge current, the lightning channel is weakened. Neutralisation of the channel is not as intense and so the resistance of the lightning channel maintains a high value. Corresponding adjustments were made to the circuit model through the addition of weakening resistances in the breakdown channel

$R_{CH,weak}$ and corona sheath $R_{CO,weak}$. Figure 5.3 shows the lightning channel model with the inclusion of the SLE and weakening resistances.

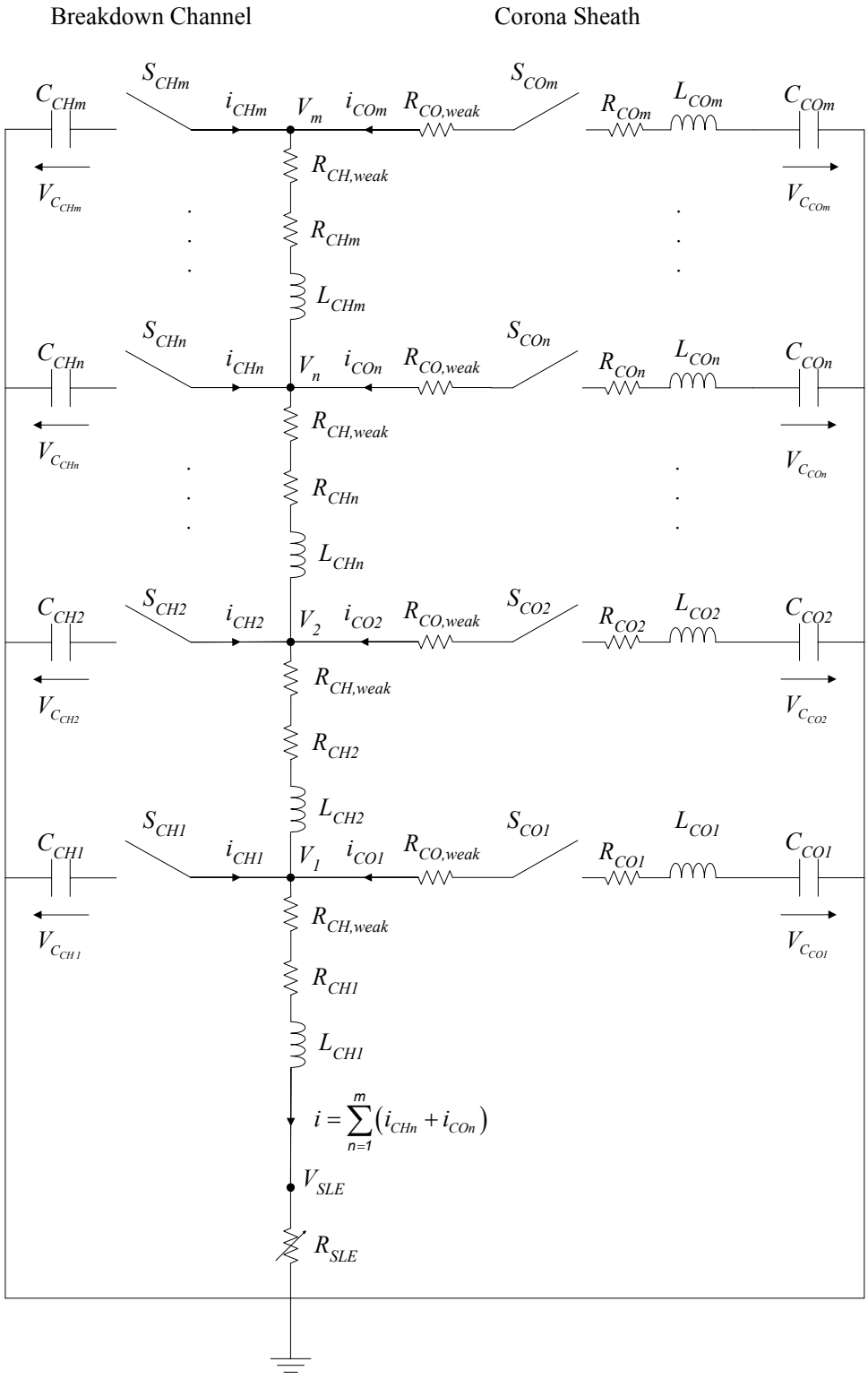

Figure 5.3 Equivalent circuit of lightning channel with inclusion of SLE

5.2.2 Flashover Voltage

The flashover voltage was derived through the impulse flashover characteristics of standard rod gaps [41]. For an angular spacing between adjacent 5-m rods of between 20 to 25 degrees, the separation distance of the tip of the rods is between 1.736 m to 2.164 m respectively. For convenience, the separation distance was taken to be 2 m (approximately 80 inches). The corresponding volt-time curve was found and is shown in Figure 5.4.

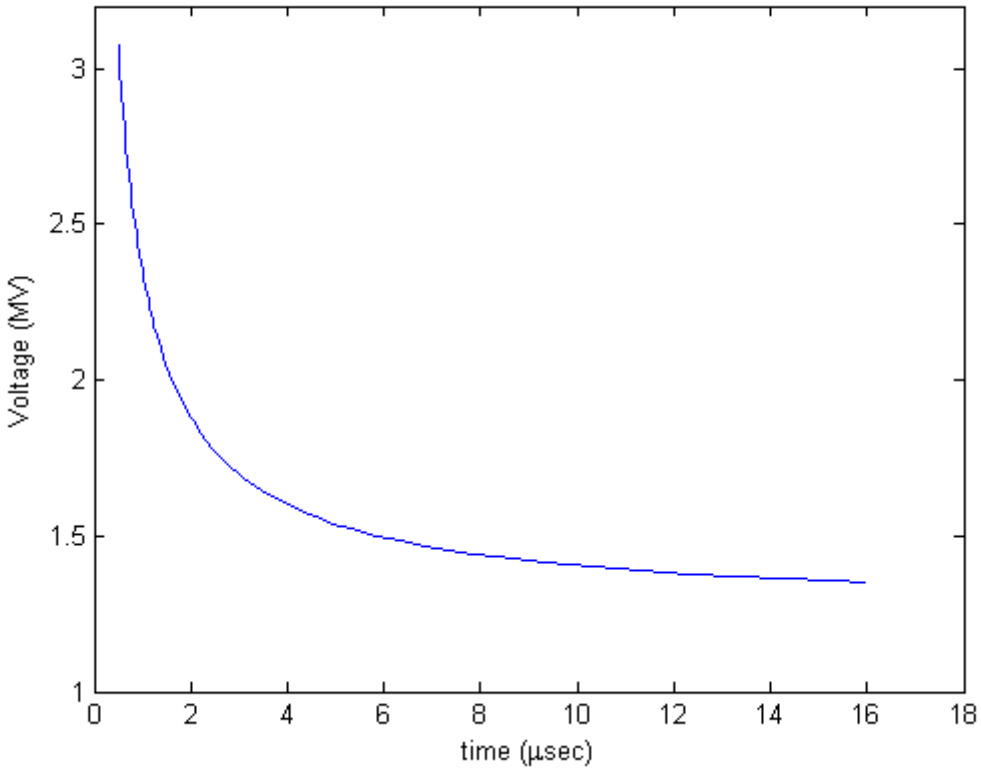

Figure 5.4 Volt-time curve for 2-m rod gap

5.3 RESULTS AND EVALUATION

The study was initially conducted for the median 30 kA lightning return stroke current. The weakening resistances were set to 500 Ω/m as suggested by Xie *et al.* in [4, 5]. For the channel height of 5 km and the number of sections being 10, the height of each

section is 500 m. The weakening resistance added to each section was therefore 250 kΩ. As there are two weakening resistors in each section, the weakening resistance was divided equally among the resistors. Therefore

$$R_{CH,weak} = R_{CO,weak} = 125\text{k}\Omega \tag{5.56}$$

The waveforms of the voltage across the SLE and the current at the base of the lightning channel are presented in Figure 5.5. The volt-time curve is included to indicate the instant of flashover which occurred once. The current was reduced from 30 kA to 62.4 A, which is a reduction to 0.208 %. The response is heavily damped which is consistent with the understanding from the case of adding a large resistance to an *R-L-C* circuit.

The study was then extended to the 14 kA and 80 kA strokes. Corresponding modifications to the weakening resistances were required but there is no other such value available. So by comparing the breakdown channel and corona sheath resistances for the 14 kA stroke with the 30 kA stroke, it was noted that the resistances for the former was approximately double. Hence the weakening resistances were doubled for this case, i.e. 250 kΩ. Similarly the weakening resistances for the 80 kA stroke were halved to 62.5 kΩ. Figures 5.6 and 5.7 show the resulting waveforms. There was no events of flashover for the 14 kA stroke and the current was reduced to 35 A, which is a 0.25 % reduction. For the 80 kA stroke, the flashover occurred 3 times and the peak current was reduced to 140 *A*, a 0.175 % reduction. And as with the 30 kA case, the waveforms obtained were heavily damped.

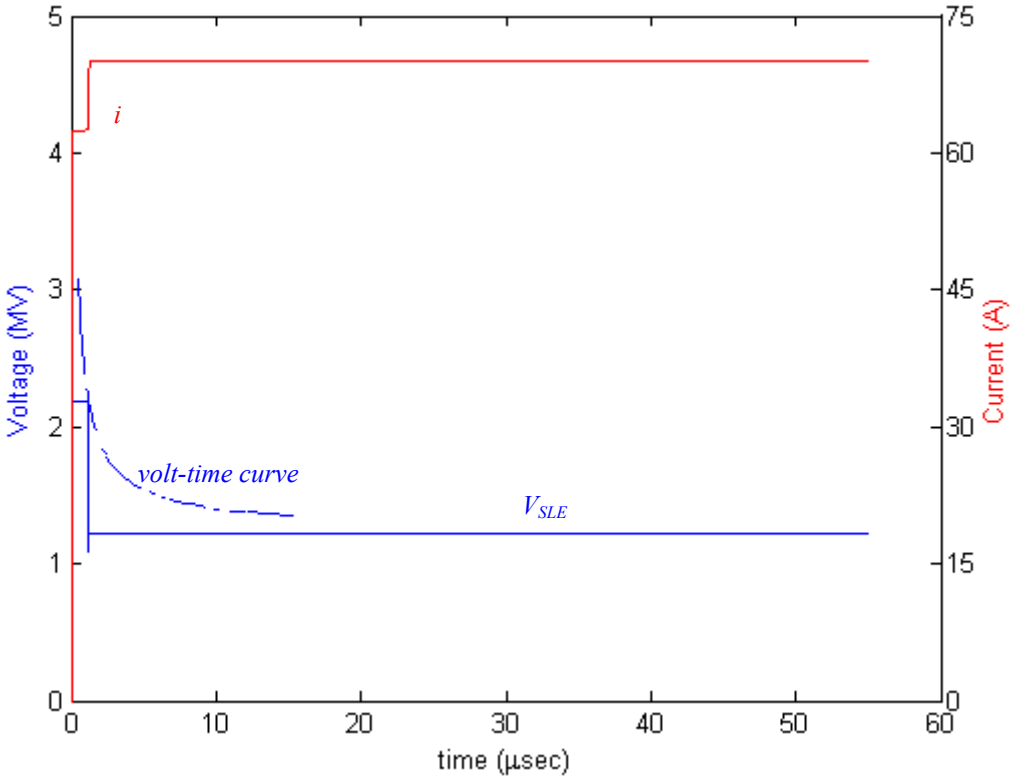

(a) 0 – 60 μs

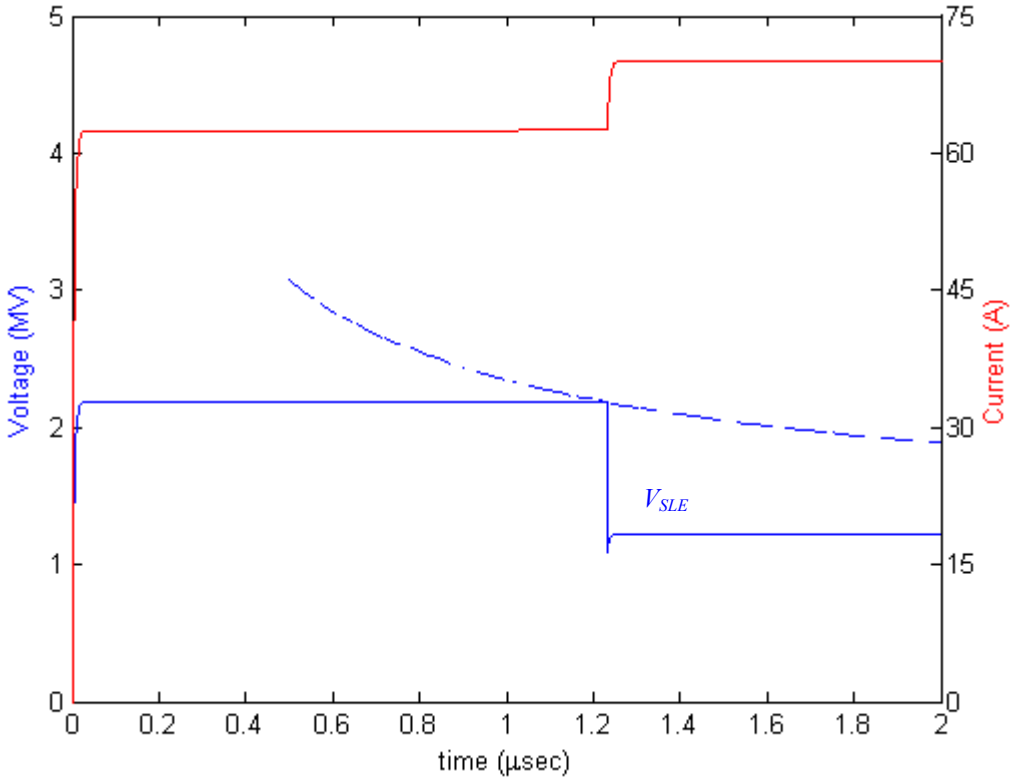

(b) 0 – 2 μs

Figure 5.5 Voltage and current through SLE for 30 kA stroke

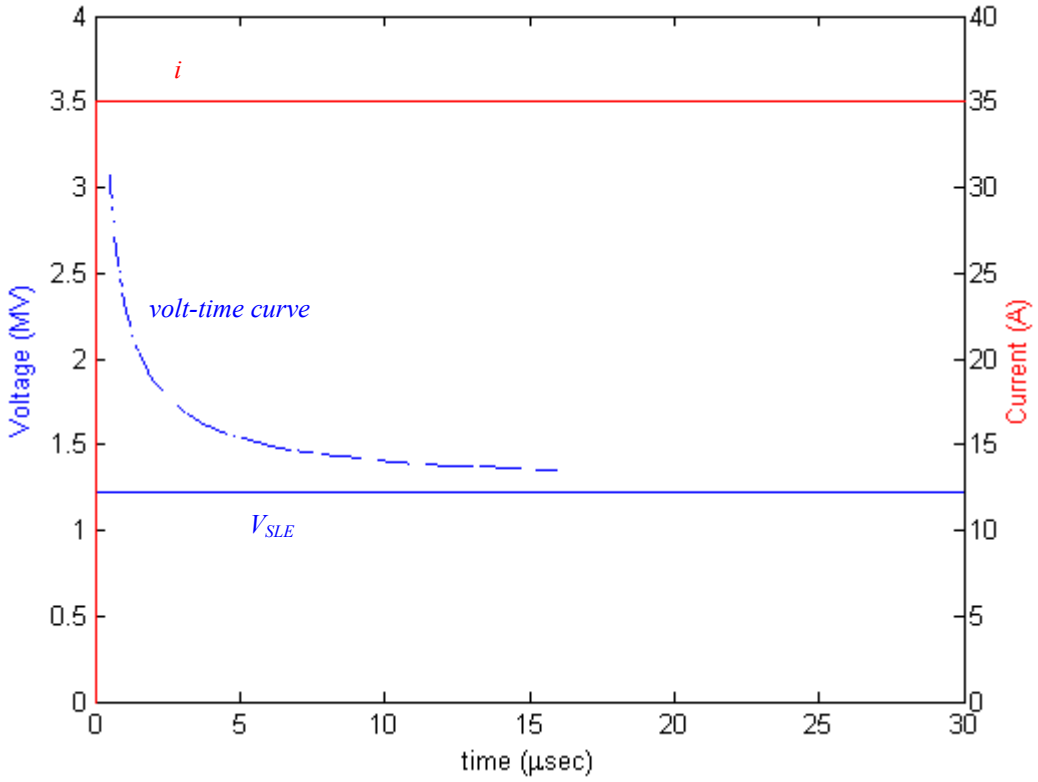

(a) 0 – 30 μs

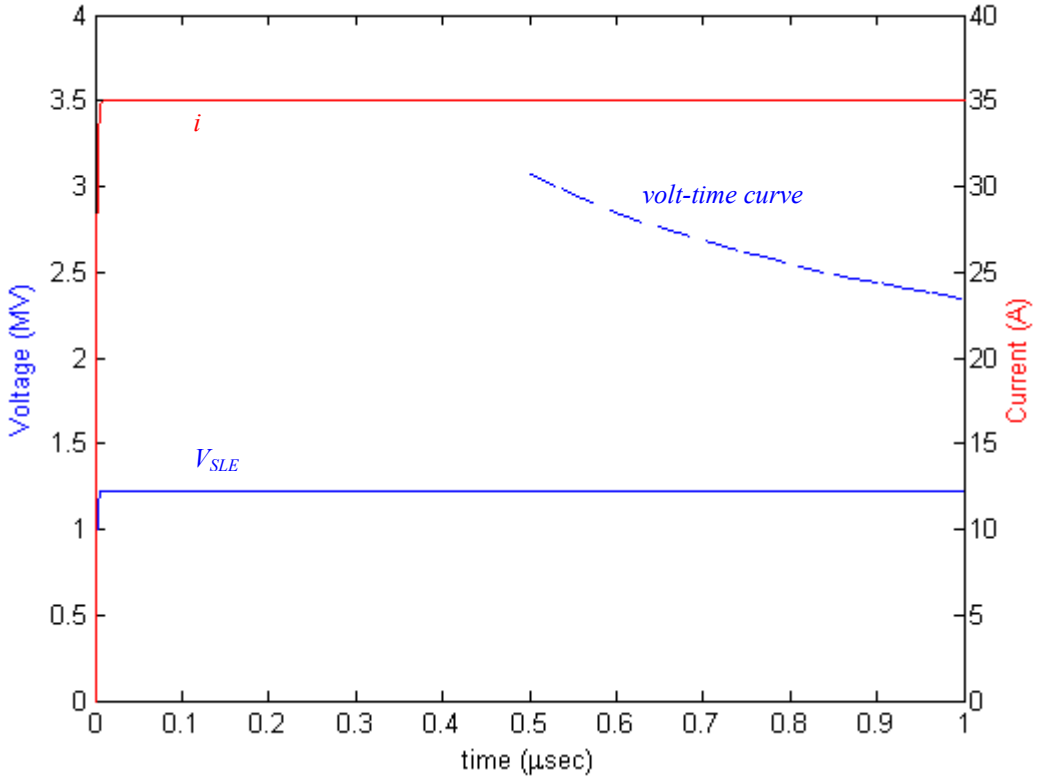

(b) 0 – 1 μs

Figure 5.6 Voltage and current through SLE for 14 kA stroke

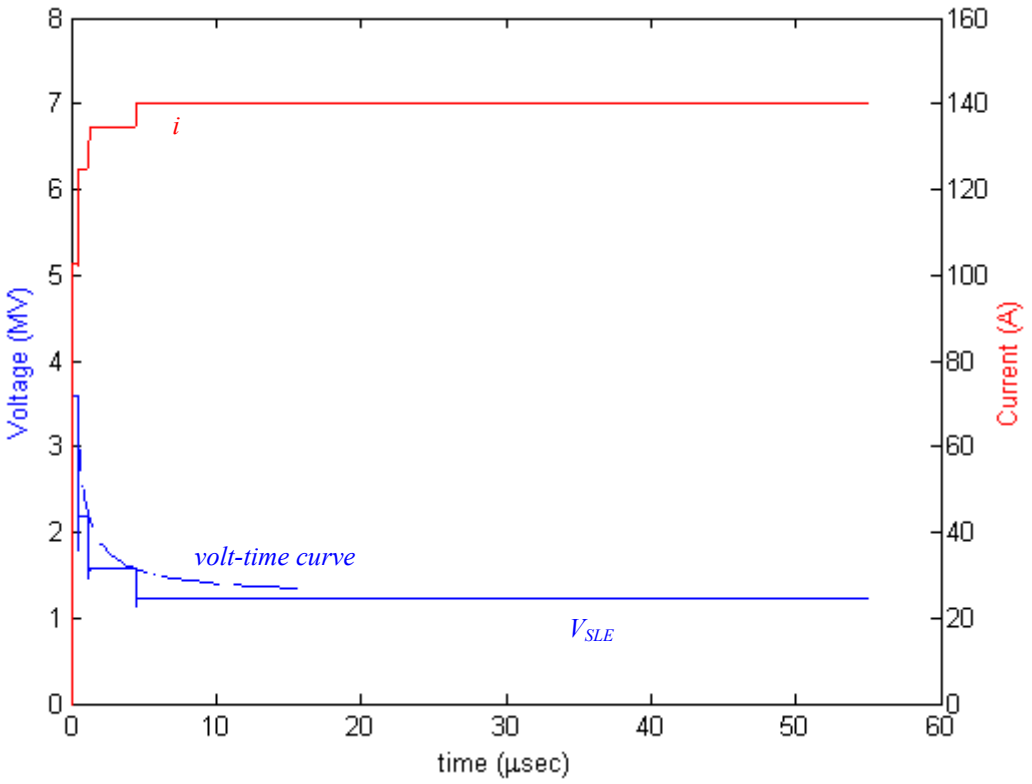

(a) 0 – 60 μs

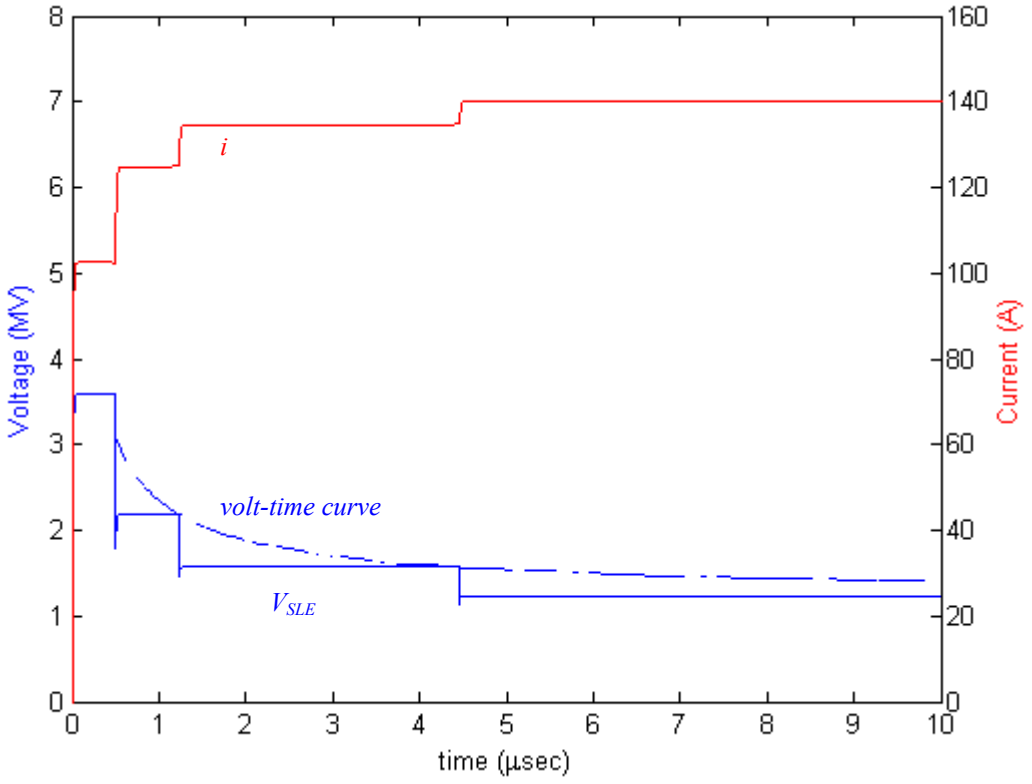

(b) 0 – 10 μs

Figure 5.7 Voltage and current through SLE for 80 kA stroke

The current reduction percentages obtained for the proposed model are close to the 0.4 % suggested by Xie *et al.* [4], even though the probabilities of occurrence of the 3 strokes and their corresponding reduced currents do not match the probabilities compiled through direct measurement shown in Table 5.2. The main cause was attributed to the assumed values for the weakening resistances. The value of 500 Ω/m and the subsequent adjustments are only approximate values employed for use with the proposed model. But in all, the proposed model performed reasonably well in this study, demonstrating the SLE's ability to significantly reduce the lightning discharge current.

Although the proposed model was incapable of matching the maximum *di/dt* as presented in Chapter 4, a close look at the initial sub-microsecond behaviour of the currents through the SLE exhibit a slower rate of rise. The current waveforms with and without the inclusion of the SLE are presented together in Figure 5.8 for all 3 currents.

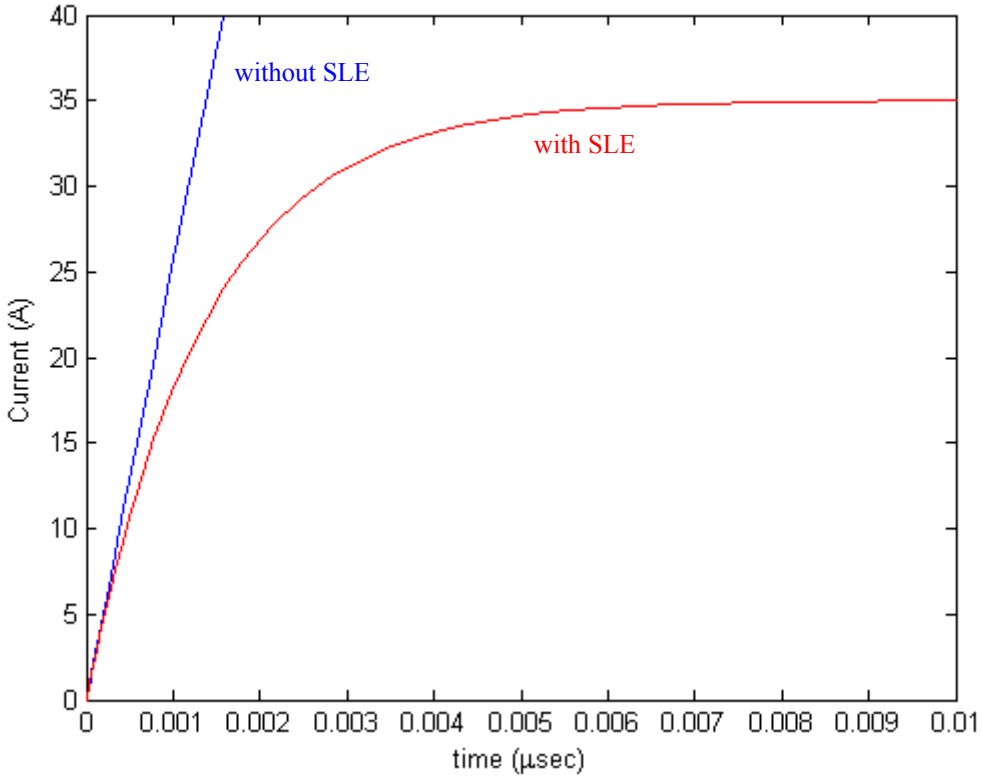

(a) 14 kA stroke

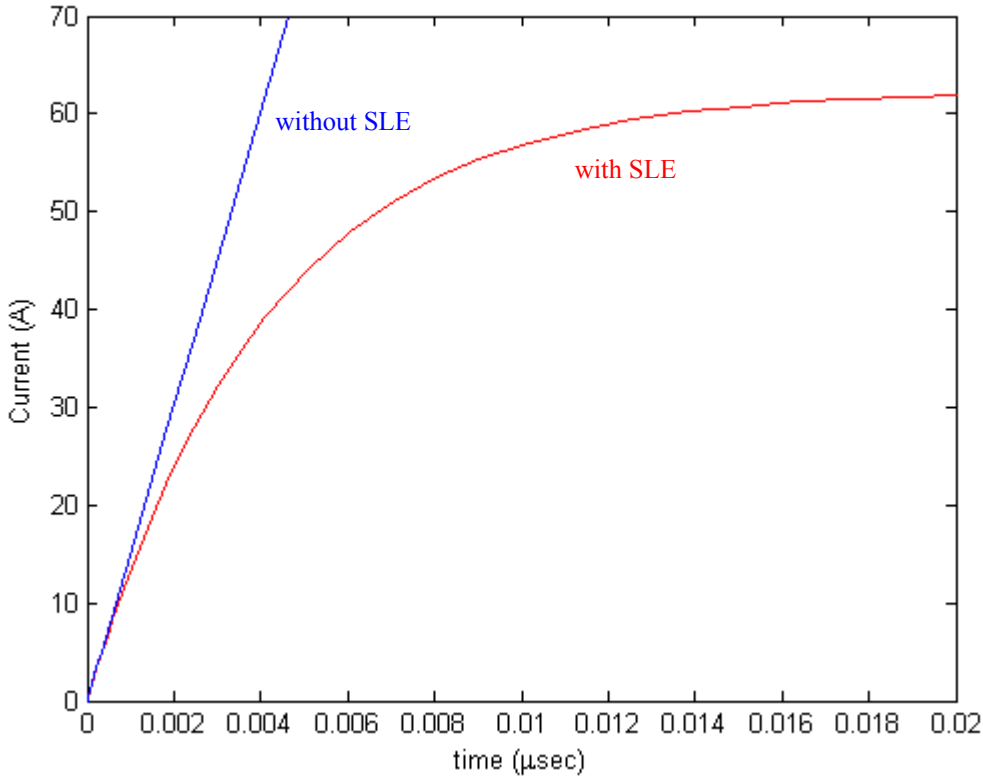

(b) 30 kA stroke

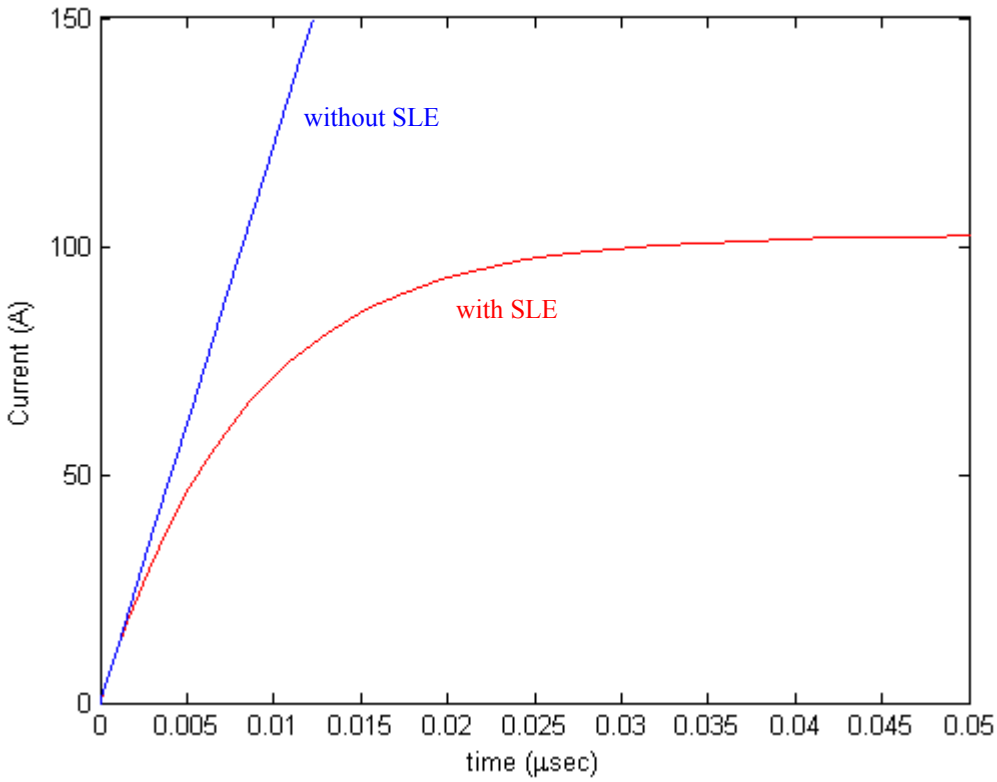

(c) 80 kA stroke

Figure 5.8 Comparison of currents with and without SLE

The proposed model has shown to be capable of demonstrating the current-limiting characteristic of the SLE. The waveforms also illustrate the behaviour of the current and voltage through the SLE during flashover. The results obtained clearly verify the validity of the proposed model.

CHAPTER 6

IMPROVED MODEL FOR ELECTROMAGNETIC FIELDS GENERATED BY TORTUOUS LIGHTNING CHANNELS

The Bruce-Golde (BG) model, transmission line (TL) model, Master-Uman-Lin-Standler (MULS) model, travelling source (TCS) model and Diendorfer-Uman (DU) model assume the temporal and spatial distribution of the channel current, which is used to calculate remote electromagnetic fields [26 – 30]. As with most models, these models approximated a straight vertical channel for the lightning path and have mainly been used for the evaluation of remote electromagnetic fields at ground. It is a known fact that the lightning channel is tortuous in nature but models adopting such geometry are limited. In the model by Lupò *et al*., the tortuous channel was broken down into a series of arbitrarily oriented straight segments and treated individually. The overall effect of the tortuous channel was then found by summing up the individual components [6]. But an error was found in the formulation which is the motivation for the modification proposed although a similar approach is adopted.

6.1 MATHEMATICAL FORMULATION

6.1.1 Electromagnetic Fields due to a Straight Vertical Segment

We first consider a straight vertical segment above ground as shown in Figure 6.1.

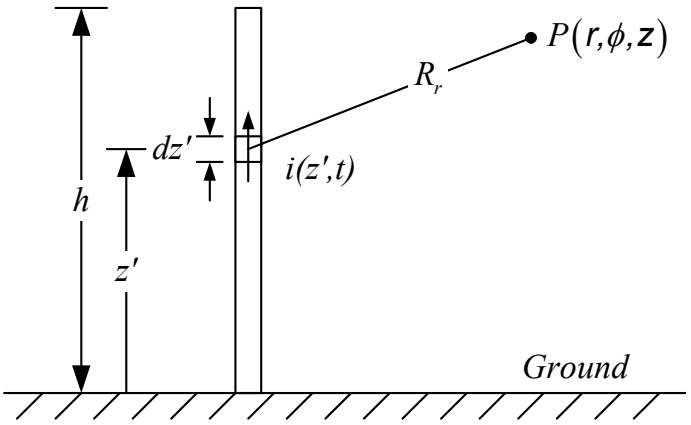

Figure 6.1 Geometry used in calculating electromagnetic fields
(Primed coordinates refer to the position along the vertical segment; unprimed coordinates refer to the observation point *P*)

Using vector magnetic potential **A** and scalar electric potential φ expressions, the electric field strength **E** and magnetic field strength **H** are given by [42]

$$\mathbf{E} = -\nabla\varphi - \frac{\partial \mathbf{A}}{\partial t} \tag{6.1}$$

$$\mathbf{H} = \frac{\nabla \times \mathbf{A}}{\mu} \tag{6.2}$$

The vector magnetic potential $d\mathbf{A}$ and scalar electric potential $d\varphi$ associated with an infinitesimal element of length dz', at $z = z'$, traversed by a current $i(z',t)$ and carrying a charge $\lambda(z',t)dz'$ are

$$d\mathbf{A} = \frac{\mu_0}{4\pi} \frac{i\left(z', t - \frac{R_r}{c}\right)}{R_r} dz' \mathbf{a}_z \tag{6.3}$$

$$d\varphi(r,\phi,z)=\frac{1}{4\pi\varepsilon_0}\frac{\lambda\left(z',t-\frac{R_r}{c}\right)}{R_r}dz' \tag{6.4}$$

where $\mathbf{a_z}$ is the unit vector along the z-axis, c is the speed of light and

$$R_r=\sqrt{(x'-x)^2+(y'-y)^2+(z'-z)^2} \tag{6.5}$$

The current profile assumed is a unit step function

$$i(z',t)=u\left(t-\frac{z'}{v}\right) \tag{6.6}$$

where v is the return stroke front speed and u is the Heaviside step function.

Applying the continuity equation

$$\nabla\cdot\mathbf{J}=-\frac{\partial\rho}{\partial t} \tag{6.7}$$

the corresponding charge distribution is

$$\begin{aligned}\lambda(z',t)&=\lambda(z',0)-\int_0^t\frac{\partial i(z',\tau)}{\partial z'}d\tau\\&=-\int_0^t\left[-\frac{1}{v}\delta\left(\tau-\frac{z'}{v}\right)\right]d\tau\\&=\frac{1}{v}u\left(t-\frac{z'}{v}\right)\end{aligned} \tag{6.8}$$

where δ is the Dirac delta function and the initial charge distribution $\lambda(z',0)$ is assumed to be zero.

Substituting equations (6.6) and (6.8) into equations (6.3) and (6.4),

$$d\mathbf{A}=\frac{\mu_0}{4\pi}\times\frac{1}{R_r}u\left(t-\frac{z'}{v}-\frac{R_r}{c}\right)dz'\mathbf{a_z} \tag{6.9}$$

$$d\varphi(r,\phi,z) = -\frac{1}{4\pi\varepsilon_0}\times\frac{1}{R_r}\times\left[-\frac{1}{v}u\left(t-\frac{z'}{v}-\frac{R_r}{c}\right)\right] \tag{6.10}$$

To find $\mathbf{H}$, take the curl of $d\mathbf{A}$ and integrate along the segment

$$\begin{aligned} H_r &= 0 \\ H_z &= 0 \\ H_\phi &= \int_0^h g(t)\,dz' \end{aligned} \tag{6.11}$$

where

$$g(t) = \frac{1}{4\pi}\left[\frac{r}{R_r^{\,3}}u\left(t-\frac{z'}{v}-\frac{R_r}{c}\right)+\frac{r}{cR_r^{\,2}}\delta\left(t-\frac{z'}{v}-\frac{R_r}{c}\right)\right] \tag{6.12}$$

Similarly, to find $\mathbf{E}$, substitute equations (6.9) and (6.10) into equation (6.1) and integrate along the segment.

$$\begin{aligned} E_r &= \int_0^h m(t)\,dz' \\ E_z &= \int_0^h n(t)\,dz' \\ E_\phi &= 0 \end{aligned} \tag{6.13}$$

where

$$m(t) = \frac{1}{4\pi v\varepsilon_0}\left[\frac{r}{R_r^{\,3}}u\left(t-\frac{z'}{v}-\frac{R_r}{c}\right)+\frac{1}{cR_r^{\,2}}\delta\left(t-\frac{z'}{v}-\frac{R_r}{c}\right)\right] \tag{6.14}$$

$$n(t) = \frac{1}{4\pi v\varepsilon_0}\left[\frac{z-z'}{R_r^{\,3}}u\left(t-\frac{z'}{v}-\frac{R_r}{c}\right)+\frac{z-z'}{cR_r^{\,2}}\delta\left(t-\frac{z'}{v}-\frac{R_r}{c}\right)\right]-\frac{\mu_0}{4\pi}\frac{1}{R_r}\delta\left(t-\frac{z'}{v}-\frac{R_r}{c}\right) \tag{6.15}$$

For the integrals $\int g(t)\,dz'$, $\int m(t)\,dz'$ and $\int n(t)\,dz'$, the integrand contains either the Heaviside step function or the Dirac delta function with the argument

$$\psi(t) = t - \frac{z'}{v} - \frac{R_r}{c} \tag{6.16}$$

The zero of this function can by found as:

$$\zeta_0(t) = \frac{\frac{t}{v} - \frac{z}{c^2} - \sqrt{\left(\frac{t}{v} - \frac{z}{c^2}\right)^2 - \left(\frac{1}{v^2} - \frac{1}{c^2}\right)\left(t^2 - \frac{r^2}{c^2} - \frac{z^2}{c^2}\right)}}{\frac{1}{v^2} - \frac{1}{c^2}} \tag{6.17}$$

For **E** and **H**, the Dirac delta term is equal to zero except when $z' = \zeta_0(t)$ and the Heaviside step term is equal to zero for $z' > \zeta_0(t)$.Therefore, when $\zeta_0(t) < 0$, both Heaviside step and Dirac delta functions are zero and when $\zeta_0(t) > h$, the Dirac delta function is zero while the Heaviside step function has a value of 1 for $0 \le z' \le h$. For $0 \le \zeta_0(t) \le h$, the upper limit for the integral can be changed to $\zeta_0(t)$.

Hence if we let

$$\theta(z_i') = \tan^{-1}\left(\frac{z_i' - z}{r}\right) \tag{6.18}$$

and

$$R_{r,0} = \sqrt{r^2 + \left[\zeta_0(t) - z\right]^2} \tag{6.19}$$

such that the expressions for the integrals of $g(t)$, $m(t)$ and $n(t)$ can be written as shown in equations (6.20), (6.21) and (6.22) where the ranges $\zeta_0(t) < 0$, $0 \le \zeta_0(t) \le h$

and $\zeta_0(t) > h$ correspond to $t < \frac{\sqrt{r^2+z^2}}{c}$, $\frac{\sqrt{r^2+z^2}}{c} \le t \le \frac{h}{v} + \frac{\sqrt{r^2+(z-h)^2}}{c}$ and $t > \frac{h}{v} + \frac{\sqrt{r^2+(z-h)^2}}{c}$ respectively.

$$\int_0^h g(t)\,dz' = \begin{cases} 0, & \zeta_0(t) < 0 \\ \frac{1}{4\pi}\left[\frac{\sin\left[\theta(\zeta_0(t))\right]-\sin\left[\theta(0)\right]}{r} + \frac{r}{c\left(R_{r,0}\right)^2\left|-\frac{1}{v}-\frac{\zeta_0(t)-z}{cR_{r,0}}\right|}\right], & 0 \le \zeta_0(t) \le h \\ \frac{1}{4\pi}\left[\frac{\sin\left[\theta(h)\right]-\sin\left[\theta(0)\right]}{r}\right], & \zeta_0(t) > h \end{cases} \tag{6.20}$$

$$\int_0^h m(t)\,dz' = \begin{cases} 0, & \zeta_0(t) < 0 \\ \frac{1}{4\pi v\varepsilon_0}\left[\frac{\sin\left[\theta(\zeta_0(t))\right]-\sin\left[\theta(0)\right]}{r} + \frac{r}{c\left(R_{r,0}\right)^2\left|-\frac{1}{v}-\frac{\zeta_0(t)-z}{cR_{r,0}}\right|}\right], & 0 \le \zeta_0(t) \le h \\ \frac{1}{4\pi v\varepsilon_0}\left[\frac{\sin\left[\theta(h)\right]-\sin\left[\theta(0)\right]}{r}\right], & \zeta_0(t) > h \end{cases} \tag{6.21}$$

$$\int_0^h n(t)\,dz' = \begin{cases} 0, & \zeta_0(t) < 0 \\ \dfrac{1}{4\pi v\varepsilon_0}\left[\dfrac{\cos\left[\theta\left(\zeta_0(t)\right)\right]-\cos\left[\theta(0)\right]}{r}+\dfrac{z-\zeta_0(t)}{c\left(R_{r,0}\right)^2\left|-\frac{1}{v}-\frac{\zeta_0(t)-z}{cR_{r,0}}\right|}\right] & 0 \le \zeta_0(t) \le h \\ -\dfrac{\mu}{4\pi}\dfrac{1}{R_{r,0}\left|-\frac{1}{v}-\frac{\zeta_0(t)-z}{cR_{r,0}}\right|}, & \\ \dfrac{1}{4\pi v\varepsilon_0}\left[\dfrac{\cos\left[\theta(h)\right]-\cos\left[\theta(0)\right]}{r}\right], & \zeta_0(t) > h \end{cases} \tag{6.22}$$

The expressions derived so far are for a Heaviside step current travelling through a straight vertical segment. (See Appendix A for detailed derivation.) To evaluate the fields $f(t)$ corresponding to an arbitrary current waveform $i_r(t)$, representing the return stroke current propagating along the segment, a convolution integral is performed with the corresponding unit step response $s(t)$.

$$f(t) = \int_0^t \frac{di_r(\tau)}{d\tau} \cdot s(t-\tau)\,d\tau \tag{6.23}$$

As with most lightning models, a perfectly conducting ground is assumed and thus, the method of images can be applied. A similar analysis can be followed to obtain the contributions of the images below ground.

6.1.2 Geometrical Transformation for a Segment of Arbitrary Location and Orientation

The coordinate axes need to be realigned such that the segment of arbitrary location and slope lies on the vertical z-axis for the application of the equations derived.

Referring to Figure 6.2, the origin is first translated such that it lies on the base of the segment. The coordinate axes are then rotated along the z_1-axis by ϕ, which is the angle made by the projection of the segment on the x_1-y_1 plane, followed by a rotation along the y_1-axis by θ, which is the angle between the segment and the z_1-axis.

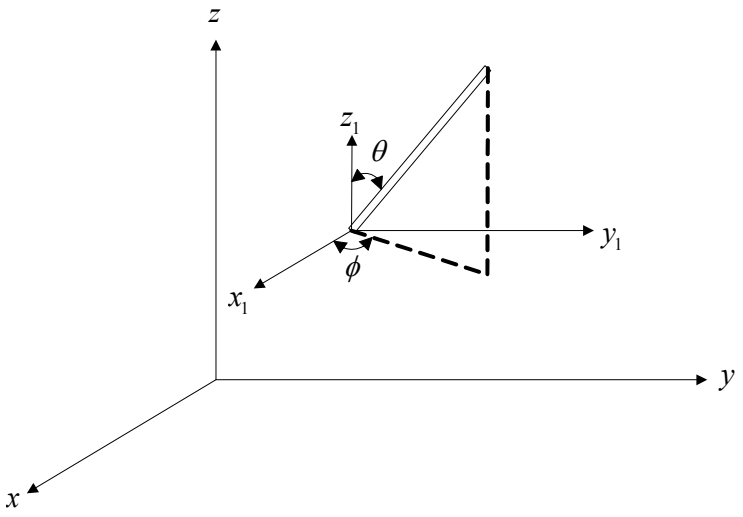

Figure 6.2 Geometrical representation of transformation parameters

The rotation of the axes transforms the observation point P and its new coordinates with respect to the new origin can be determined from the transformation matrix shown in (6.24):

$$\begin{bmatrix} x_p \\ y_p \\ z_p \end{bmatrix} = \begin{bmatrix} \cos\theta\cos\phi & \cos\theta\sin\phi & -\sin\theta \\ -\sin\phi & \cos\phi & 0 \\ \sin\theta\cos\phi & \sin\theta\sin\phi & \cos\theta \end{bmatrix} \begin{bmatrix} x_1 \\ y_1 \\ z_1 \end{bmatrix} \tag{6.24}$$

And after the electromagnetic fields with respect to the shifted coordinate axes are found, their values with respect to the original coordinate axes can be obtained from the following inverse transformation matrix:

$$\mathbf{T} = \begin{bmatrix} \cos\theta\cos\phi & -\sin\phi & \sin\theta\cos\phi \\ \cos\theta\sin\phi & \cos\phi & \sin\theta\sin\phi \\ -\sin\theta & 0 & \cos\theta \end{bmatrix} \tag{6.25}$$

6.1.3 Comparison with Lupò *et al.*'s Model

In the formulation presented by Lupò *et al*. discussed in Section 3.8 [6], the current distribution assumed and the corresponding charge distribution are reproduced here:

$$i(z',t) = u\left(t - \frac{z'}{v}\right) \times \left[u(z') - u(z'-h)\right] \tag{6.26}$$

$$\begin{aligned} \lambda(z',t) = -\Bigg\{ & tu(t)\delta(z') - \left(t - \frac{h}{v}\right)u\left(t - \frac{h}{v}\right)\delta(z'-h) \\ & - \frac{1}{v}u\left(t - \frac{z'}{v}\right)\left[u(z') - u(z'-h)\right]\Bigg\} \end{aligned} \tag{6.27}$$

The first two terms within the curly brackets of (6.27) constitute an accumulation of charge at the bottom and top of the segment which increases with time. This results in the remote electromagnetic fields diverging infinitely. When the convolution integral with a current which decays to zero is performed to find the fields, the field waveforms converge to a finite value, given that the charge accumulation also converges, rather than decays to zero. This is physically incorrect.

The key difference in the corrected formulation is the removal of the expression $\left[u(z') - u(z'-h)\right]$ in the current distribution. The purpose of this expression is to ensure that the current propagating along the straight vertical segment is bounded within its height. But since the integrals performed to find **E** and **H** have limits 0 and h,

the absence in the expression is justified. Thus the coherence of the improved model is maintained while addressing the error found in Lupò *et al*.'s model.

6.2 PROPOSED MODEL

6.2.1 Lightning Parameters

As with the *R-L-C* model, the 30 kA peak return stroke current in the DU model was adopted for consistency. The vertical height of the lightning channel was also set to 5 km and the return stroke speed was set to a constant value of 1.5×10^8 m/s.

6.2.2 Random Tortuous Lightning Channel

Hill found the absolute value of the angles between segments to fit the Gaussian distribution and its mean is about 16° [43]. This value was corroborated with a set of similar measurement made by Idone and Orville [44]. In both sets of measurements, the angles were obtained from lightning photographs and represent the angle from a two-dimensional perspective. In the approach to generating a random tortuous lighting stroke path of vertical height of 5 km, it was the angle made with the vertical which was set to follow a Gaussian distribution rather than the angle between segments. This avoids the occurrence of loops or spirals within the channel or an unrealistically long channel which changes direction vertically repeatedly. But even in doing so, the three-dimensional angle between segments of the randomly generated lightning channel was designed such that its mean was 16.0° so as to maintain coherency with the measurements by Hill, and Idone and Orville.

Typical step lengths average tens of meters and this was taken into consideration when randomly generating the segment lengths. For the random tortuous lightning stroke path shown in Fig. 6.3, the segment lengths range from 14.9 m to 120.1 m. The azimuthal directions for each segment was also generated randomly.

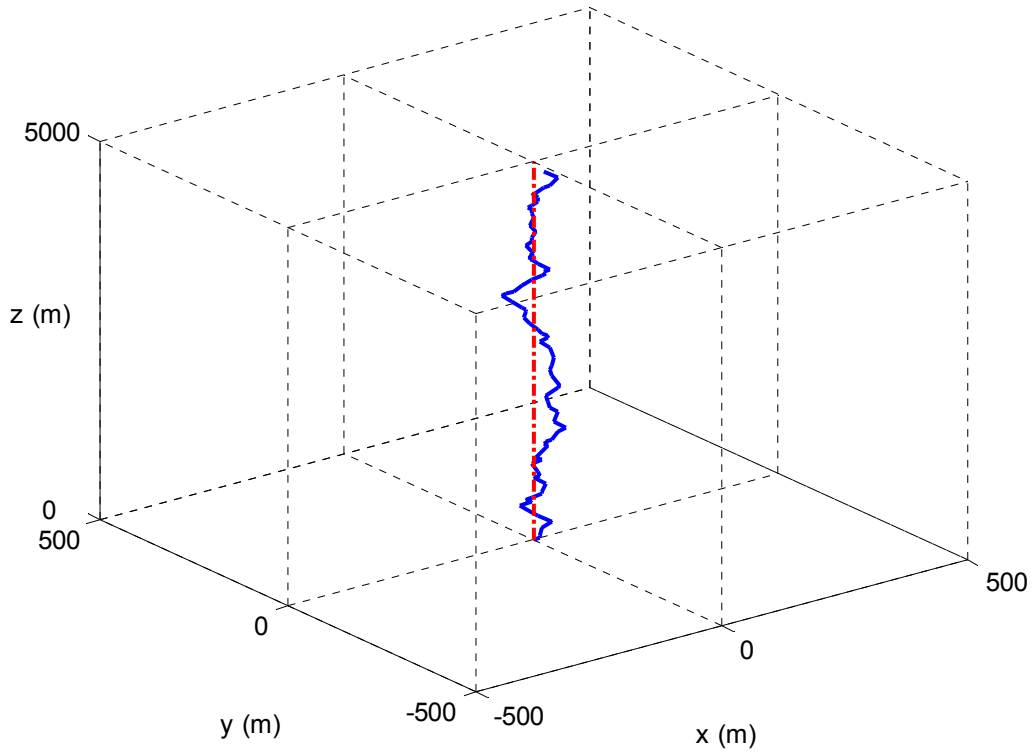

Figure 6.3 Randomly generated lightning stroke path (shown against a straight vertical channel)

6.2.3 Results and Observations

The electromagnetic fields were calculated for 6 different observation points. N1, N2 and N3 represent near points 100 m from the lightning incident point at ground with coordinates (100,0,0), (100,0,10) and (100,0,100) respectively while F1 F2 and F3 represent far points 100000 m away with coordinates (100000,0,0), (100000,0,10) and

(100000,0,100) respectively. At both distances, the fields were evaluated at ground level, 10 m above ground and 100 m above ground.

Together with the electromagnetic fields due to a straight vertical channel, the waveforms are shown in Figures 6.4 to 6.9. It should be noted that the y-axes for the fields due to the tortuous and straight channels are plotted with an offset so that the two curves can be seen clearly and compared. Certain components of the electromagnetic fields are zero throughout and therefore are not shown.

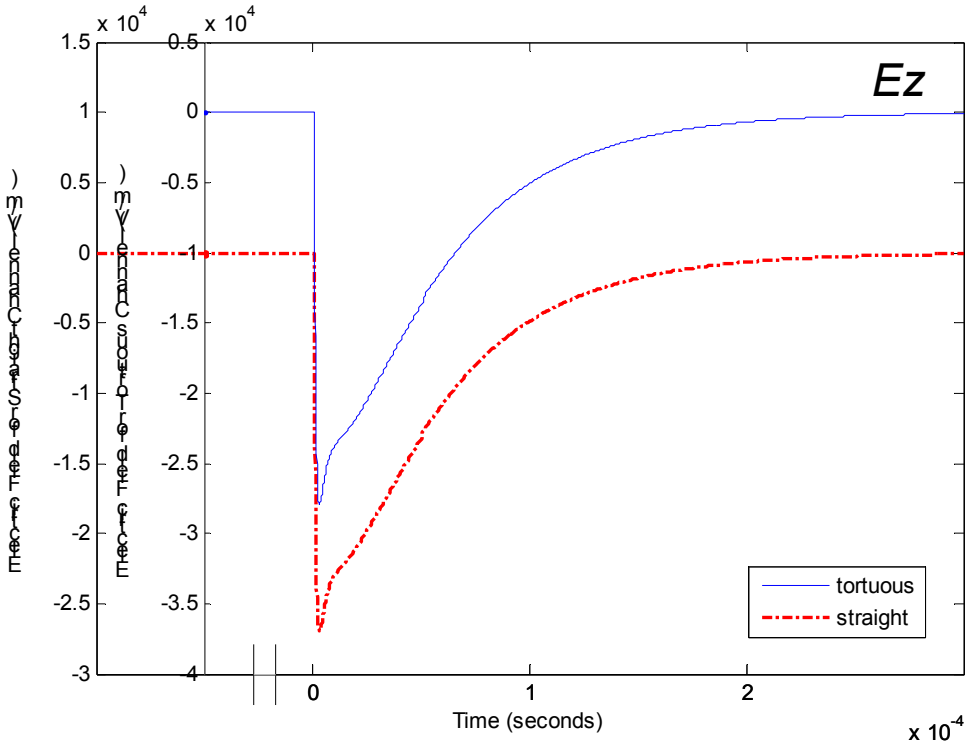

(a) *z*-component of *E*

Figure 6.4 Electromagnetic fields at N1 (100,0,0)

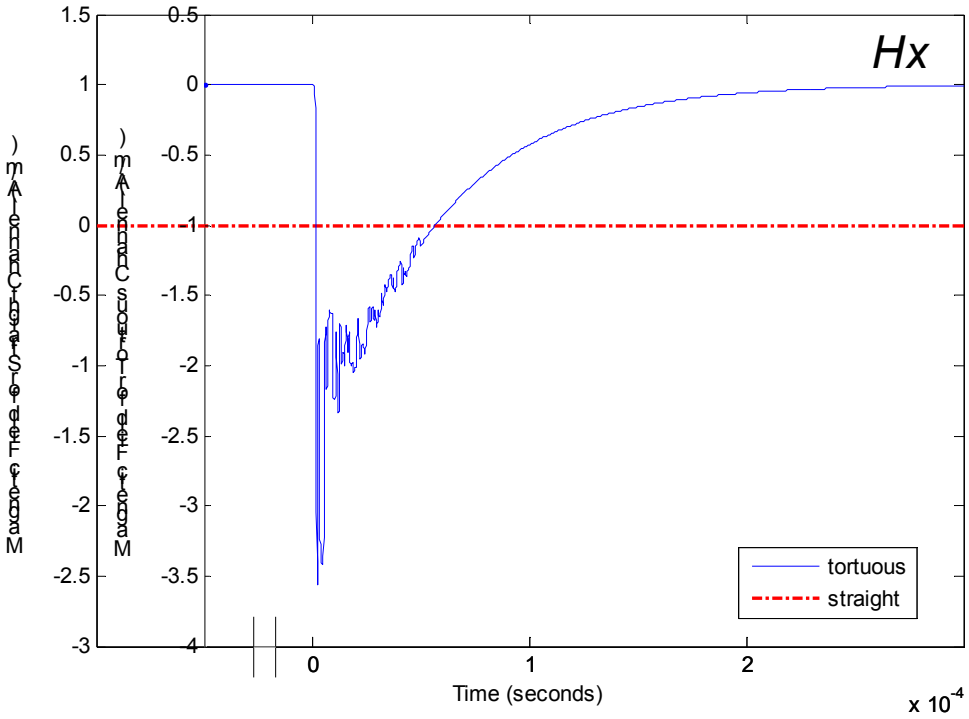

(b) x-component of H

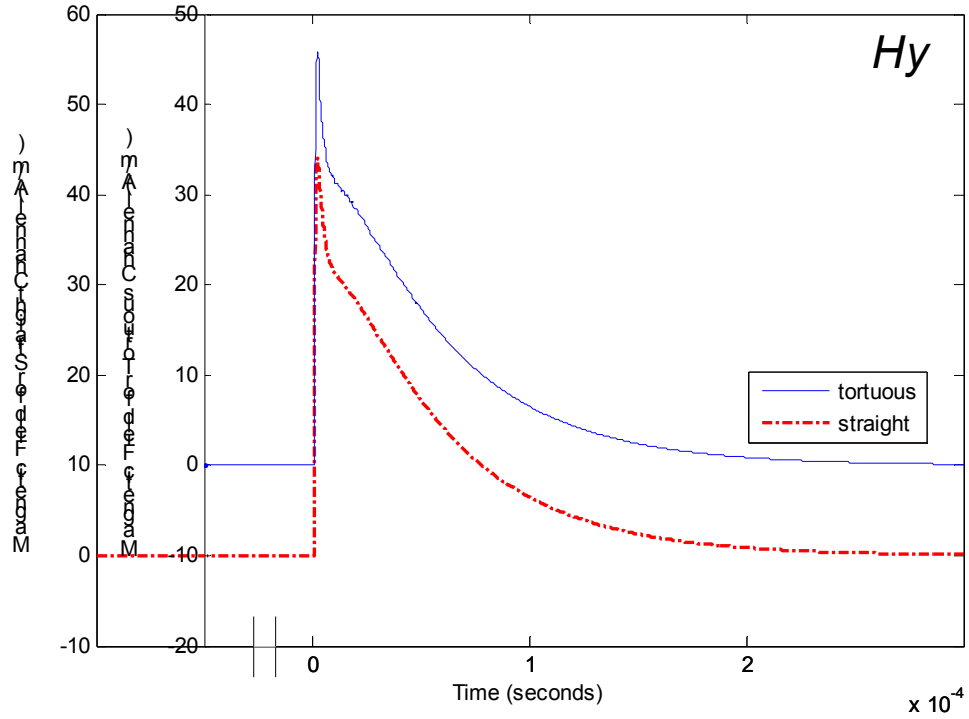

(c) y-component of H

Figure 6.4 Electromagnetic fields at N1 (100,0,0)

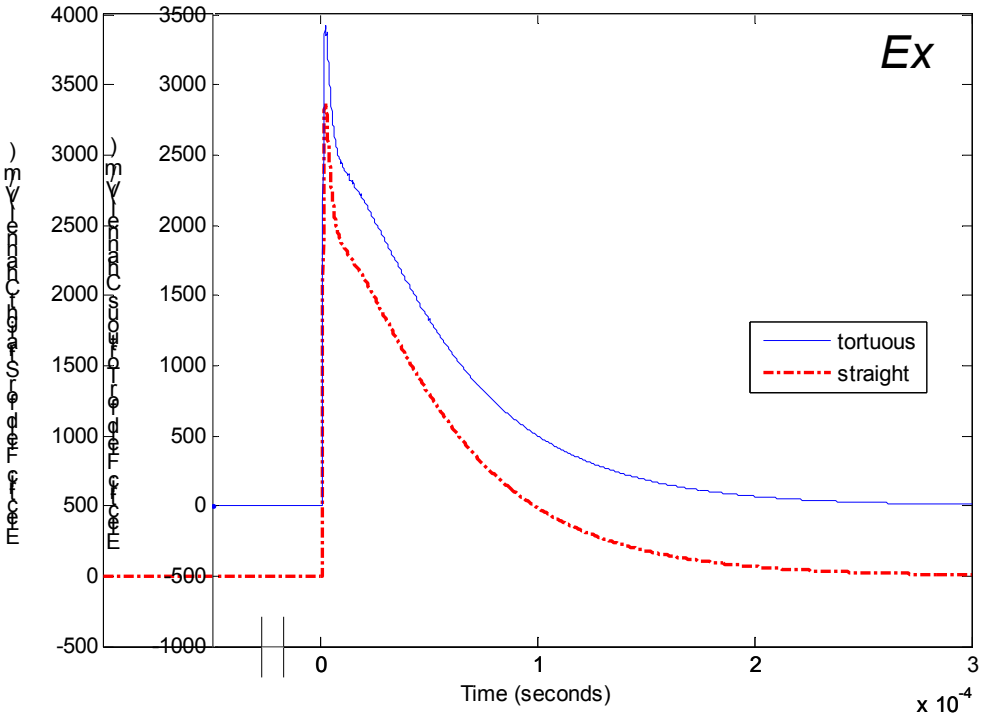

(a) x-component of E

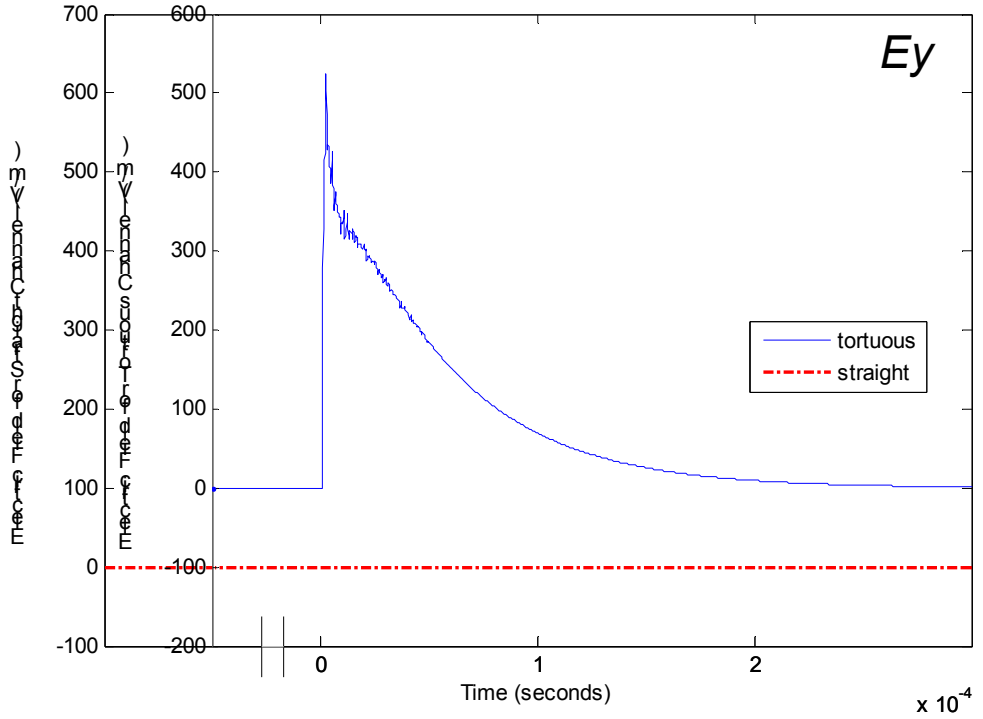

(b) y-component of E

Figure 6.5 Electromagnetic fields at N2 (100,0,10)

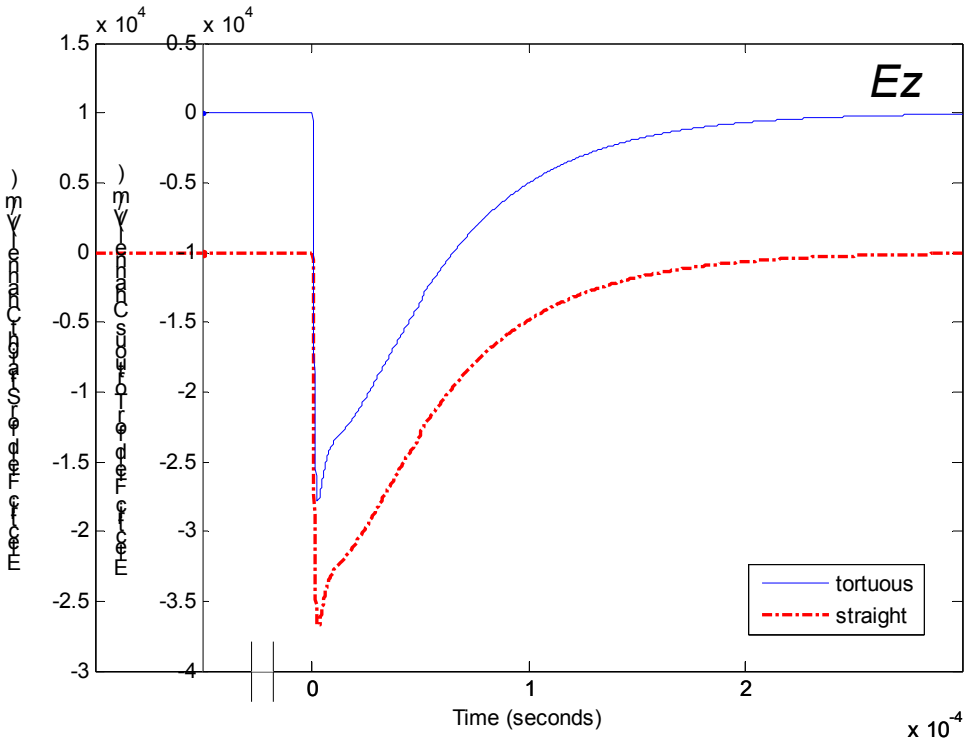

(c) *z*-component of *E*

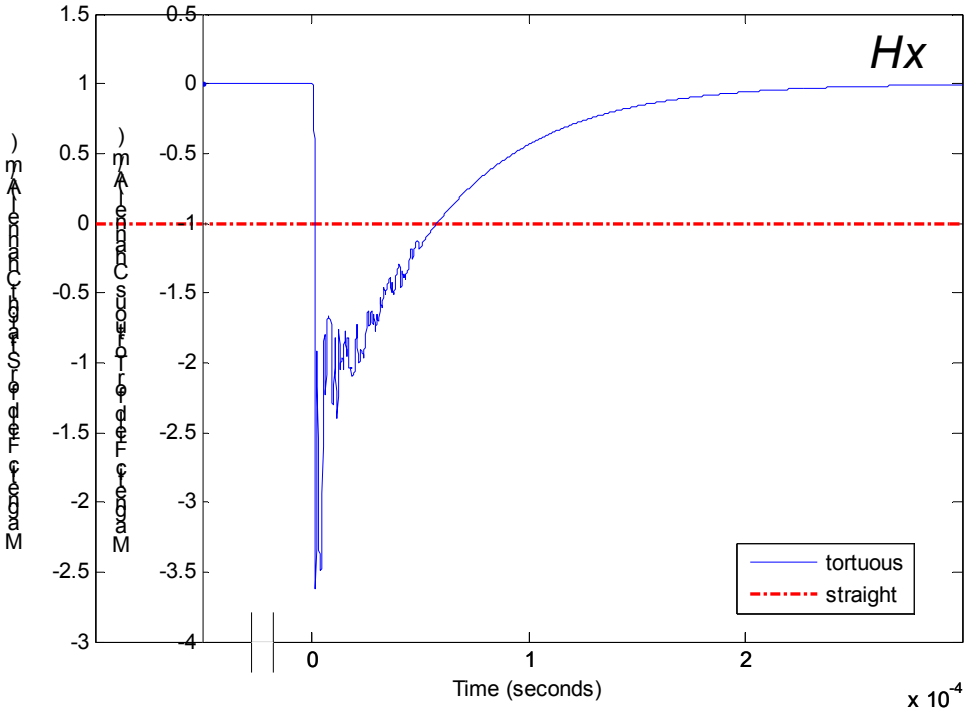

(d) *x*-component of *H*

Figure 6.5 Electromagnetic fields at N2 (100,0,10)

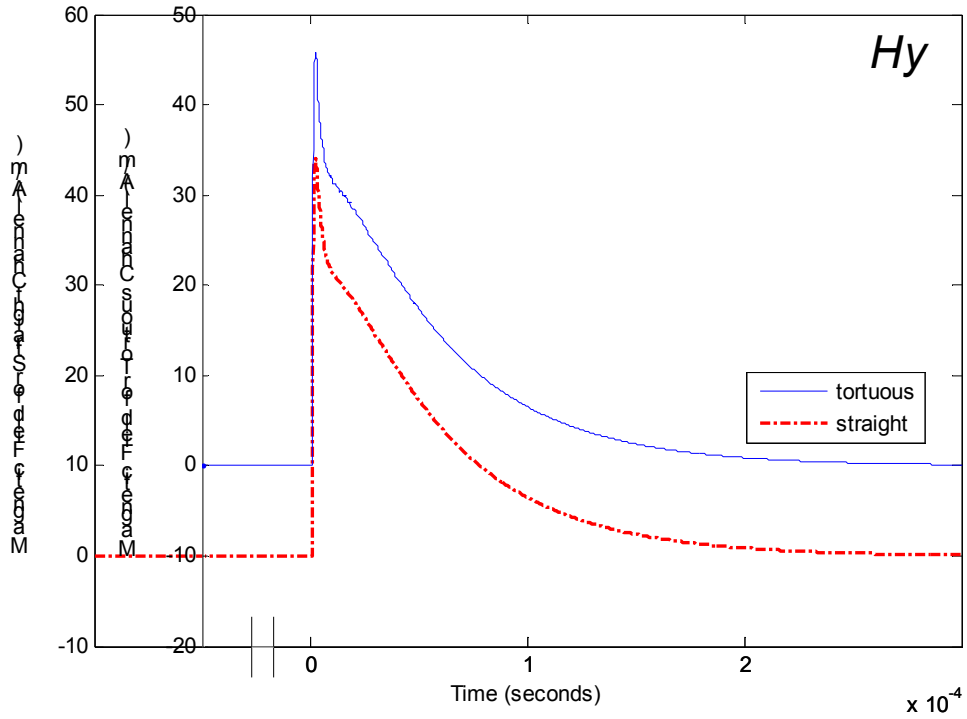

(e) *y*-component of *H*

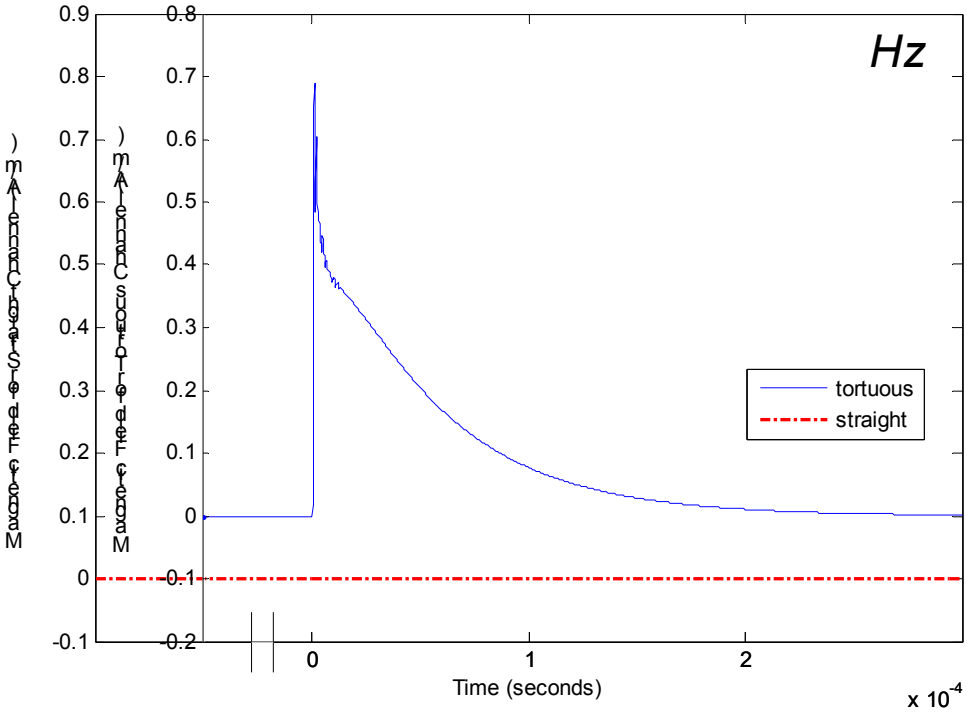

(f) *z*-component of *H*

Figure 6.5 Electromagnetic fields at N2 (100,0,10)

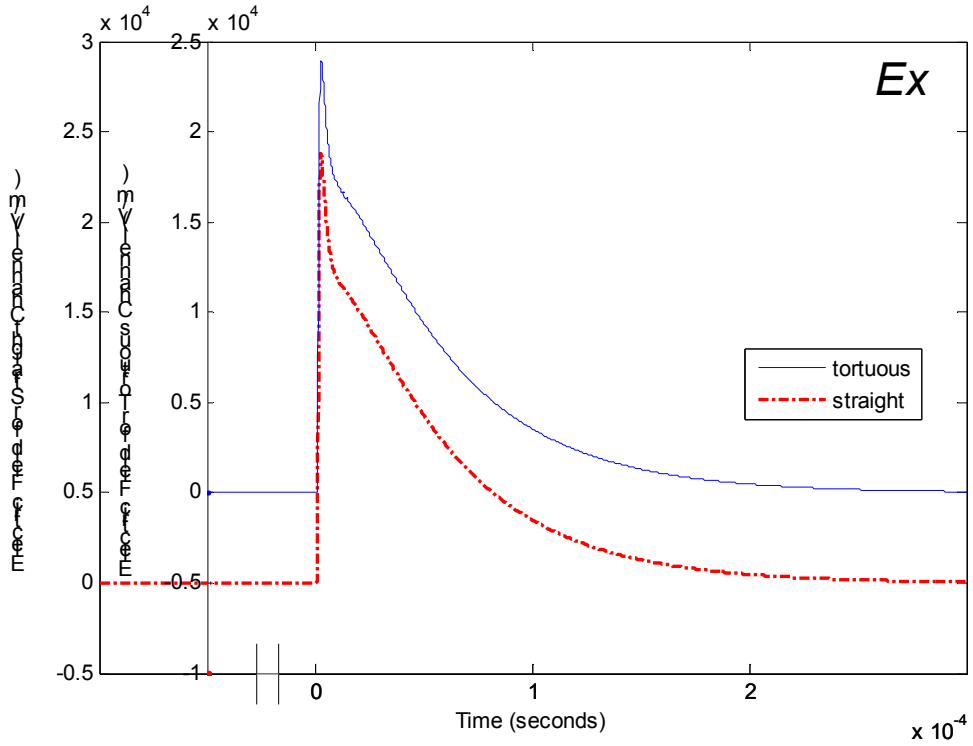

(a) *x*-component of *E*

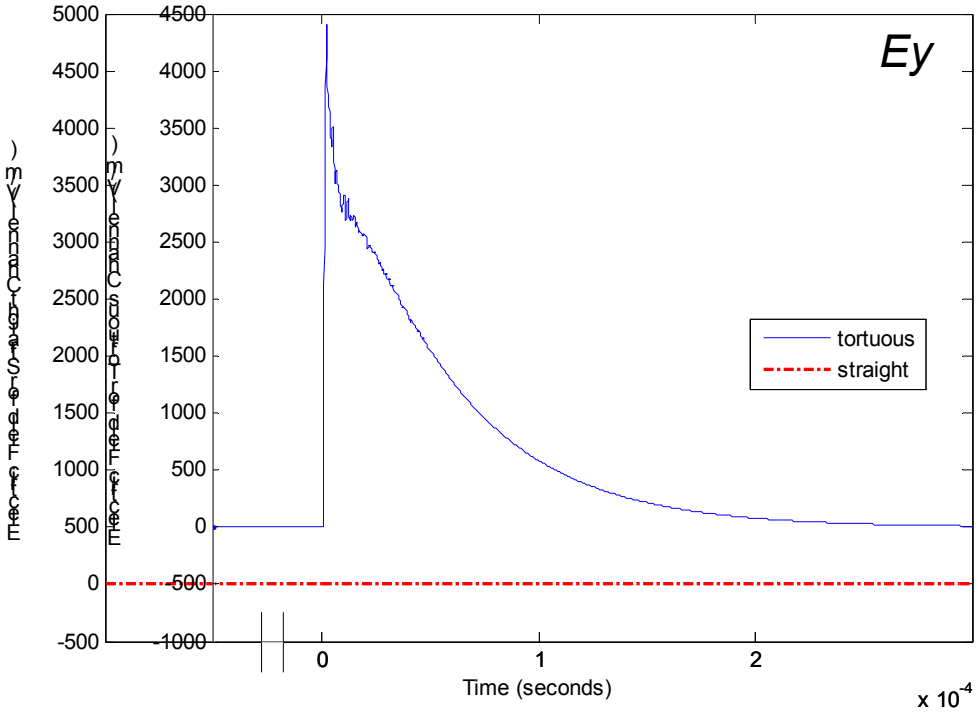

(b) *y*-component of *E*

Figure 6.6 Electromagnetic fields at N3 (100,0,100)

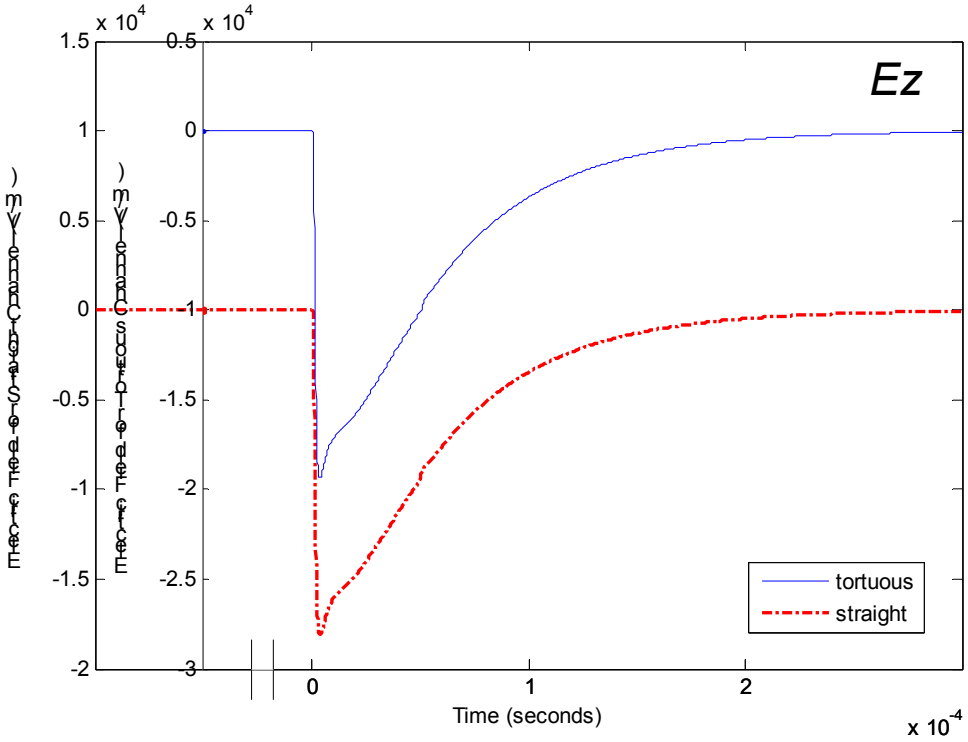

(c) *z*-component of *E*

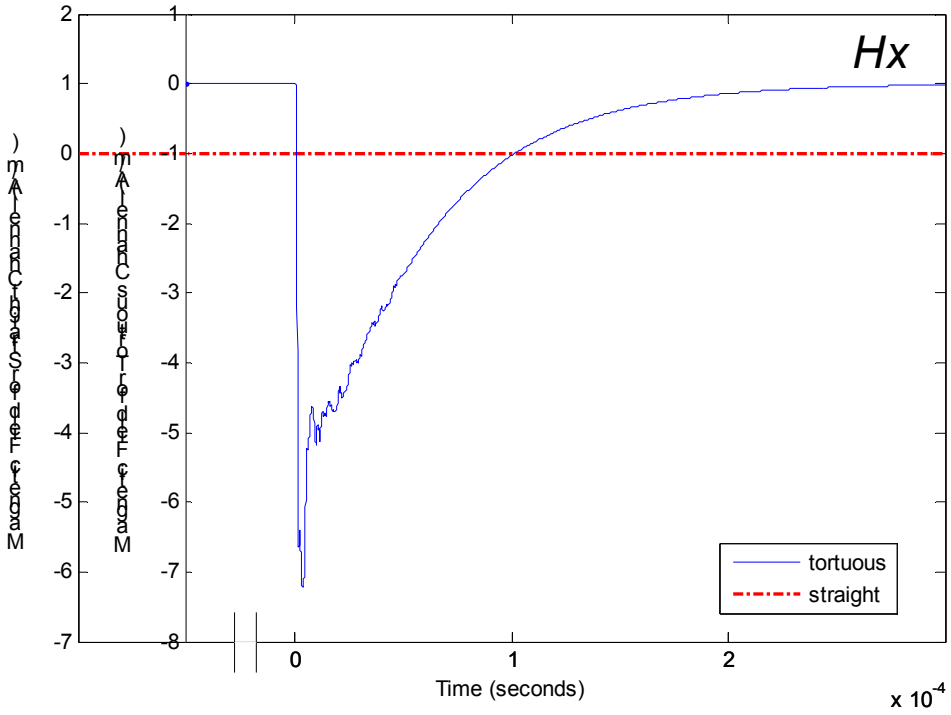

(d) *x*-component of *H*

Figure 6.6 Electromagnetic fields at N3 (100,0,100)

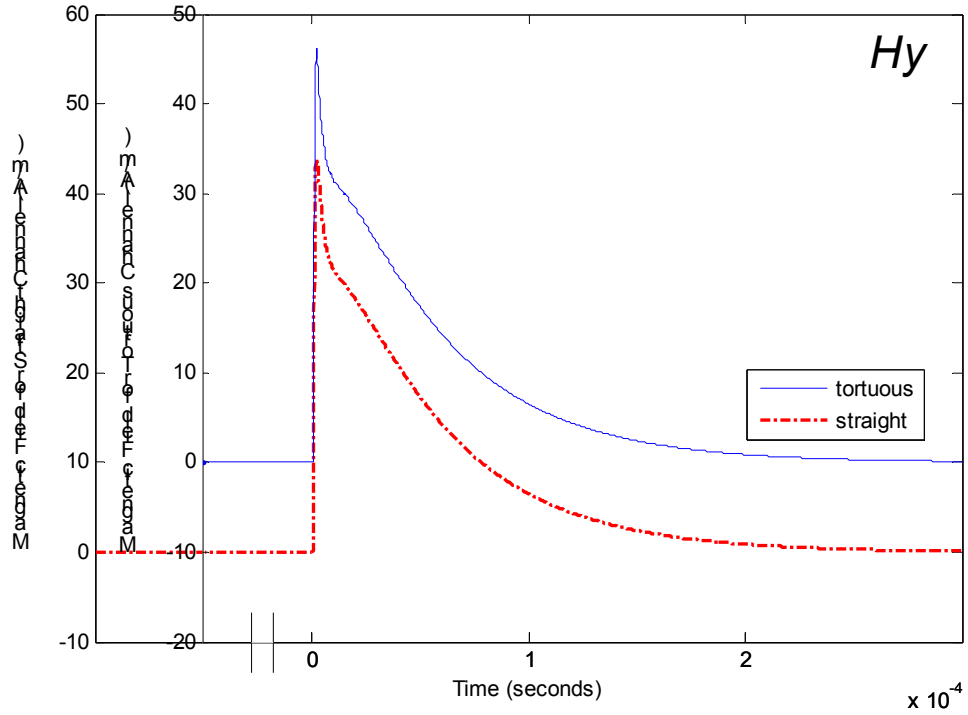

(e) *y*-component of *H*

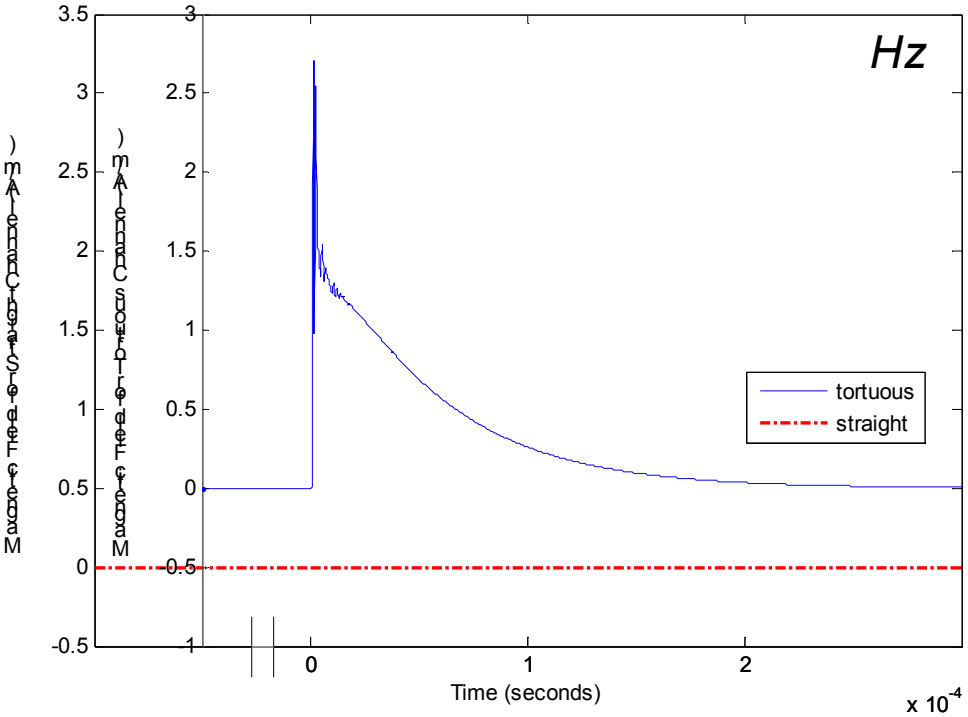

(f) *z*-component of *H*

Figure 6.6 Electromagnetic fields at N3 (100,0,100)

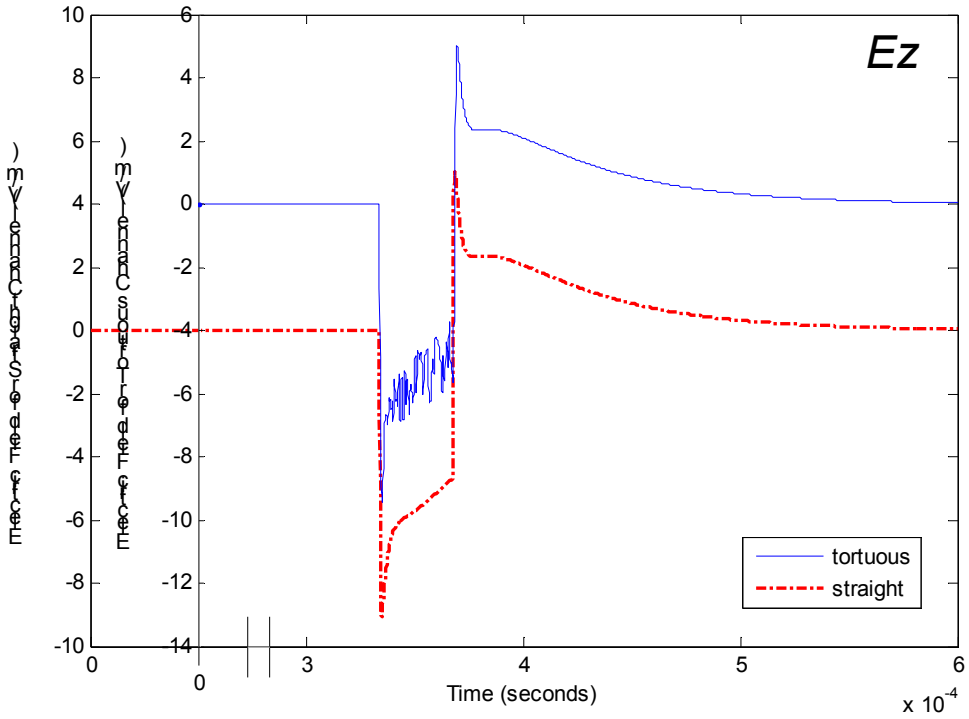

(a) *z*-component of *E*

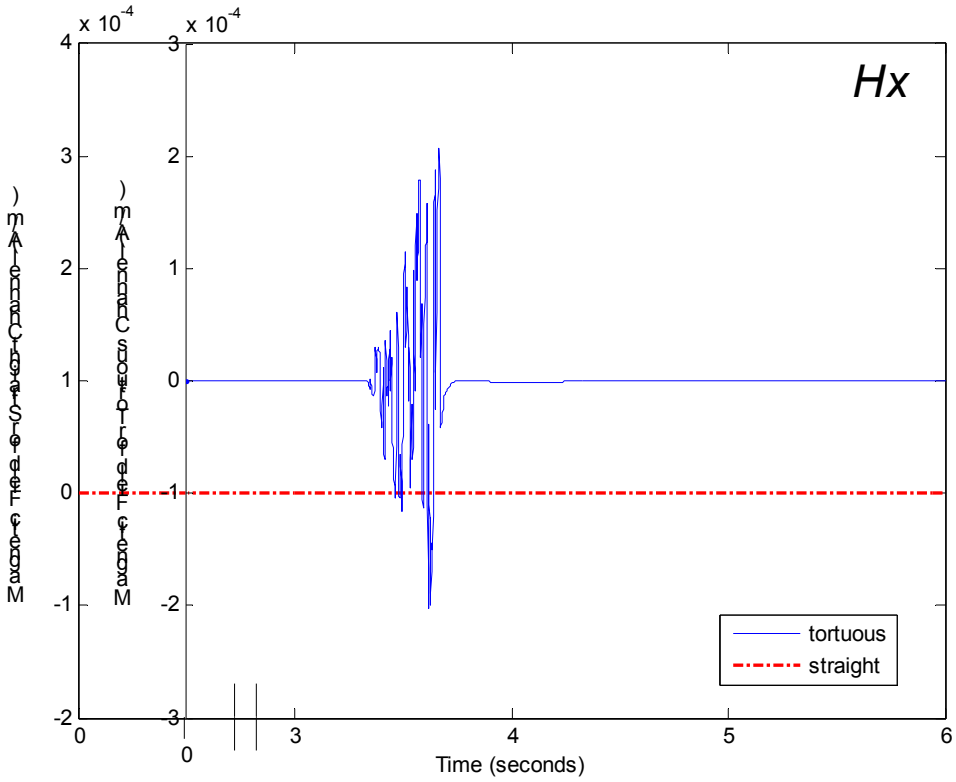

(b) *x*-component of *H*

Figure 6.7 Electromagnetic fields at F1 (100000,0,0)

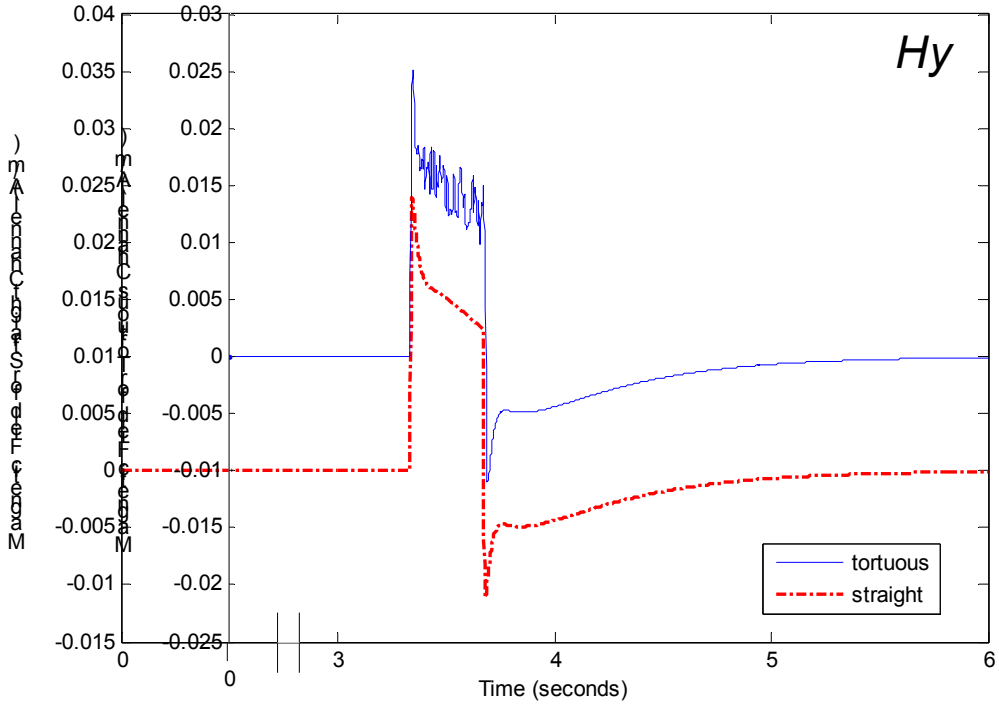

(c) *y*-component of *H*

Figure 6.7 Electromagnetic fields at F1 (100000,0,0)

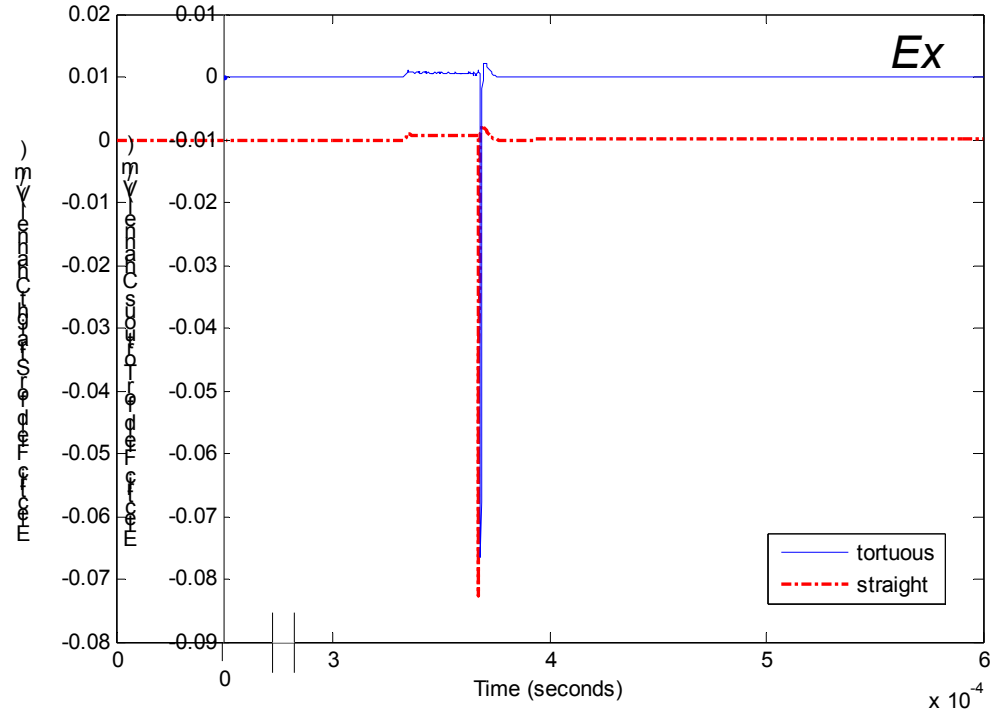

(a) *x*-component of *E*

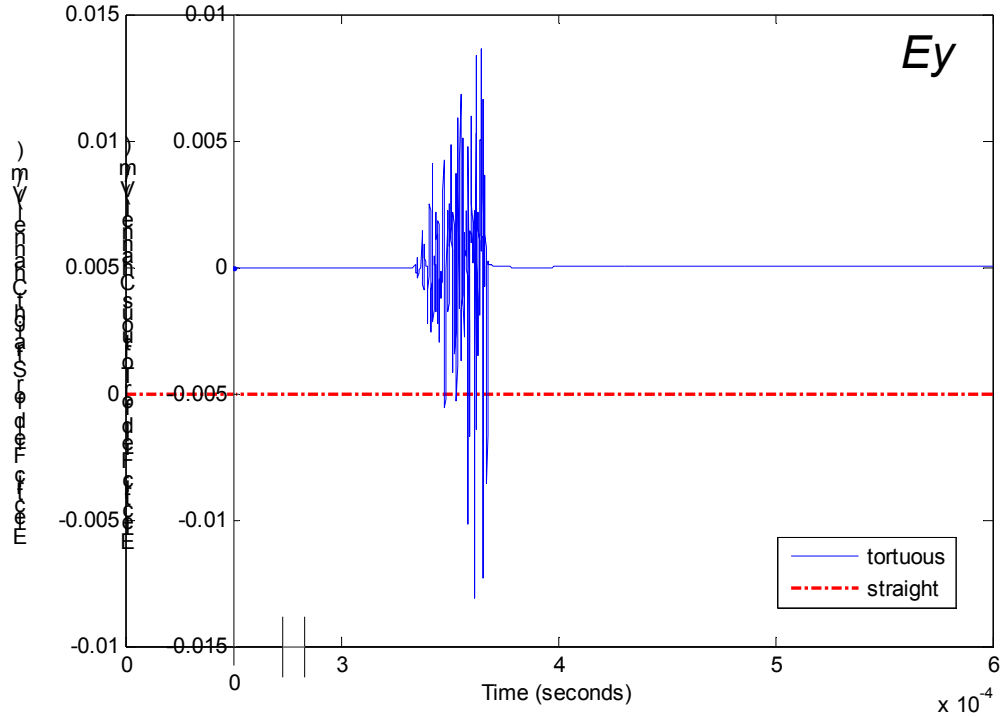

(b) *y*-component of *E*

Figure 6.8 Electromagnetic fields at F2 (100000,0,10)

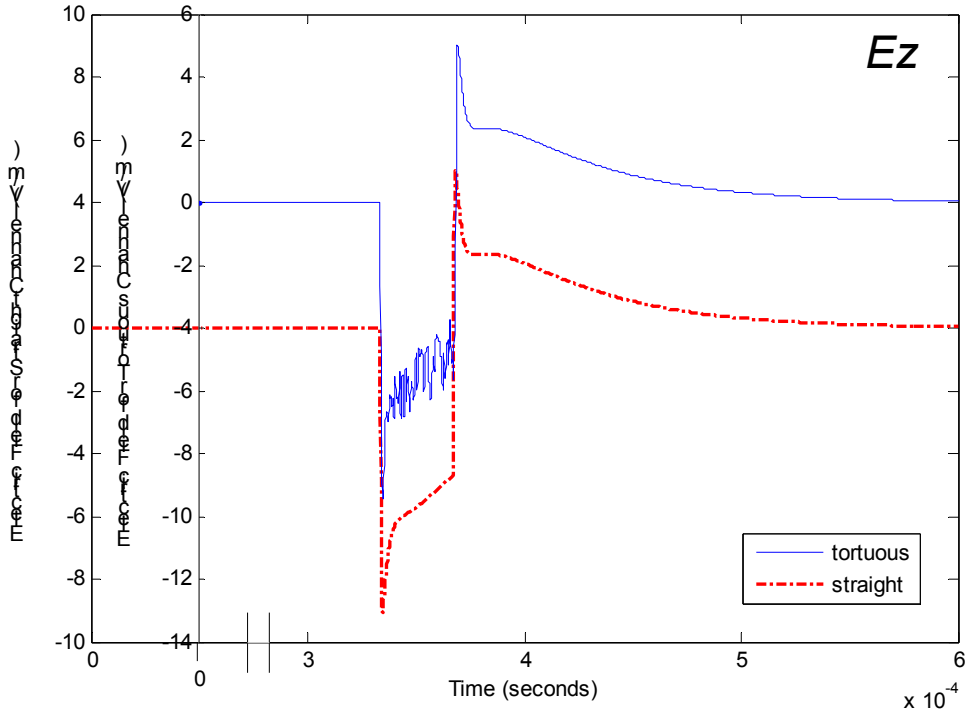

(c) *z*-component of *E*

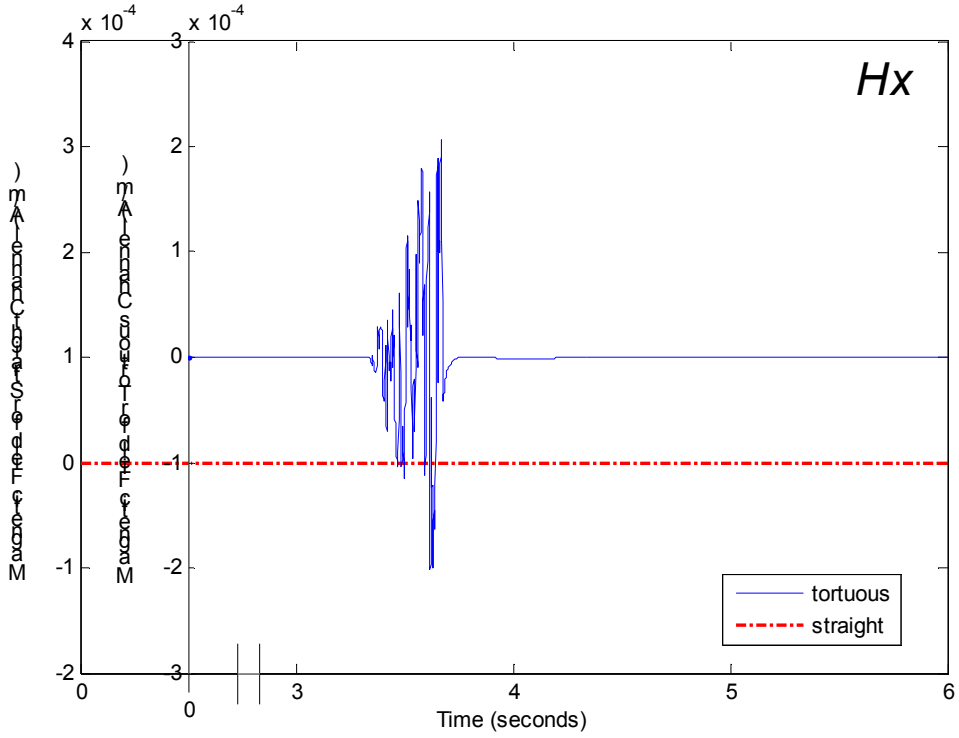

(d) *x*-component of *H*

Figure 6.8 Electromagnetic fields at F2 (100000,0,10)

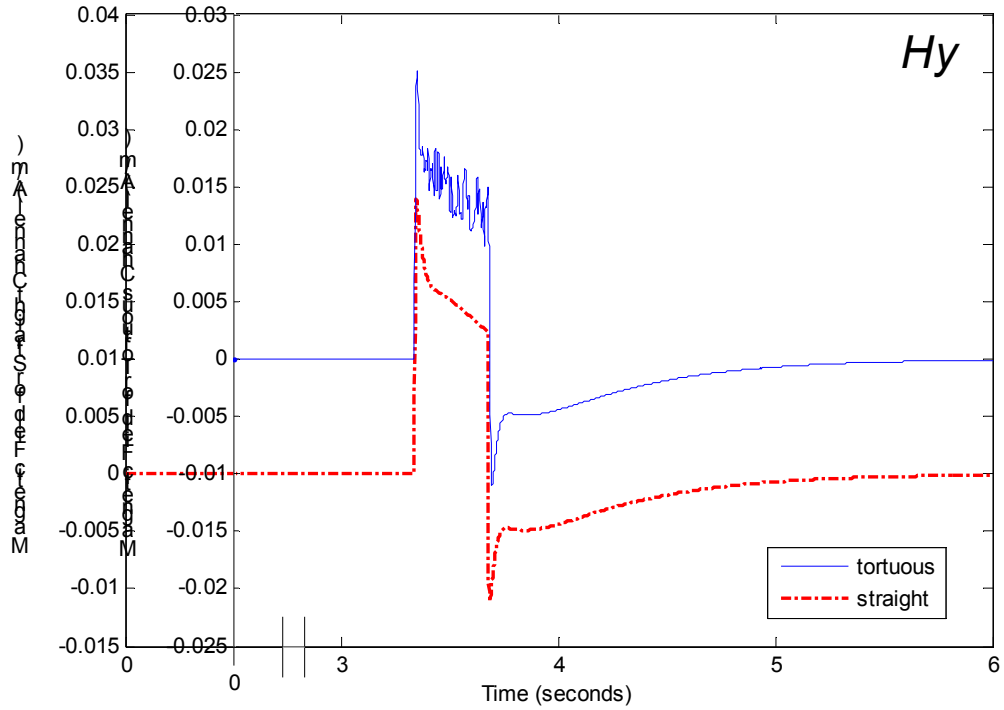

(e) *y*-component of *H*

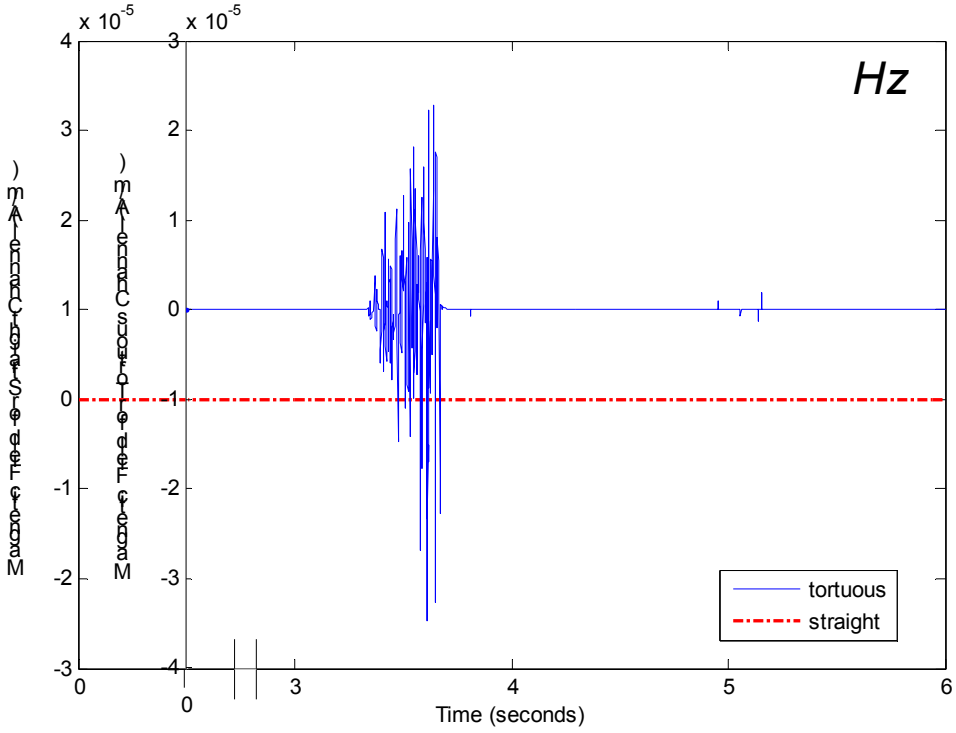

(f) *z*-component of *H*

Figure 6.8 Electromagnetic fields at F2 (100000,0,10)

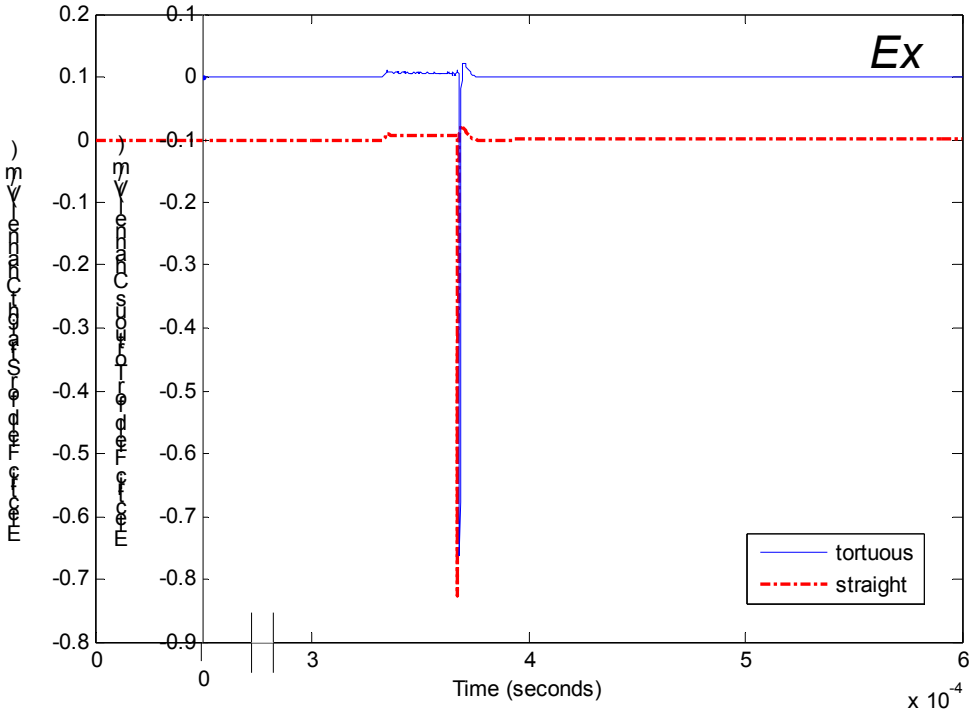

(a) *x*-component of *E*

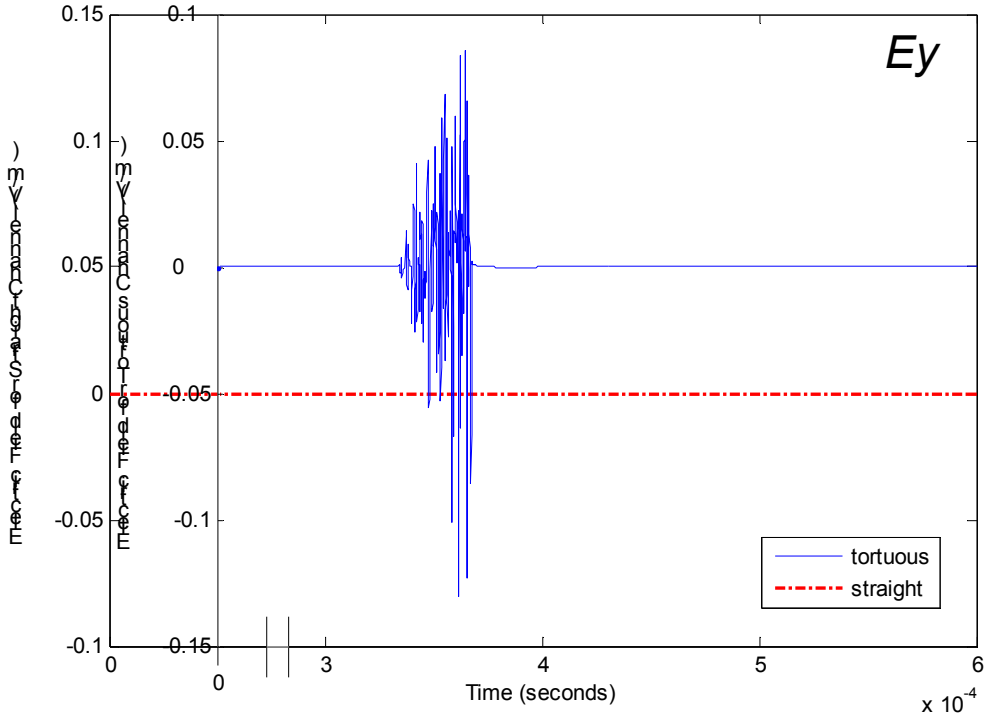

(b) *y*-component of *E*

Figure 6.9 Electromagnetic fields at F3 (100000,0,100)

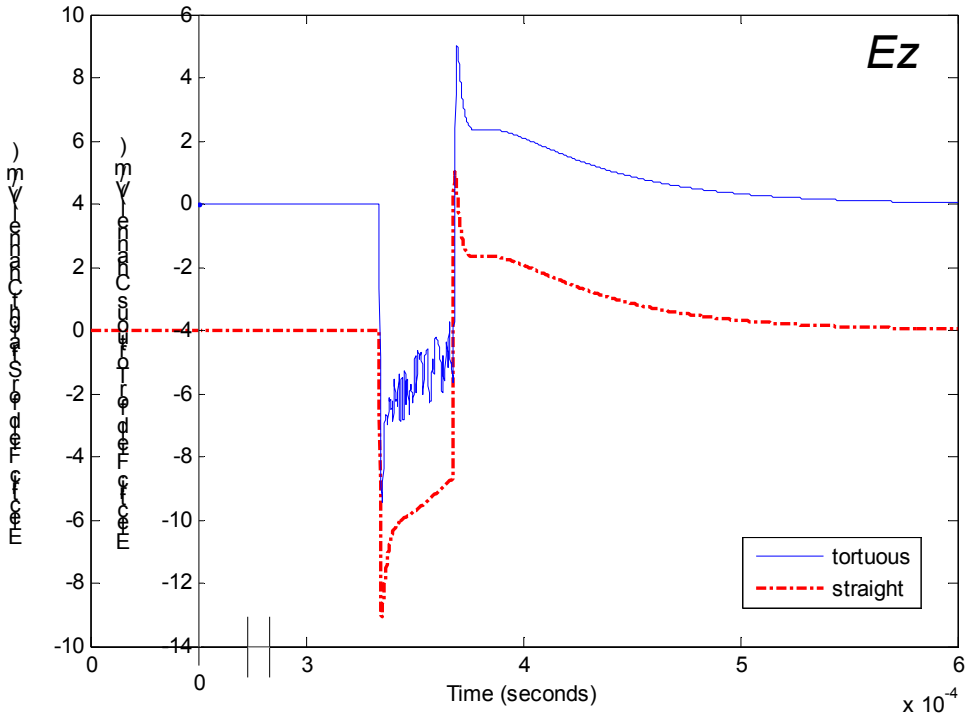

(c) *z*-component of *E*

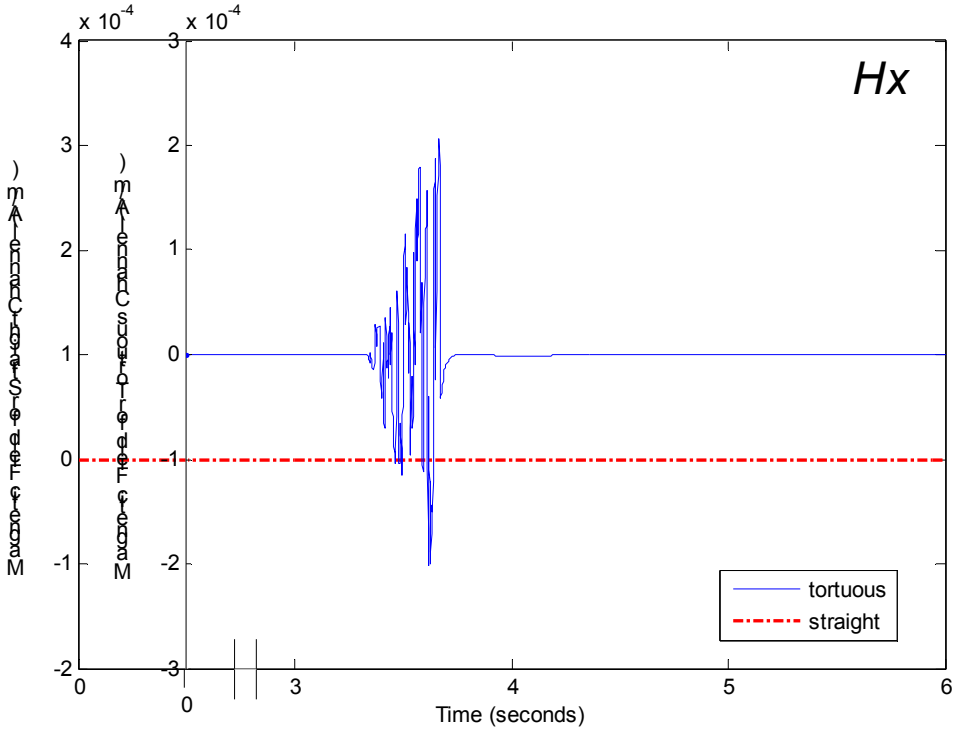

(d) *x*-component of *H*

Figure 6.9 Electromagnetic fields at F3 (100000,0,100)

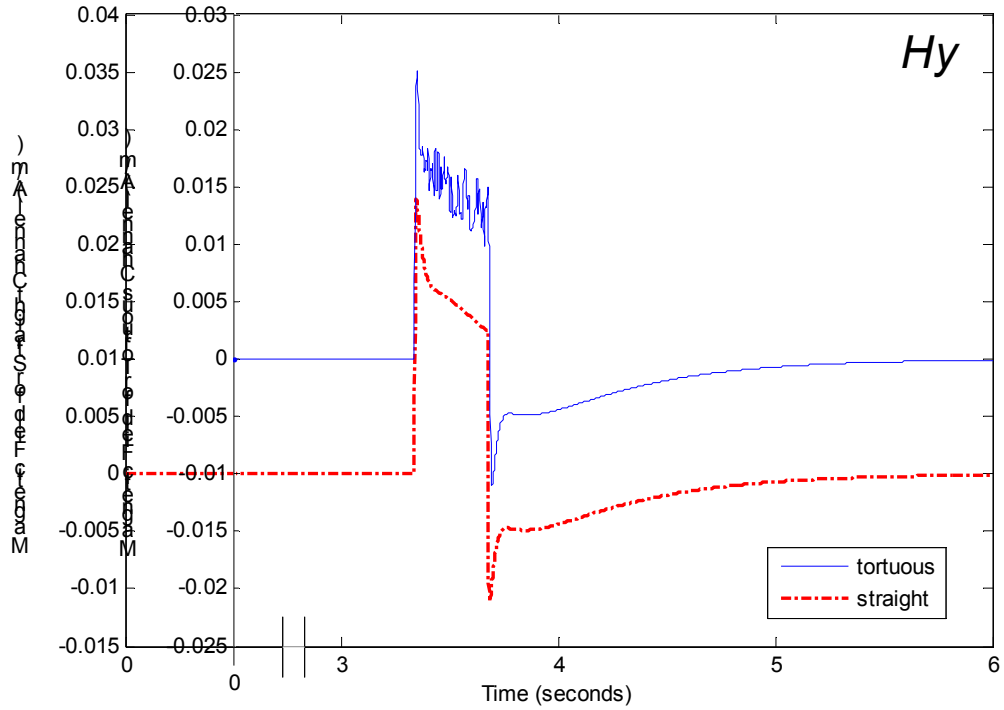

(e) *y*-component of *H*

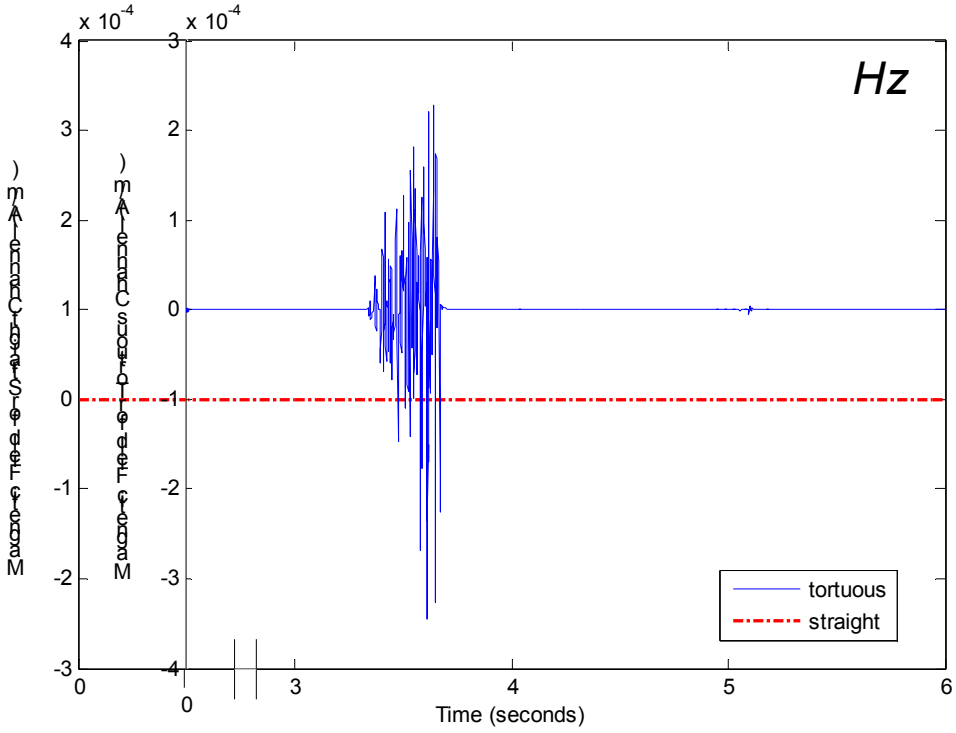

(f) *z*-component of *H*

Figure 6.9 Electromagnetic fields at F3 (100000,0,100)

For the electromagnetic fields at ground, the horizontal components of the electric field and vertical components of the magnetic field are zero as expected. This is consistent with the understanding of the boundary conditions governing electromagnetic fields at the perfectly conducting ground plane that the tangential component of the electric field and the normal component of the magnetic field are zero.

For the straight channel, the *y*-component of the electric field was zero throughout because the observation point lies along *x*-axis and it is known that the azimuthal component is zero. Similarly, the *x*- and *z*-components of the magnetic fields are also zero.

The electromagnetic fields due to the tortuous channel exhibit a more fine structure, indicating more significant high frequency components, compared with the fields due to a straight channel. This is more coherent with actual measurements [18, 44]. A sharp initial peak in both electric and magnetic fields measured for distances beyond a kilometre was observed by Lin *et al*. as seen in Figure 2.3 and this feature was also evident in the waveforms calculated [18]. The characteristic zero-crossing for far fields was also present.

A key observation is that the electromagnetic fields for both the straight and tortuous channels are comparable. The waveshapes are generally similar apart from the presence of high frequency ripples in the waveforms for the tortuous channel and slight differences in the peak values and zero-crossings. This can be explained by the fact that the tortuous channel, as shown in Figure 6.3, does not deviate much from the straight channel where the *x*-coordinates range from -45 m to 59 m and the *y*-

coordinates range from -75 m to 43 m. Hence for a tortuous channel whose path does not vary far from a straight channel, the straight vertical channel approximation can be adopted conveniently.

CHAPTER 7

CONCLUSION

As a key part of lightning research, lightning modelling has progressed over the years with the advent of new models, and modifications and improvements to current models. In contribution to this field of work, two lightning return stroke models which addressed the inadequacies of earlier endeavours were developed.

7.1 DISTRIBUTED CIRCUIT MODEL (CHIA-LIEW MODEL)

A new distributed circuit model was developed to simulate the lightning return stroke channel. On top of resistance and capacitance elements, the proposed model includes additional inductance elements in the lightning channel. The proposed model was shown to be capable of reproducing the median lightning current at ground, matching the peak current, charge lowered and front duration. In addition, it bears resemblance to the current waveshape of the DU model. Clearly, the proposed model is superior to the PL model in that it accounts for inductive elements along the lightning channel. Its edge over the DU model is evident in that it presents a more characteristic current

waveform based on median current parameters gathered from actual measurements rather than arbitrarily-set values.

The study conducted on the application of the proposed model on the SLE demonstrated the efficacy of the proposed model on lightning protection terminal systems which can easily be modelled by resistive and inductive elements. This application allows for the prediction of lightning current levels in the protection systems to assess their behaviour and performance when struck directly by lightning.

7.2 TORTUOUS LIGHTNING CHANNELS

A major fault in Lupò *et al.*'s formulation was identified and addressed. Upon improvisation of the current and charge description, the improved model has demonstrated to be capable of calculating the electromagnetic fields for tortuous lightning channels. The fields at various heights and distances are presented while earlier models usually present only either the electromagnetic fields at ground or at far distances adopting the Fraunhofer approximation.

The calculated field waveforms also demonstrated certain key characteristics observed from actual measurements, namely the sharp initial peak as well as the zero-crossing for fields at far distances. The fine structure seen in measured electromagnetic fields, which is absent in electromagnetic field waveforms calculated from models adopting a straight vertical lightning channel, was also present in the presented waveforms. This is a clear advantage of this model over others which adopt the straight vertical lightning channel approximation.

7.3 SCOPE FOR FUTURE WORK

A possible extension to the models is to incorporate a variable return stroke speed to study its effect on the resultant return stroke current and electromagnetic fields.

The distributed circuit model can be further applied to other novel lightning protection systems to investigate their performance.

For the electromagnetic model, a variable return stroke current can be employed to study its effect on the resultant field waveforms.

Potential applications of the electromagnetic field model include the reproduction of the lightning stroke path and also the calculation of the effects of the propagating electromagnetic fields on equipments and systems in the range of the lightning discharge. Assessment of vulnerability of equipment (e.g. aircraft avionics, telecommunication systems, computer systems, distributed control systems, etc.) and hence its protection, can then be performed.

BIBLIOGRAPHY

[1] M. A. Uman, *The Lightning Discharge*, New York: Academic, 1987.

[2] M. A. Uman and E. P. Krider, "A Review of Natural Lightning: Experimental Data and Modeling," *IEEE Trans. Electromagn. Compat.*, vol. 24, pp79–112, 1982.

[3] E. Pan and A. C. Liew, "Effect of Resistance on Lightning Return Stroke Current," *IEEE Trans. Power Delivery*, vol. 15, pp. 135–141, Jan. 2000.

[4] G. R. Xie, C. X. Chen, Y. P. Chen, X. S. Wen, and J. H. Yu, "Theory and Practice of Semiconductor Lightning Eliminator," in *Proc. Int. Conf. Energy Management Power Delivery*, 1998, pp. 532–537.

[5] C. X. Chen, G. R. Xie, and Z. F. Xie, "An Introduction to the Semiconductor Lightning Eliminator," in *Proc. Power Engineering Soc. Winter Meeting*, vol. 3, 2000, pp. 2101–2106.

[6] G. Lupò, C. Petrarca, V. Tucci and M, Vitelli, "EM Fields Generated by Lightning Channels with Arbitrary Location and Slope," *IEEE Trans. Electromagn. Compat.*, vol. 42, no. 1, pp. 39–53, 2000.

[7] V. A. Rakov and M. A. Uman, *Lightning: Physics and Effects*. Cambridge University Press, 2003.

[8] K. Berger, "Blitzstrom-Parameter von Aufwärtsblitzen," *Bull. Schweiz. Elektrotech. Ver.,* vol. 69, pp. 353–360, 1978.

[9] P. E. Viemeister, *The Lightning Book*. First MIT Press, 1972.

[10] P. R. Krehbiel, "The Electrical Structure of Thunderstorms," in *The Earth's Electrical Environment*, eds. E. P. Krider and R. G. Roble, Washington, DC: National Academy Press, 1986, pp. 90–113.

[11] W. H. Beasley, M. A. Uman and P. L. Rustan, "Electric Fields Preceding Cloud-to-Ground Lightning Flashes," *J. Geophys. Res.*, vol. 87, C7, pp. 4883–4902, 1982.

[12] B. F. J. Schonland, "The Lightning Discharge," in *Handbuch der Physik*, ed. S. Fulgge, Berlin: Springer-Verlag, 1956, pp. 576–628.

[13] E. M. Thomson, M. A. Uman and W. H. Beasley, "Speed and Current for Lightning Stepped Leaders near Ground as Determined from Electric Field Records," *J. Geophys. Res.*, vol. 90, pp. 8136–8142, 1985.

[14] K. Berger, R. B. Anderson and H. Kroninger, "Parameters of Lightning Flashes," *Electra*, vol. 41, pp. 23–37, 1975.

[15] D. M. Mach and W. D. Rust, "Photoelectric Return-Stroke Velocity and Peak Current Estimates in Natural and Triggered Lightning," *J. Geophys. Res.*, Vol.94, D11, pp. 13237–13247, 1989.

[16] E. M. Thomson, M. A. Galib, M. A. Uman, W. H. Beasley and M. J. Master, "Some Features of Stroke Occurrence in Florida Lightning Flashes," *J. Geophys. Res.*, vol. 89, pp. 4910–4916, 1984.

[17] M. Brook, N. Kitagawa and E. J. Workman, "Quantitative Study of Strokes and Continuing Currents in Lightning Discharges to Ground," *J. Geophys. Res.*, vol. 67, pp. 649–659, 1962.

[18] Y. T. Lin, M. A. Uman, J. A. Tiller, R. D. Brantley and W. H. Beasley, "Characterization of Lightning Return Stroke Electric and Magnetic Fields from Simultaneous Two-Station Measurements," *J. Geophys. Res.*, vol. 84, pp. 6307–6314, 1979

[19] C. A. Nucci, G. Diendorfer, M. A. Uman, F. Rachidi, M. Ianoz and C. Mazzetti, "Lightning Return Stroke Current Models with a Specified Channel-Base Current: A Review and Comparison", *J. Geophys. Res.*, vol. 95, D12, pp. 20395–20408, 1990.

[20] R. Thottappillil and M. A. Uman, "Comparison of Lightning Return-Stroke Models," *J. Geophys. Res.*, vol. 98, D12, pp. 22903–22914, 1993.

[21] A. H. Paxton, R. L. Gardner and L. Baker, "Lightning Return Stroke: A Numerical Calculation of the Optical Radiation," *Phys. Fluids*, vol. 29, pp. 2736–2741, 1986.

[22] A. S. Podgorski and J. A. Landt, "Three Dimensional Time Domain Modelling of Lightning," *IEEE Trans. Power Del.*, vol. 2, pp. 931–938, 1987.

[23] R. Moini, B. Kordi, G. Z. Rafi and V. A. Rakov, "A New Lightning Return Stroke Model Based on Antenna Theory," *J. Geophys. Res.*, vol. 105, D24, pp. 29693–29702, 2000.

[24] Y. Baba and M. Ishii, "Numerical Electromagnetic Field Analysis of Lightning Current in Tall Structures," *IEEE Trans. Power Del.*, vol. 16, no. 2, pp. 324–328, 2001.

[25] P. F. Little, "Transmission Line Representation of a Lightning Return Stroke", *J. Phys. D: Appl. Phys*., vol. 11, pp. 1893–1910, 1978.

[26] C. E. R. Bruce and R. H. Golde, "The Lightning Discharge," *J. Inst. Elect. Eng.*, vol. 88, pp. 487–520, 1941.

[27] M. A. Uman and D. K. McLain, "Magnetic Field of the Lightning Return Stroke," *J. Geophys. Res.*, vol. 74, pp. 6899–6910, 1969.

[28] M. J. Master, M. A. Uman, Y. T. Lin, and R. B. Standler, "Calculations of Lightning Return Stroke Electric and Magnetic Fields above Ground," *J. Geophys. Res.*, vol. 86, pp. 12127–12132, 1981.

[29] F. Heidler, "Traveling Current Source Model for LEMP Calculation," in *Proc. 6th Int. Zurich Symp. Electromagn. Compat., Zurich, Switzerland*, Mar. 1985, pp. 157–162.

[30] G. Diendorfer and M. A. Uman, "An Improved Return Stroke Model with Specified Channel-Base Current," *J. Geophys. Res.*, vol. 95, D11, pp. 13621–13644, 1990.

[31] M. A. Uman, D. K. McLain and E. P. Krider, "The Electromagnetic Radiation from a Finite Antenna," *Am. J. Phys.*, vol. 43, pp. 33 – 38, 1975.

[32] M. J. Master and M. A. Uman, "Transient Electric and Magnetic Fields Associated with Establishing a Finite Electrostatic Dipole," *Am. J. Phys.*, vol. 51, pp. 118–126, 1983.

[33] C. A. Nucci, C. Mazzetti, F. Rachidi and M. Ianoz, "On Lightning Return Stroke Models for LEMP Calculations," in *Proc. 19th Int. Conf. on Lightning Protection, Graz, Austria*, April 1988, 463–469.

[34] F. Rachidi and C. A. Nucci, "On the Master, Uman, Lin, Standler and the Modified Transmission Line Lightning Return Stroke Current Models," *J. Geophys. Res.*, vol. 95, D12, pp. 20389–20394, 1990.

[35] R. Thottappillil, D. K. McLain, M. A. Uman and G. Diendorfer, "Extension of the Diendorfer-Uman Lightning Return Stroke Model to the Case of a Variable

Upward Return Stroke Speed and a Variable Downward Discharge Current Speed", *J. Geophys. Res.*, vol. 96, D9, pp. 17143–17150, 1991.

[36] G. Lupò, C. Petrarca, V. Tucci and M, Vitelli, "EM Fields Associated with Lightning Channels: On the Effect of Tortuosity and Branching," *IEEE Trans. Electromagn. Compat.*, vol. 42, no. 4, pp. 394–404, 2000.

[37] P. C. Thum, A. C. Liew, and C. M. Wong, "Computer Simulation of the Initial Stages of the Lightning Protection Mechanism," *IEEE Trans. PAS*, vol. PAS-101, no. 11, pp. 4370–4377, 1982.

[38] P. C. Thum, A. C. Liew, and C. M. Wong, "Electrostatic Field Computation by an Integral Equation Method," *Elect. Power Syst. Res.*, pp. 259–275, 1982.

[39] F. A. M. Rizk, "Modeling of Lightning Incidence to Tall Structures," "Part I: Theory," "Part II: Application," *IEEE Trans. Power Delivery*, vol. 9, pp. 162–193, Jan. 1994.

[40] C. A. Jordan, "Lightning Computations for Transmission Lines with Overhead Ground Wires," *General Electric Rev.*, vol. 37, no. 3, Mar. 1934.

[41] A. C. Monteith, H. R. Vaughan, and A. A. Johnson, "Insulation Coordination," in *Electrical Transmission and Distribution Reference Book*. East Pittsburgh, PA: Westinghouse Electric Corp., 1964, pp. 610–642.

[42] J. A. Stratton, *Electromagnetic Theory*. New York: McGraw-Hill, 1941.

[43] R. D. Hill, "Analysis of Irregular Paths of Lightning Channels," *J. Geophys. Res.*, vol. 73, pp. 1897–1906, 1968.

[44] V. P. Idone and R. E. Orville, "Channel tortuosity variation in Florida triggered lightning," Geophys. Res. Lett., vol. 15, no. 7, pp. 645–648, 1988.

[45] V. A. Rakov, "Lightning Electric and Magnetic Fields," in *Proc. 13th Int. Symp. On Electromagnetic Compatibility, Zurich, Switzerland*, 1999, pp. 561–566.

APPENDIX A

DERIVATION OF ELECTROMAGNETIC FIELD EQUATIONS

Using the vector magnetic potential **A** and scalar electric potential φ expressions, the electric field strength **E** and magnetic field strength **H** are given by

$$\mathbf{E} = -\nabla\varphi - \frac{\partial \mathbf{A}}{\partial t} \tag{A.1}$$

$$\mathbf{H} = \frac{\nabla \times \mathbf{A}}{\mu} \tag{A.2}$$

The vector magnetic potential $d\mathbf{A}$ and scalar electric potential $d\varphi$ associated with an infinitesimal element of length dz', at $z = z'$, traversed by a current $i(z',t)$ and carrying a charge $\lambda(z',t)dz'$ are

$$d\mathbf{A} = \frac{\mu_0}{4\pi}\frac{i\left(z', t - \frac{R_r}{c}\right)}{R_r} dz' \mathbf{a_z} \tag{A.3}$$

$$d\varphi(r,\phi,z) = \frac{1}{4\pi\varepsilon_0}\frac{\lambda\left(z', t - \frac{R_r}{c}\right)}{R_r} dz' \tag{A.4}$$

where $\mathbf{a_z}$ is the unit vector along the z-axis, c is the speed of light and

$$R_r = \sqrt{(x'-x)^2 + (y'-y)^2 + (z'-z)^2} \tag{A.5}$$

The current profile assumed is a unit step function

$$i^{+}\left(z',t\right)=u\left(t-\frac{z'}{v}\right) \tag{A.6}$$

where v is the return stroke front speed and u is the Heaviside step function.

Applying the continuity equation

$$\nabla\cdot\mathbf{J}=-\frac{\partial\rho}{\partial t} \tag{A.7}$$

the corresponding charge distribution is

$$\begin{aligned}\lambda^{+}\left(z',t\right)&=\lambda^{+}\left(z',0\right)-\int_{0}^{t}\frac{\partial i^{+}\left(z',\tau\right)}{\partial z'}d\tau\\&=-\int_{0}^{t}\left[-\frac{1}{v}\delta\left(\tau-\frac{z'}{v}\right)\right]d\tau\\&=\frac{1}{v}u\left(t-\frac{z'}{v}\right)\end{aligned} \tag{A.8}$$

where δ is the Dirac delta function and the initial charge distribution $\lambda^{+}(z',0)$ is assumed to be zero.

Substituting equations (A.6) and (A.8) into equations (A.3) and(A.4),

$$d\mathbf{A}^{+}=\frac{\mu_0}{4\pi}I_0\times\frac{1}{R_r}u\left(t-\frac{z'}{v}-\frac{R_r}{c}\right)dz'\mathbf{a_z} \tag{A.9}$$

$$d\varphi^{+}\left(r,\phi,z\right)=-\frac{1}{4\pi\varepsilon_0}\times\frac{I_0}{R_r}\times\left[-\frac{1}{v}u\left(t-\frac{z'}{v}-\frac{R_r}{c}\right)\right] \tag{A.10}$$

To find $\mathbf{H}^{+}$, take the curl of $d\mathbf{A}$ and integrate along the segment. Since $x' = y' = 0$,

$$R_r=\sqrt{x^2+y^2+\left(z'-z\right)^2}=\sqrt{r^2+\left(z'-z\right)^2} \tag{A.11}$$

Let $\mathbf{F}^+ = \frac{1}{R_r} u\left(t - \frac{z'}{v} - \frac{R_r}{c}\right)$,

$$\begin{aligned}
\nabla \times \mathbf{F}^+ &= \mathbf{a}_r \left(\frac{\partial F_z^+}{r\partial\phi} - \frac{\partial F_\phi^+}{\partial z} \right) + \mathbf{a}_\phi \left(\frac{\partial F_r^+}{\partial z} - \frac{\partial F_z^+}{\partial r} \right) + \mathbf{a}_z \frac{1}{r} \left[\frac{\partial}{\partial r}\left(r F_\phi^+ \right) - \frac{\partial F_r^+}{\partial \phi} \right] \\
&= -\mathbf{a}_\phi \frac{\partial F_z^+}{\partial r} \\
&= -\mathbf{a}_\phi \frac{\partial F_z^+}{\partial R_r} \times \frac{\partial R_r}{\partial r} \\
&= -\mathbf{a}_\phi \left[-\frac{1}{R_r^{\,2}} u\left(t - \frac{z'}{v} - \frac{R_r}{c}\right) - \frac{1}{cR_r} \delta\left(t - \frac{z'}{v} - \frac{R_r}{c}\right) \right] \times \frac{r}{R_r} \\
&= \mathbf{a}_\phi \left[\frac{r}{R_r^{\,3}} u\left(t - \frac{z'}{v} - \frac{R_r}{c}\right) + \frac{r}{cR_r^{\,2}} \delta\left(t - \frac{z'}{v} - \frac{R_r}{c}\right) \right]
\end{aligned} \tag{A.12}$$

Hence

$$\begin{aligned}
\mathbf{H}^+ &= \frac{1}{\mu_0} \int_0^h \left(\nabla \times d\mathbf{A}^+ \right) \\
&= \frac{I_0}{4\pi} \int_0^h \left[\nabla \times \mathbf{F}^+(t) \right] dz'
\end{aligned} \tag{A.13}$$

Therefore

$$\begin{aligned}
H_r^+ &= 0 \\
H_z^+ &= 0 \\
H_\phi^+ &= \int_0^h g^+(t)\, dz'
\end{aligned} \tag{A.14}$$

where

$$g^+(t) = \frac{1}{4\pi} \left[\frac{r}{R_r^{\,3}} u\left(t - \frac{z'}{v} - \frac{R_r}{c}\right) + \frac{r}{cR_r^{\,2}} \delta\left(t - \frac{z'}{v} - \frac{R_r}{c}\right) \right] \tag{A.15}$$

Similarly, to find $\mathbf{E}^+$, substitute equations (A.9) and (A.10) into equation (A.1) and integrate along the segment.

$$\mathbf{A}^{+} = \int_0^h \frac{\mu_0}{4\pi} \times \frac{1}{R_r} u\left(t - \frac{z'}{v} - \frac{R_r}{c}\right) dz' \mathbf{a_z} \tag{A.16}$$

$$\Rightarrow \qquad \frac{\partial \mathbf{A}^{+}}{\partial t} = \frac{\mu_0}{4\pi} \int_0^h \frac{1}{R_r} \delta\left(t - \frac{z'}{v} - \frac{R_r}{c}\right) dz' \mathbf{a_z} \tag{A.17}$$

$$\nabla \varphi^{+} = \mathbf{a}_r \frac{\partial \varphi^{+}}{\partial r} + \mathbf{a}_\phi \frac{\partial \varphi^{+}}{r \partial \phi} + \mathbf{a}_z \frac{\partial \varphi^{+}}{\partial z} \tag{A.18}$$

For the *r*-component,

$$\begin{aligned}
&\int_0^h \left\{ \frac{\partial}{\partial r} \left[\frac{1}{4\pi v \varepsilon_0} \frac{1}{R_r} u\left(t - \frac{z'}{v} - \frac{R_r}{c}\right) \right] \right\} dz' \\
&\quad = \int_0^h \left\{ \frac{1}{4\pi v \varepsilon_0} \left[\frac{-1}{R_r^{\,2}} u\left(t - \frac{z'}{v} - \frac{R_r}{c}\right) + \frac{1}{R_r} \left(\frac{-1}{c}\right) \delta\left(t - \frac{z'}{v} - \frac{R_r}{c}\right) \right] \times \left(\frac{r}{R_r}\right) \right\} dz' \\
&\quad = \int_0^h \left\{ \frac{-1}{4\pi v \varepsilon_0} \left[\frac{r}{R_r^{\,3}} u\left(t - \frac{z'}{v} - \frac{R_r}{c}\right) + \frac{r}{c R_r^{\,2}} \delta\left(t - \frac{z'}{v} - \frac{R_r}{c}\right) \right] \right\} dz' \\
&\quad = -\int_0^h m^{+}(t)\, dz'
\end{aligned} \tag{A.19}$$

where

$$m^{+}(t) = \frac{1}{4\pi v \varepsilon_0} \left[\frac{r}{R_r^{\,3}} u\left(t - \frac{z'}{v} - \frac{R_r}{c}\right) + \frac{1}{c R_r^{\,2}} \delta\left(t - \frac{z'}{v} - \frac{R_r}{c}\right) \right] \tag{A.20}$$

For the *z*-component,

$$\begin{aligned}
&\int_0^h \left\{ \frac{\partial}{\partial z}\left[\frac{1}{4\pi v\varepsilon_0}\frac{1}{R_r} u\left(t-\frac{z'}{v}-\frac{R_r}{c}\right)\right]\right\} dz' \\
&\quad = \int_0^h \left\{ \frac{1}{4\pi v\varepsilon_0}\left[\frac{-1}{R_r^{\,2}} u\left(t-\frac{z'}{v}-\frac{R_r}{c}\right) + \frac{1}{R_r}\left(\frac{-1}{c}\right)\delta\left(t-\frac{z'}{v}-\frac{R_r}{c}\right)\right]\times\left(\frac{z-z'}{R_r}\right)\right\} dz' \\
&\quad = \int_0^h \left\{ \frac{-1}{4\pi v\varepsilon_0}\left[\frac{z-z'}{R_r^{\,3}} u\left(t-\frac{z'}{v}-\frac{R_r}{c}\right) + \frac{z-z'}{cR_r^{\,2}}\delta\left(t-\frac{z'}{v}-\frac{R_r}{c}\right)\right]\right\} dz'
\end{aligned} \tag{A.21}$$

Grouping with the $\dfrac{\partial \mathbf{A}^+}{\partial t}$ term, let

$$n^+(t) = \frac{1}{4\pi v\varepsilon_0}\left[\frac{z-z'}{R_r^{\,3}} u\left(t-\frac{z'}{v}-\frac{R_r}{c}\right) + \frac{z-z'}{cR_r^{\,2}}\delta\left(t-\frac{z'}{v}-\frac{R_r}{c}\right)\right] - \frac{\mu_0}{4\pi}\frac{1}{R_r}\delta\left(t-\frac{z'}{v}-\frac{R_r}{c}\right) \tag{A.22}$$

Hence

$$\begin{aligned}
E_r^+ &= \int_0^h m^+(t)\, dz' \\
E_z^+ &= \int_0^h n^+(t)\, dz' \\
E_\phi^+ &= 0
\end{aligned} \tag{A.23}$$

where $m^+(t)$ and $n^+(t)$ are defined in equations (A.20) and(A.22).

As with most lightning models, a perfectly conducting ground is assumed and thus, the method of images can be applied. A similar analysis is followed to obtain the contributions of the image below ground. The quantities for the image is superscripted with the negative sign '–' for differentiation with the segment above ground which is superscripted with the positive sign '+'.

For the image, $-h \le z' \le 0$,

$$i^{-}\left(z',t\right) = u\left(t + \frac{z'}{v}\right) \tag{A.24}$$

and

$$\begin{aligned}\lambda^{-}\left(z',t\right) &= \lambda^{-}\left(z',0\right) - \int_0^t \frac{\partial i^{-}\left(z',\tau\right)}{\partial z'} d\tau \\ &= -\int_0^t \left[\frac{1}{v}\delta\left(\tau + \frac{z'}{v}\right)\right] d\tau \\ &= -\left[\frac{1}{v}u\left(t + \frac{z'}{v}\right)\right] \\ &= -\lambda^{+}\left(-z',t\right)\end{aligned} \tag{A.25}$$

Similarly, the initial charge distribution $\lambda^{-}(z',0)$ was set to zero

Substituting equations (A.24) and (A.25) into equations (A.3) and (A.4),

$$d\mathbf{A}^{-} = \frac{\mu_0}{4\pi} \times \frac{1}{R_r} u\left(t + \frac{z'}{v} - \frac{R_r}{c}\right) dz' \mathbf{a_z} \tag{A.26}$$

$$d\varphi^{-}\left(r,\phi,z\right) = \frac{1}{4\pi\varepsilon_0} \times \frac{1}{R_r} \times \left[-\frac{1}{v} u\left(t + \frac{z'}{v} - \frac{R_r}{c}\right)\right] \tag{A.27}$$

$\mathbf{H}^{-}$ is found as previously with the integral limits changed to from $-h$ to 0.

Let $\mathbf{F}^- = \frac{1}{R_r} u\left(t + \frac{z'}{v} - \frac{R_r}{c}\right)$,

$$\begin{aligned}
\nabla \times \mathbf{F}^- &= \mathbf{a}_r \left(\frac{\partial F_z^-}{r\partial\phi} - \frac{\partial F_\phi^-}{\partial z} \right) + \mathbf{a}_\phi \left(\frac{\partial F_r^-}{\partial z} - \frac{\partial F_z^-}{\partial r} \right) + \mathbf{a}_z \frac{1}{r} \left[\frac{\partial}{\partial r}\left(rF_\phi^- \right) - \frac{\partial F_r^-}{\partial \phi} \right] \\
&= -\mathbf{a}_\phi \frac{\partial F_z^-}{\partial r} \\
&= -\mathbf{a}_\phi \frac{\partial F_z^-}{\partial R_r} \times \frac{\partial R_r}{\partial r} \\
&= -\mathbf{a}_\phi \left[-\frac{1}{R_r^{\,2}} u\left(t + \frac{z'}{v} - \frac{R_r}{c} \right) - \frac{1}{cR_r} \delta\left(t + \frac{z'}{v} - \frac{R_r}{c} \right) \right] \times \frac{r}{R_r} \\
&= \mathbf{a}_\phi \left[\frac{r}{R_r^{\,3}} u\left(t + \frac{z'}{v} - \frac{R_r}{c} \right) + \frac{r}{cR_r^{\,2}} \delta\left(t + \frac{z'}{v} - \frac{R_r}{c} \right) \right]
\end{aligned} \tag{A.28}$$

Hence,

$$\begin{aligned}
\mathbf{H}^- &= \frac{1}{\mu_0} \int_{-h}^{0} \left(\nabla \times d\mathbf{A}^- \right) \\
&= \frac{1}{4\pi} \int_{-h}^{0} \left[\nabla \times \mathbf{F}^-(t) \right] dz'
\end{aligned} \tag{A.29}$$

Therefore

$$\begin{aligned}
H_r^- &= 0 \\
H_z^- &= 0 \\
H_\phi^- &= \int_{-h}^{0} g^-(t)\, dz'
\end{aligned} \tag{A.30}$$

where

$$g^-(t) = \frac{1}{4\pi} \left[\frac{r}{R_r^{\,3}} u\left(t + \frac{z'}{v} - \frac{R_r}{c} \right) + \frac{r}{cR_r^{\,2}} \delta\left(t + \frac{z'}{v} - \frac{R_r}{c} \right) \right] \tag{A.31}$$

For $\mathbf{E}^-$, substitute equations (A.26) and (A.27) into equation (6.1) and integrate along the channel from from $-h$ to 0.

$$\mathbf{A}^{-} = \int_{-h}^{0} \frac{\mu_0}{4\pi} I_0 \times \frac{1}{R_r} u\left(t + \frac{z'}{v} - \frac{R_r}{c}\right) dz' \mathbf{a_z} \tag{A.32}$$

$$\Rightarrow \qquad \frac{\partial \mathbf{A}^{-}}{\partial t} = \frac{\mu_0 I_0}{4\pi} \int_{-h}^{0} \frac{1}{R_r} \delta\left(t + \frac{z'}{v} - \frac{R_r}{c}\right) dz' \mathbf{a_z} \tag{A.33}$$

$$\nabla \varphi^{-} = \mathbf{a}_r \frac{\partial \varphi^{-}}{\partial r} + \mathbf{a}_\phi \frac{\partial \varphi^{-}}{r \partial \phi} + \mathbf{a}_z \frac{\partial \varphi^{-}}{\partial z} \tag{A.34}$$

For the *r*-component,

$$\begin{aligned}
&\int_{-h}^{0} \left\{ \frac{\partial}{\partial r} \left[\frac{1}{4\pi v \varepsilon_0} \frac{1}{R_r} u\left(t + \frac{z'}{v} - \frac{R_r}{c}\right) \right] \times \left[u\left(z' + h\right) - u\left(z'\right) \right] \right\} dz' \\
&\quad = \int_{-h}^{0} \left\{ \frac{1}{4\pi v \varepsilon_0} \left[\frac{-1}{{R_r}^2} u\left(t + \frac{z'}{v} - \frac{R_r}{c}\right) + \frac{1}{R_r} \left(\frac{-1}{c}\right) \delta\left(t + \frac{z'}{v} - \frac{R_r}{c}\right) \right] \right. \\
&\qquad\qquad \left. \times \left(\frac{r}{R_r}\right) \times \left[u\left(z' + h\right) - u\left(z'\right) \right] \right\} dz' \\
&\quad = \int_{-h}^{0} \left\{ \frac{-1}{4\pi v \varepsilon_0} \left[\frac{r}{{R_r}^3} u\left(t + \frac{z'}{v} - \frac{R_r}{c}\right) + \frac{r}{c{R_r}^2} \delta\left(t + \frac{z'}{v} - \frac{R_r}{c}\right) \right] \right\} dz' \\
&\quad = -\int_{-h}^{0} m^{-}\left(t\right) dz'
\end{aligned} \tag{A.35}$$

where

$$m^{-}\left(t\right) = \frac{1}{4\pi v \varepsilon_0} \left[\frac{r}{{R_r}^3} u\left(t + \frac{z'}{v} - \frac{R_r}{c}\right) + \frac{1}{c{R_r}^2} \delta\left(t + \frac{z'}{v} - \frac{R_r}{c}\right) \right] \tag{A.36}$$

For the *z*-component,

$$\begin{aligned}
&\int_{-h}^{0}\left\{\frac{\partial}{\partial z}\left[\frac{1}{4\pi v\varepsilon_0}\frac{1}{R_r}u\left(t+\frac{z'}{v}-\frac{R_r}{c}\right)\right]\times\left[u\left(z'+h\right)-u\left(z'\right)\right]\right\}dz' \\
&\quad=\int_{-h}^{0}\left\{\frac{1}{4\pi v\varepsilon_0}\left[\frac{-1}{R_r^{\,2}}u\left(t+\frac{z'}{v}-\frac{R_r}{c}\right)+\frac{1}{R_r}\left(\frac{-1}{c}\right)\delta\left(t+\frac{z'}{v}-\frac{R_r}{c}\right)\right]\right. \\
&\qquad\left.\times\left(\frac{z-z'}{R_r}\right)\times\left[u\left(z'+h\right)-u\left(z'\right)\right]\right\}dz' \\
&\quad=\int_{-h}^{0}\left\{\frac{-1}{4\pi v\varepsilon_0}\left[\frac{z-z'}{R_r^{\,3}}u\left(t+\frac{z'}{v}-\frac{R_r}{c}\right)+\frac{z-z'}{cR_r^{\,2}}\delta\left(t+\frac{z'}{v}-\frac{R_r}{c}\right)\right]\right\}dz'
\end{aligned} \tag{A.37}$$

Grouping with the $\dfrac{\partial\mathbf{A}^{-}}{\partial t}$ term, let

$$n^{-}\left(t\right)=\frac{1}{4\pi v\varepsilon_0}\left[\frac{z-z'}{R_r^{\,3}}u\left(t+\frac{z'}{v}-\frac{R_r}{c}\right)+\frac{z-z'}{cR_r^{\,2}}\delta\left(t+\frac{z'}{v}-\frac{R_r}{c}\right)\right]+\frac{\mu_0}{4\pi}\frac{1}{R_r}\delta\left(t+\frac{z'}{v}-\frac{R_r}{c}\right) \tag{A.38}$$

Hence

$$\begin{aligned}
E_r^{-}&=-\int_{-h}^{0}m^{-}\left(t\right)dz' \\
E_z^{-}&=-\int_{-h}^{0}n^{-}\left(t\right)dz' \\
E_\phi^{-}&=0
\end{aligned} \tag{A.39}$$

where $m^{-}\left(t\right)$ and $n^{-}\left(t\right)$ are defined in equations (A.36) and(A.38).

For the integrals $\int g^{\pm}\left(t\right)dz'$, $\int m^{\pm}\left(t\right)dz'$ and $\int n^{\pm}\left(t\right)dz'$, the integrand contains either the Heaviside step function or the Dirac delta function with the argument

$$\psi^{\pm}\left(t\right)=t\,\mathrm{m}\frac{z'}{v}-\frac{R_r}{c} \tag{A.40}$$

The zeros of this function can by found as below:

$$t \mp \frac{\zeta_0^{\pm}}{v} - \frac{R_r}{c} = 0$$

$$t \mp \frac{\zeta_0^{\pm}}{v} - \frac{\sqrt{r^2 + \left(\zeta_0^{\pm} - z\right)^2}}{c} = 0$$

$$v\sqrt{r^2 + \left(\zeta_0^{\pm} - z\right)^2} = cvt \mp c\zeta_0^{\pm}$$

$$v^2\left[r^2 + \left(\zeta_0^{\pm} - z\right)^2\right] = c^2v^2t^2 \mp 2c^2vt\zeta_0^{\pm} + c^2\left(\zeta_0^{\pm}\right)^2$$

$$v^2r^2 + v^2\left(\zeta_0^{\pm}\right)^2 - 2v^2z\zeta_0^{\pm} + v^2z^2 = c^2v^2t^2 \mp 2c^2vt\zeta_0^{\pm} + c^2\left(\zeta_0^{\pm}\right)^2$$

$$\left(c^2 - v^2\right)\left(\zeta_0^{\pm}\right)^2 + \left(2v^2z \mp 2c^2vt\right)\zeta_0^{\pm} + c^2v^2t^2 - v^2r^2 - v^2z^2 = 0$$

$$\zeta_0^{\pm}(t) = \frac{\pm\frac{t}{v} - \frac{z}{c^2} \mp \sqrt{\left(\frac{t}{v} \mp \frac{z}{c^2}\right)^2 - \left(\frac{1}{v^2} - \frac{1}{c^2}\right)\left(t^2 - \frac{r^2}{c^2} - \frac{z^2}{c^2}\right)}}{\frac{1}{v^2} - \frac{1}{c^2}} \tag{A.41}$$

Note that the other root of the quadratic equation is neglected as it was introduced when the square of both sides was taken. A simple back-substitution can verify the choice of roots.

For $\mathbf{E}^+$ and $\mathbf{H}^+$, the Dirac delta term is equal to zero except when $z' = \zeta_0^+(t)$ and the Heaviside step term is equal to zero for $z' > \zeta_0^+(t)$.Therefore, when $\zeta_0^+(t) < 0$, both Heaviside step and Dirac delta functions are zero and when $\zeta_0^+(t) > h$, the Dirac delta function is zero while the Heaviside step function has a value of 1 for $0 \le z' \le h$. For $0 \le \zeta_0^+(t) \le h$, the upper limit for the integral can be changed to $\zeta_0^+(t)$.

Similarly for $\mathbf{E}^-$ and $\mathbf{H}^-$, the Dirac delta term is equal to zero except when $z' = \zeta_0^-(t)$ and the Heaviside step term is equal to zero for $z' < \zeta_0^-(t)$.Therefore, when $\zeta_0^-(t) > 0$,

the integrals for both Heaviside step and Dirac delta functions are zero and when $\zeta_0^-(t) < -h$, the integral for the Dirac delta term is zero while the integral for the Heaviside step function has a value of 1 for $-h \le z' \le 0$. For $-h \le \zeta_0^-(t) \le 0$, the lower limit for the integral can be changed to $\zeta_0^-(t)$.

To further evaluate the integrals, let $z' - z = r\tan\theta$

$$dz' = r\sec^2\theta d\theta \tag{A.42}$$

$$\theta(z_i') = \tan^{-1}\left(\frac{z_i' - z}{r}\right) \tag{A.43}$$

$$\begin{aligned}
\int_{z_1'}^{z_2'} \frac{r}{R_r^{\,3}} dz' &= \int_{z_1'}^{z_2'} \frac{r}{\left(\sqrt{r^2 + (z'-z)^2}\right)^3} dz' \\
&= \int_{\theta(z_1')}^{\theta(z_2')} \frac{r}{\left(\sqrt{r^2 + r^2\tan^2\theta}\right)^3} r\sec^2\theta d\theta \\
&= \int_{\theta(z_1')}^{\theta(z_2')} \frac{1}{r}\frac{\sec^2\theta}{\sec^3\theta} d\theta \\
&= \int_{\theta(z_1')}^{\theta(z_2')} \frac{1}{r}\cos\theta d\theta \\
&= \frac{1}{r}\left\{\sin\left[\tan^{-1}\left(\frac{z_2' - z}{r}\right)\right] - \sin\left[\tan^{-1}\left(\frac{z_1' - z}{r}\right)\right]\right\}
\end{aligned} \tag{A.44}$$

$$\begin{aligned}\int_{z_1'}^{z_2'} \frac{z-z'}{R_r^{\,3}} dz' &= \int_{z_1'}^{z_2'} \frac{z-z'}{\left(\sqrt{r^2+\left(z'-z\right)^2}\right)^3} dz' \\ &= \int_{\theta(z_1')}^{\theta(z_2')} \frac{-r\tan\theta}{\left(\sqrt{r^2+r^2\tan^2\theta}\right)^3} r\sec^2\theta d\theta \\ &= \int_{\theta(z_1')}^{\theta(z_2')} \frac{-1}{r}\frac{\tan\theta\sec^2\theta}{\sec^3\theta} d\theta \\ &= \int_{\theta(z_1')}^{\theta(z_2')} \frac{-1}{r}\sin\theta d\theta \\ &= \frac{1}{r}\left\{\cos\left[\tan^{-1}\left(\frac{z_2'-z}{r}\right)\right]-\cos\left[\tan^{-1}\left(\frac{z_1'-z}{r}\right)\right]\right\}\end{aligned} \tag{A.45}$$

Since $\delta\left[p(z)\right]=\sum_i \frac{\delta(z-z_i)}{\left|p'(z_i)\right|}$ where z_i are roots of p, for $z_1' \le \zeta_0^{\pm}(t) \le z_2'$,

$$\int_{z_1'}^{z_2'} \frac{r}{cR_r^{\,2}}\delta\left(t-\frac{z'}{v}-\frac{R_r}{c}\right)dz' = \frac{r}{c\left(R_{r,0}^{\pm}\right)^2\left|-\frac{1}{v}-\frac{\zeta_0^{\pm}(t)-z}{cR_{r,0}^{\pm}}\right|} \tag{A.46}$$

$$\int_{z_1'}^{z_2'} \frac{z-z'}{cR_r^{\,2}}\delta\left(t-\frac{z'}{v}-\frac{R_r}{c}\right)dz' = \frac{z-\zeta_0^{\pm}(t)}{c\left(R_{r,0}^{\mathrm{m}}\right)^2\left|-\frac{1}{v}-\frac{\zeta_0^{\pm}(t)-z}{cR_{r,0}^{\pm}}\right|} \tag{A.47}$$

$$\int_{z_1'}^{z_2'} \frac{1}{R_r}\delta\left(t-\frac{z'}{v}-\frac{R_r}{c}\right)dz' = \frac{1}{R_{r,0}^{\pm}\left|-\frac{1}{v}-\frac{\zeta_0^{\pm}(t)-z}{cR_{r,0}^{\pm}}\right|} \tag{A.48}$$

where

$$R_{r,0}^{\pm} = \sqrt{r^2+\left[\zeta_0^{\pm}(t)-z\right]^2} \tag{A.49}$$

Therefore the expressions for the integrals of $g^{\pm}(t)$, $m^{\pm}(t)$ and $n^{\pm}(t)$ can be written as shown in equations (A.50) to (A.55).

$$\int_0^h g^+(t)\,dz' = \begin{cases} 0, & \zeta_0^+(t) < 0 \\ \dfrac{1}{4\pi}\left[\dfrac{\sin\left[\theta\left(\zeta_0^+(t)\right)\right]-\sin\left[\theta(0)\right]}{r}+\dfrac{r}{c\left(R_{r,0}^+\right)^2\left|-\frac{1}{v}-\frac{\zeta_0^+(t)-z}{cR_{r,0}^+}\right|}\right], & 0 \le \zeta_0^+(t) \le h \\ \dfrac{1}{4\pi}\left[\dfrac{\sin\left[\theta(h)\right]-\sin\left[\theta(0)\right]}{r}\right], & \zeta_0^+(t) > h \end{cases} \tag{A.50}$$

$$\int_0^h m^+(t)\,dz' = \begin{cases} 0, & \zeta_0^+(t) < 0 \\ \dfrac{1}{4\pi v\varepsilon_0}\left[\dfrac{\sin\left[\theta\left(\zeta_0^+(t)\right)\right]-\sin\left[\theta(0)\right]}{r}+\dfrac{r}{c\left(R_{r,0}^+\right)^2\left|-\frac{1}{v}-\frac{\zeta_0^+(t)-z}{cR_{r,0}^+}\right|}\right], & 0 \le \zeta_0^+(t) \le h \\ \dfrac{1}{4\pi v\varepsilon_0}\left[\dfrac{\sin\left[\theta(h)\right]-\sin\left[\theta(0)\right]}{r}\right], & \zeta_0^+(t) > h \end{cases} \tag{A.51}$$

$$\int_0^h n^+(t)\,dz' = \begin{cases} 0, & \zeta_0^+(t) < 0 \\ \dfrac{1}{4\pi v\varepsilon_0}\left[\dfrac{\cos\left[\theta\left(\zeta_0^+(t)\right)\right]-\cos\left[\theta(0)\right]}{r}+\dfrac{z-\zeta_0^{\pm}(t)}{c\left(R_{r,0}^+\right)^2\left|-\frac{1}{v}-\frac{\zeta_0^+(t)-z}{cR_{r,0}^+}\right|}\right] & 0 \le \zeta_0^+(t) \le h \\ \qquad -\dfrac{\mu}{4\pi}\dfrac{1}{R_{r,0}^+\left|-\frac{1}{v}-\frac{\zeta_0^+(t)-z}{cR_{r,0}^+}\right|}, & \\ \dfrac{1}{4\pi v\varepsilon_0}\left[\dfrac{\cos\left[\theta(h)\right]-\cos\left[\theta(0)\right]}{r}\right], & \zeta_0^+(t) > h \end{cases} \tag{A.52}$$

Note that the limits $\zeta_0^+(t)<0$, $0\le\zeta_0^+(t)\le h$ and $\zeta_0^+(t)>h$ correspond respectively to $t<\dfrac{\sqrt{r^2+z^2}}{c}$, $\dfrac{\sqrt{r^2+z^2}}{c}\le t\le\dfrac{h}{v}+\dfrac{\sqrt{r^2+(z-h)^2}}{c}$ and $t>\dfrac{h}{v}+\dfrac{\sqrt{r^2+(z-h)^2}}{c}$.

$$\int_{-h}^{0} f^-(t)\,dz' = \begin{cases} \dfrac{1}{4\pi}\left[\dfrac{\sin\left[\theta(0)\right]-\sin\left[\theta(-h)\right]}{r}\right], & \zeta_0^-(t)<-h \\ \dfrac{1}{4\pi}\left[\dfrac{\sin\left[\theta(0)\right]-\sin\left[\theta\left(\zeta_0^-(t)\right)\right]}{r}+\dfrac{r}{c\left(R_{r,0}^-\right)^2\left|\frac{1}{v}-\frac{\zeta_0^-(t)-z}{cR_{r,0}^-}\right|}\right], & -h\le\zeta_0^-(t)\le 0 \\ 0, & \zeta_0^-(t)>0 \end{cases} \tag{A.53}$$

$$\int_{-h}^{0} g^-(t)\,dz' = \begin{cases} \dfrac{1}{4\pi v\varepsilon_0}\left[\dfrac{\sin\left[\theta(0)\right]-\sin\left[\theta(-h)\right]}{r}\right], & \zeta_0^-(t)<-h \\ \dfrac{1}{4\pi v\varepsilon_0}\left[\dfrac{\sin\left[\theta(0)\right]-\sin\left[\theta\left(\zeta_0^-(t)\right)\right]}{r}+\dfrac{r}{c\left(R_{r,0}^-\right)^2\left|\frac{1}{v}-\frac{\zeta_0^-(t)-z}{cR_{r,0}^-}\right|}\right], & -h\le\zeta_0^-(t)\le 0 \\ 0, & \zeta_0^-(t)>0 \end{cases} \tag{A.54}$$

$$\int_{-h}^{0} p^{-}(t)\,dz' = \begin{cases} \dfrac{I_0}{4\pi v\varepsilon_0}\left[\dfrac{\cos\left[\theta(0)\right]-\cos\left[\theta(-h)\right]}{r}\right], & \zeta_0^{-}(t) < -h \\ \dfrac{I_0}{4\pi v\varepsilon_0}\left[\dfrac{\cos\left[\theta(0)\right]-\cos\left[\theta\left(\zeta_0^{-}(t)\right)\right]}{r}+\dfrac{z-\zeta_0^{-}(t)}{c\left(R_{r,0}^{-}\right)^2\left|\frac{1}{v}-\frac{\zeta_0^{-}(t)-z}{cR_{r,0}^{-}}\right|}\right] & -h \le \zeta_0^{-}(t) \le 0 \\ \qquad\qquad +\dfrac{\mu I_0}{4\pi}\dfrac{1}{R_{r,0}^{-}\left|\frac{1}{v}-\frac{\zeta_0^{-}(t)-z}{cR_{r,0}^{-}}\right|}, & \\ 0, & \zeta_0^{-}(t) > 0 \end{cases} \tag{A.55}$$

Similarly, the limits $\zeta_0^{-}(t) < -h$, $-h \le \zeta_0^{-}(t) \le 0$ and $\zeta_0^{-}(t) > 0$ correspond respectively to $t > \frac{h}{v} + \frac{\sqrt{r^2+(z+h)^2}}{c}$, $\frac{\sqrt{r^2+z^2}}{c} \le t \le \frac{h}{v} + \frac{\sqrt{r^2+(z+h)^2}}{c}$ and $t < \frac{\sqrt{r^2+z^2}}{c}$.